The Pennsylvania State University

The Graduate School

COLD SINTERING OF CERAMIC MATRIX COMPOSITES FOR VARISTORS AND MICROWAVE DIELECTRIC SUBSTRATES

A Dissertation in

Materials Science and Engineering

by

Javier Mena Garcia

Submitted in Partial Fulfillment
of the Requirements
for the Degree of

Doctor of Philosophy

August 2024

The dissertation of Javier Mena Garcia was reviewed and approved by the following:

Clive A. Randall
Evan Pugh University Professor
Distinguished Professor of Materials Science and Engineering
Dissertation Advisor
Chair of Committee

Susan E. Trolier-McKinstry
Evan Pugh University Professor
Steward S. Flaschen Professor of Ceramic Science and Engineering
Professor of Electrical Engineering

Andrea P. Argüelles
Assistant Professor of Engineering Science and Mechanics

Qiming Zhang
Distinguished Professor of Electrical Engineering

John C. Mauro
Dorothy Pate Enright Professor of Materials Science and Engineering
Chair of Intercollege Graduate Degree Program in Materials Science
and Engineering

ABSTRACT

This dissertation presents a comprehensive investigation into the synthesis, characterization, and application of ceramic-polymer composites and ceramic matrix composites (CMC) through the cold sintering process. With a primary focus on understanding the relationship between the designed composites' microstructures and their physical properties, this research integrates the results and learnings from four integral studies to elucidate the multifaceted aspects of materials science and engineering.

The initial study explores into the design of ceramic-polymer composites, integrating the ferroelectric co-polymer polyvinylidene fluoride-trifluoroethylene (PVDF-TrFE) at the grain boundaries of a semiconducting zinc oxide (ZnO) matrix. Through a synergistic approach encompassing electrical conductivity modeling, dielectric characterization, and transmission electron microscopy (TEM) investigation, the study unveils the pivotal role of PVDF-TrFE in modulating the electrical properties of the composite, with an average thickness of 3 nm of PVDF-TrFE at the grain boundaries of ZnO measured by TEM and confirmed by calculations based on the Maxwell-Wagner-Sillars (MWS) effect. The addition of only 2 vol.% of PVDF-TrFE was sufficient to improve the non-linear conductivity and enable the Fowler-Nordheim tunneling mechanism at high applied electric fields, with a low barrier height of $q\varphi_B = 0.1$ eV. The critical electric field per grain boundary to transition from Schottky thermionic emission at low electric fields to Fowler-Nordheim tunneling was identified at 2.6 $\mathrm{V{\bullet}nm^{-1}}$.

Subsequent investigations underscore pressing necessity for advanced dielectric substrates tailored to the demands of modern 5G and 6G communication technologies. Employing sodium molybdate ($Na_2Mo_2O_7$, NMO) as the ceramic matrix and hexagonal boron nitride (hBN) as the filler, dense CMCs are fabricated to augment the thermal conductivity from 2 to 12 $\mathrm{W{\bullet}m^{-1}K^{-1}}$, and to improve the dielectric properties by decreasing the relative permittivity from 13 to 8, at 10^6 and

9-13 GHz frequencies, with the addition of 50 vol.% of hBN. The dielectric loss of the composites was lower than 8×10^{-4} at microwave frequencies. The following exploration extends this paradigm by incorporating diamond as a filler, aiming to further enhance thermal conductivity while maintaining minimal dielectric loss, thus elucidating the potential of engineered CMCs as versatile microwave substrate materials.

Integral to the thesis is an in-depth analysis of the densification process of the NMO ceramic matrix phase, cold sintered in conjunction with filler materials of hBN and micro diamond (md). Through examination of kinetics, mechanisms, and microstructural changes, including pressure solution creep and steady-state creep processes induced by applied stress and variation of temperatures, this study describes the densification behavior and underscores the transformative impact of filler materials on mechanical and thermal properties. A dilatometry study allowed to identify activation energies between 48 and 97 kJ/mol for the NMO, NMO-hBN and NMO-md samples, using the Woolfrey-Bannister method. Norton's equation was used to estimate activation energy of 36 kJ/mol for NMO and the NMO-md composites, in the isothermal region of the steady-state creep. Determination of n stress exponent was used to identify the creep mechanisms of diffusional transport (n~1) for NMO and sliding interfaces (n~2) for NMO-md composites.

By synthesizing findings from these interconnected studies, this thesis contributes to a holistic understanding of CSP-derived composites, offering valuable insights into their potential applications across a spectrum of communication technologies and microwave substrate materials.

TABLE OF CONTENTS

LIST OF FIGURES

LIST OF TABLES

ACKNOWLEDGEMENTS

First and foremost, I would like to thank my advisor, Professor Clive Randall, for being the best advisor, teacher, and mentor I could have ever asked for. He is always ready to offer his support in both academic and personal matters. His dedication, openness and hard work have strongly inspired me to learn how to be a good researcher and keep me motivated to achieve my professional goals. Professor Randall, I wholeheartedly appreciate your mentorship and your trust in me, to continuously accomplish more than what I can initially visualize. I truly cannot put all my gratitude into words. I will always feel fortunate to have you as a role model for my future, and I am very proud of being a member of your group. Thank you for the opportunities to explore the world and understand it a little better.

Secondly, I would like to express my sincere appreciation to the rest of the members of my committee, Professor Susan Trolier-McKinstry, Professor Andrea Argüelles and Professor Qiming Zhang, for their thoughtful feedback, keen suggestions and stimulating questions, helping me to improve the quality of my thesis.

Many thanks to the Materials Research Institute technical team: Steve Perini, Jeff Long, Michael Norrell, Amira Meddeb, Julie Anderson, Wesley Auker, Nichole Wonderling, Gino Tambourine, Maria DiCola and Tawanda Zimudzi, for helping me overcome technical difficulties and for the training sessions. To Professor Wenjie Li, Professor Bed Poudel, Professor Paolo Colombo and Professor Michael Lanagan, for their guidance and collaboration in my research efforts. A special thanks also goes to Melissa Bailey and Joanne Aller, for helping me with all administrative processes related to the conferences, meetings, traveling and events that enriched my academic experience.

I would also like to acknowledge the sources of federal funding that enabled my work, specifically the National Science Foundation and the Center for Dielectrics and Piezoelectrics

under Grant Nos. IIP-1841466 and IIP-1841453. I also acknowledge the COMEXUS Fulbright-Garcia Robles scholarship for opening the door to a pathway leading to my PhD program at Penn State. Finally, the findings and conclusions in this dissertation do not necessarily reflect the view of the funding agencies.

I would like to thank my friends in Professor Randall's group, for being there for each other, for helping me to solve some troubleshooting problems, providing a supportive environment to share intellectual ideas and a daily dose of humor: Arnaud Ndayishimiye (and Alexandra), Sinan Dursun, Zhongming Fan, Koki Nakagawa, Toshiki Okazaki, Takashi Nunokawa, Hiroshi Nishiyama, Kosuke Tsuji, Sun-Hwi Bang, Zane Grady, Pedram Yousefian (and Samira), Jake DeChiara, Julian Fanghanel (and Lucia), Sevag Momjian, Michael Mervosh, Adam Vetser, Topher Wheatley (and Heidi), and thanks to my friends outside of my research group: Furkan Turker (and Cansu), Benazir Fazlioglu Yalcin (and Omer), Stephanie Castro (and Jay), Travis Peters (and Maepearl), Jake Tipsawat, Ryan Hawks, Betul Akkopru Akgun, Haley Jones, Mohamed El Sayed Eltantawy, Rocio Rodriguez, Anton Tuluk, Lorenzo Lattanzi, Linsea Foster, Abdullah Jabr, Erkan Gurdal (and Elise), James Roscow, Yosuke Endo, Eriko Maeda, Tatiana Kuznetsova, Ricardo Amaral and Marco Damasceno, Gaby Rivera and Michelle Soo, Jeremy Engels and Anna Engels. I consider myself incredibly lucky to be surrounded by smart scientists. Thank you very much for the long working hours, the helpful discussions, and for your support. I believe this work would not have been possible without your help.

I would also like to thank my parents, Javier and María Teresa, for their endless support. Without your encouragement, understanding and believing in me, I couldn't be the person I am today. Thank you very much for your love, support, and sacrifice throughout my PhD years and all my life.

Finally, I would like to thank my wife, Cristy, for her infinite support, love, encouragement, inspiration, and advice whenever I feel a heavy load on my shoulders. Her presence in my life is the source of my strength to give the best of me, every day. Cristy, you are my favorite person in the world, and my best friend. I would like to dedicate this dissertation to you. Let’s go for the next adventure.

Chapter 1

Introduction

1.1 Background and motivation

Sintering is a method conventionally used for the bonding and compression of a powder into a bulk solid body, being a popular manufacturing technique for products of a wide variety of applications at many scales. Among them are electroceramic materials. Electronic components are formed by the integration of parts made from different sorts of materials, such as metals, polymers or ceramics. The processes required for such integration are constrained by the physical properties of the materials being used. Since generally polymers and metals have lower melting points than ceramics, the sintering of ceramics for the production of devices such as Low Temperature Co-fired Ceramics (LTCC), requires a reduction in processing temperatures to maintain the desired properties of the design.

To fabricate electronic components such as varistors and LTCC substrates, the cold sintering process (CSP) emerges as an attractive alternative for innovative designs of such integrated products. Cold sintering is a ceramic processing technique that allows the compaction of ceramic powders at temperatures below 300°C under the application of a uniaxial pressure of a few hundred MPa, while the process is assisted by the temporary presence of a liquid transient phase. Achieving densifications above 95 % of the theoretical density through cold sintering is possible by mixing a ceramic powder with a suitable solvent. The compact is subsequently pressed and heated to the sintering temperature for a certain period of time. During the cold sintering process, the contact points between ceramic grains, where capillary force increases the chemical potential, are preferentially dissolved into the liquid phase. This chemomechanical phenomenon causes the dissolved ions to migrate and precipitate on the grain surfaces adjacent to pores, leading to the densification of the ceramic at low temperatures, preventing the development of unwanted secondary phases, and addressing a technical challenge encountered in conventional sintering methods.

Previous studies have confirmed the feasibility of cold sintering to incorporate novel phases and materials, such as polymers[1–6], 2-D materials [7, 8], and buckminsterfullerene [9], at the grain boundaries of a ceramic matrix, demonstrating its remarkable advantage for the design of grain boundary engineered ceramic matrix composites.

Cold sintering has therefore potential to be the medium for the fabrication of innovative composite materials that would address the growing demand of modern communication technologies for substrate materials with low dielectric loss (*tan* δ) and high thermal conductivity (κ), to provide more bandwidth at higher operating frequencies. Cold sintering also provides the opportunity to explore and propose material systems with new microstructural designs for electronic components, which could help to advance the technology of electronic devices, such as varistors, yielding to a better understanding of electrical conduction mechanisms at the grain boundaries of composites.

1.2 General objective and specific goals

The general objective of this dissertation is to investigate several functional ceramic composites, by analyzing and correlating the nature of the individual inherent properties of their components, with respect to the effective properties of the bulk composite, using a designed microstructure enabled by the Cold Sintering Process. This investigation involves different composite material systems and their physical properties. Understanding the local interfacial nature of the functionality of grain boundaries can provide guidance for the development of future novel compositions designed with cold sintering process.

The specific goals driving the motivation for this dissertation are:

1) To integrate an electrically functional ferroelectric polymer at the grain boundaries of a zinc oxide matrix, via cold sintering, and to model the electrical conduction mechanism.
2) To improve the properties of a low permittivity ceramic system for microwave substrate applications, by designing and cold sintering composites that incorporate fillers with high thermal conductivity, while keeping a low dielectric loss and high electrical resistivity, at operating frequencies in the microwave regime.
3) To identify the underlying densification mechanisms of ceramic composites undergoing cold sintering, and to assess how the included fillers affect the densification process.

This dissertation documents in Chapter 4, the integration, for the first time, of a ferroelectric polymer at the grain boundaries of zinc oxide through the cold sintering process, for varistor applications. The investigation of the grain boundary phase confirms the preservation of the polymer's ferroelectric properties, analyzes the electrical conduction mechanisms at the grain boundary, and confirms the polymer's thicknesses to the dimensions predicted from the various electric measurements and subsequent phenomenological modeling.

Previous investigations have been made in the cold sintering of low loss dielectrics with ceramic matrix composites. [10, 11, 20, 21, 12–19] Before the work completed in this dissertation, there have been no attempts to consider composites that maintain high frequency dielectric properties and high electrical resistivity, while simultaneously enhancing thermal properties. Chapters 5 and 6 document the development of cold sintered composites using sodium molybdate ($Na_2Mo_2O_7$, NMO) as the ceramic matrix, using high thermal conductivity (κ) fillers such as hexagonal boron nitride (hBN) and microsized diamond (md). Analysis of their physical properties revealed the practicality of these composites for applications of microwave substrates of high power and frequency.

An investigation of the multiple creep mechanisms driving densification of NMO-hBN and NMO-md composites undergoing cold sintering is documented in Chapter 7. This work is based on previous studies that identify pressure solution creep as the densification mechanism for cold sintering, following the Woolfrey-Bannister method. This type of study is conducted in cold sintered ceramic matrix composites for the first time. The analysis of secondary (steady state) creep during isothermal conditions is documented as function of filler volume fraction, temperature and variations of the applied uniaxial pressure.

Finally, considering the successful and promising results described in Chapter 7 for the NMO-hBN composites, Chapter 8 describes preliminary results of proposed future work for the cold sintering of pure hexagonal boron nitride.

Chapter 2

Literature Review

2.1 Sintering

Sintering is one of the oldest material fabrication techniques for making ceramic materials. It entails the application of thermal energy to a granular body to drive it into a dense ceramic monolith.

For more than 20,000 years, sintering has been used for the fabrication of stoneware, pottery, and many other applications of ceramic materials.[22] As humanity advances, so has our understanding of the sintering processing and has made possible the processing of incredibly complex and technologically critical materials and devices such as ceramic cutting tools and bearings, electronic packaging materials, catalytic converters, membranes for filtration processes,[23] multilayer ceramic capacitors (MLCC), solid oxide fuel cells (SOFC), and refractories,[24] among others. Thus, a strong understanding of its fundamental mechanism is critical for the advancement of such materials and devices.

The principles to understand sintering begin with the premise that all materials inherently have surfaces. By nature, these surfaces are unstable because the atoms at these locations contain missing or "broken" bonds. The energy of the interface at this surface[25] can be described as:

$$\gamma_S = \left(\frac{dE}{dA}\right)_{T,P,n_i} \qquad \text{(Eq. 2.1)}$$

Accordingly, globally, within a powder compact, there is a driving force for the elimination of excess surface free energy. And so, when substantial thermal energy is applied to activate the diffusion of atoms, the system will begin to eliminate this surface free energy. However, this can occur in two ways. First, it may be by transforming the interface type, from a high energy surface (solid-vapor, or solid-liquid) interface to a lower energy grain boundary (solid-solid) interface. The second could be by decreasing the total amount of surface area, by the growth or fusing of grains. The former is a densifying mechanism, while the latter would be a non-densifying mechanism. During sintering both operate concurrently, and so there is a competition between pathways for eliminating surface free energy. This can be understood as such:

$$\Delta(\gamma A) = \Delta\gamma A + \gamma\Delta A \qquad \text{(Eq. 2.2)}$$

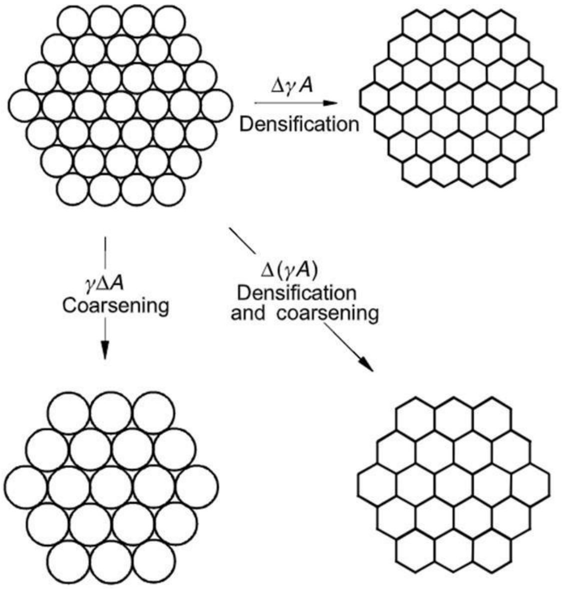

Figure **2-1**: Basic phenomena occurring during sintering under the driving force for sintering, $\Delta(\gamma, A)$. Figure reproduced from reference.[25]

Generally, the thermal energy needed to activate the diffusional process, and densify most ceramic materials is $\gtrsim$ 1000°C, with totally processing times ranging between ~2 – 10 hours. And so, not only is sintering a very thermally and energy intensive process, but the range of materials that can be processed, or co-processed is limited.

Additionally, with Earth's rising temperatures, as result of greenhouse gas emissions driving climate change, there is a motivation for the decarbonization across all industrial sectors. The ceramics industry is not exempt from this pressing issue.[26, 27] Motivated by these pressing issues, and the limitations on the processing & co-processing of less stable materials imposed by the high thermal inputs necessary for densifying ceramics, scientists have been researching novel processing methods. Jantunen's research group published in 2014 the dielectric properties of a lithium molybdate bulk ceramic fabricated at room temperature,[11] and the Randall's group in 2016 began the publication of a series of dielectric material systems fabricated via cold sintering.[28]

2.2 Cold sintering process

The cold sintering process circumvents the thermal input necessary for densification, by mixing the granular powder with a liquid phase in which it is soluble in. This mixture is then uniaxially pressed and heated to moderate temperatures. And so, pressure differences between the stressed grain boundaries, and less stressed pores, drives diffusion from these contact areas to the pores, resulting in densification. As the system is open, because of a finite area between the punch of the idea, and die wall, the liquid phase is additionally transient, and is ejected during the sintering process.

Temperature for cold sintering generally ranges between 150°C - 400°C, and pressure of a few hundred MPa. With the cold sintering process, numerous ceramic-polymer, ceramic-metal, among other composites have been successfully densified to realize uniquely engineering materials and interfaces. Additionally, less stable ceramic materials have been successfully densified, that either decompose or transforms to another crystal structure at the more elevated temperatures that a material experiences under conventional sintering conditions.

While the science of cold sintering is still emerging, it is believed that the mechanism driving such densification is pressure solution creep (PSC). Pressure solution creep is a geologically observed diffusional creep mechanism, whereby pressurized granular matrix in the Earth's crust, with an intergranular fluid, will densify. Pressure solution creep is a 3 step process involving dissolution at the stressed grain boundaries, transport of the dissolved material from the grain boundaries, to the pores, and reprecipitation of this material at the pores, This serial 3 step process can be visualized in Figure 2-2.

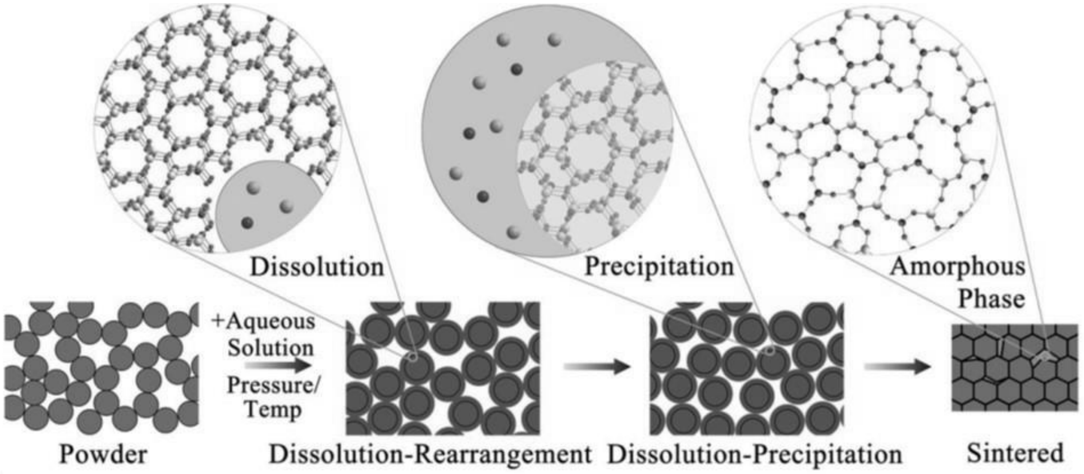

Figure **2-2**: Schematic evolution of a powder compact during cold sintering. Interfaces at the grain boundary region in dominant stages have been magnified. Figure reproduced from reference.[29]

While whether the PSC mechanism is the one driving densification during cold sintering is under debate, there is substantial circumstantial evidence demonstrating that it is.[30, 31] However, in line with the evolution of sintering as previously explained, the profound understanding of these diffusional creep mechanisms governing densification and growth is critical for the development of future materials and devices.

2.3 Cold sintering of ceramic composites

As mentioned in the previous section, cold sintering circumvents the limitations of high temperatures for the co-processing of ceramics with filler materials. This provides a powerful technique for the design and fabrication of ceramic composites with a wide range of fillers e.g. such as polymers (thermoplastics and thermosets)[1–6], 2-D materials[7, 8], and buckminsterfullerene[9].

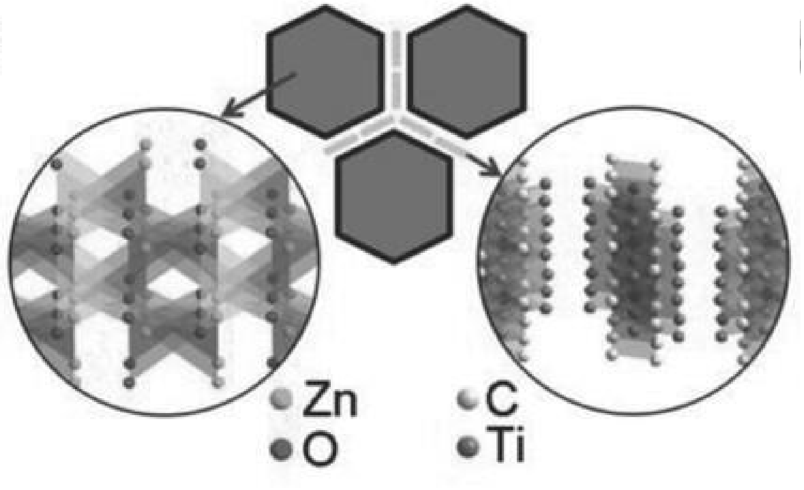

Figure **2-3**: Schematic illustration of the grain boundary of the cold sintered MXene ZnO–$Ti_3C_2T_x$ nanocomposite. Figure reproduced from reference.[7]

The diversity of applications of such cold sintered composites includes electronic packaging, capacitors, sensors, radio frequency devices, semiconductor oxides substrates, catalyst supports, ionic conductive electrolytes, lithium cathodes, varistors, multilayer ceramic capacitors (MLCC), low temperature co-fired ceramic (LTCC) substrates, to name a few, exposing the potential of a vast number of technological applications. Table 2-1 provides a collection of published articles on cold sintered composite systems, including those addressed in this dissertation.

The mentioned cold sintered composites are commonly modeled with a matrix of insulating or semiconducting polycrystalline ceramic materials, and fillers that can have different morphologies and physical characteristics, for which the properties are partly associated with how their constituent materials are arranged and processed. To design composites, there are three general factors that must be considered: (1) connectivity, (2) volume fractions and (3) selection of materials. The following sections describe the convention and nomenclature proposed by Newnham for the connectivity of composites,[32, 33] and models commonly used to quantify the contribution of each phase to the bulk material's effective properties, according to their corresponding volume fraction.

Table **2-1**: Cold sintered composite material systems.

Composite Systems	Potential applications	Reference
V_2O_5-PEDOT:PSS	Semiconductor oxide, NTC material	34, 35
V_2O_5-CNF	Catalyst support, sensor, Li cathode	36
$LiFePO_4$-Carbon-PVDF	Li cathode	37
Li_2MoO_4-PTFE	Packaging substrate	38
LAGP-PVDF:HFP	Electrolyte	38
ZnO-PTFE	Varistor	39
ZnO-$Ti_3C_2T_x$ MXene	Varistor, thermoelectric, optoelectronics, piezoelectric transducer, photocatalyst, sensor	7
ZnO-PDMS	Varistor	40
ZnO-PEI	Varistor, LTCC device	41
ZnO-PEEK	Varistor	42, 43
ZnO-PEEK-Bi_2O_3-MnO_2-Co_2O_3-Cr_2O_3	Varistor	43
$Na_2Mo_2O_7$-PEI	LTCC packaging, substrate	44
$Na_2Mo_2O_7$-hBN	LTCC packaging, microwave substrate	* 45, 46
$Na_2Mo_2O_7$-diamond	LTCC packaging, microwave substrate	*
MoS_2-Graphite	Li electrode	47
LAGP-LiTFSI	Ionic conductive electrolyte	48
LATP-LiTFSI	Ionic conductive electrolyte	48
SiO_2-PTFE	Dielectric material	49
$BaTiO_3$-PTFE	MLCC	2, 50, 51, 52
$BaTiO_3$-PPO	MLCC	53
PZT-$Pb(NO_3)_2$	Piezoelectric transducers, actuators and sensors	54, 55
LLZO/SM-PPC/$LiClO_4$	Ionic conductive electrolyte	56
NVP-CNF	All-solid-state cathodes	57, 58
NVP-NZSP	All-solid-state cathodes	57, 58
NBMO−Li_2MoO_4	Microwave dielectric	59
BLVMO-$Na_2Mo_2O_7$	Microwave dielectric	16
$BaBiLiTeO_6$-Li_2MoO_4	Microwave substrate, antenna	60
$BaBiLiTeO_6$-PTFE	Microwave substrate, antenna	60
*Work in this dissertation.		

2.4 Connectivity of phases in a composite

The connectivity of a composite describes the spatial distribution for the matrix and filler phases. Newnham defined a nomenclature to explain wide variations of different types of connectivities, where a value of ‘0’ means ‘no connection’, a value of ‘1’ corresponds to a phase being self-connected in one direction, and a value of ‘3’ to a phase interconnected in all the three orthogonal directions. The established convention of this approach indicates first the filler’s condition and secondly the matrix. For example, a 1-3 pattern would be characteristic of an extrusion process, while 2-2 could correspond to a laminated composite of multilayered ceramic insulator and metal electrodes.[32, 33, 61]

The number of possible connectivity patterns *N* for a given system depends on the number its components n, and is related by the expression:

$$N = \frac{(n+3)!}{3!\,n!} \qquad \text{(Eq. 2.3)}$$

2.5 Volume fractions in a composite

The matrix and filler elements of a composite are selected to have different physical properties, and their influence on the effective properties of the bulk composite are reflected partially in proportion with their volume fraction. Percolation theory and mixing laws are important principles used to design the desired properties of the composite.

2.5.1 Percolation theory

The properties of a composite are influenced by the volume fraction of its matrix and filler phases. The more filler is added to the matrix, the more the properties of the composite will approach that of the filler, until the "percolation limit" is reached at an inflection point.[62, 63] The set of equations that model a physical property of a composite material according to percolation theory, is composed of two sections. The fitting curve below the percolation threshold is described by the Equation 2.4:

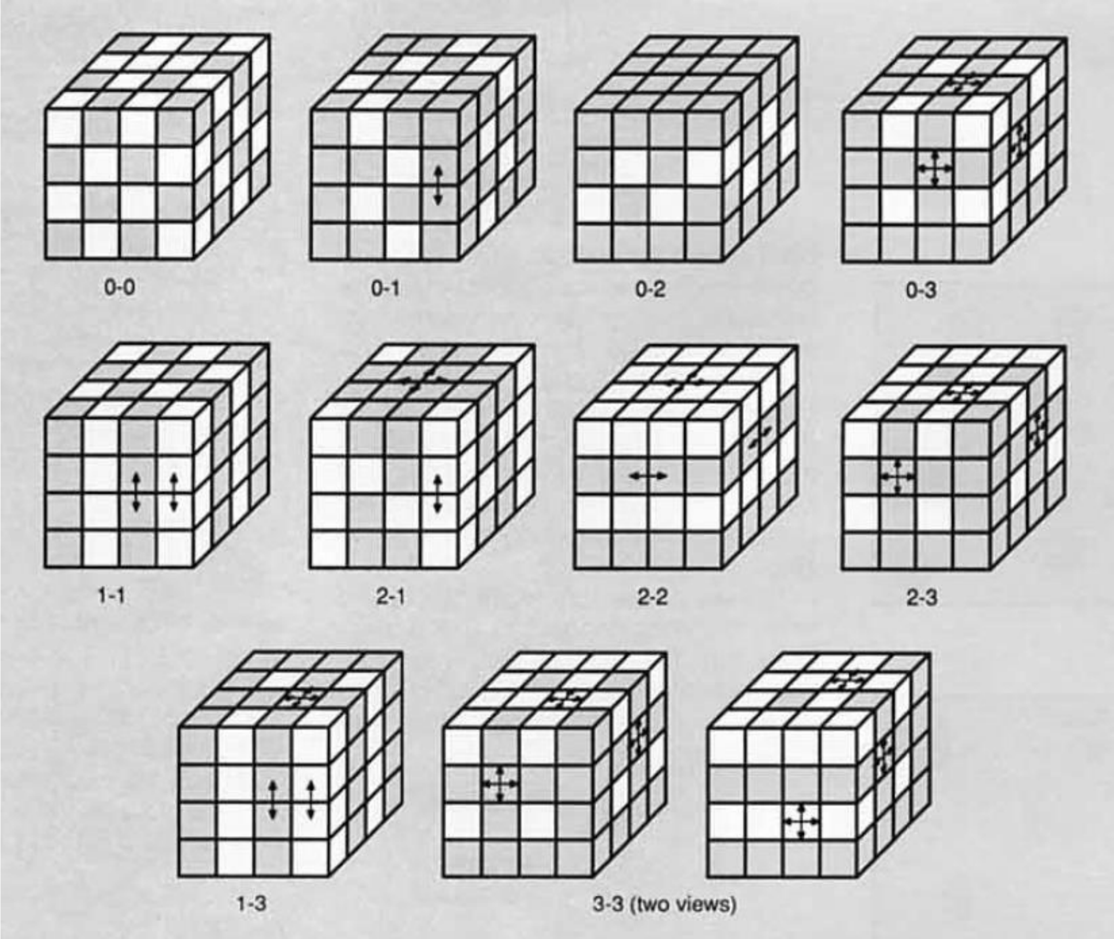

Figure **2-4**: Connectivity patterns of a composite, labeled after the nomenclature developed by Newnham. Figure reproduced from reference.[61]

$$\rho = \rho_m \left(\frac{\varphi_c - \varphi_f}{\varphi_c}\right)^{-s} \qquad \text{(Eq. 2.4)}$$

where ρ is the effective resistivity of the composite, ρ_m is the resistivity of the ceramic matrix, ϕ_f is the volume fraction of the filler, ϕ_c is the percolation threshold, and s is a critical exponent. Above the percolation threshold, the fitting equation is:

$$\rho = \rho_f\left(\varphi_f - \varphi_c\right)^t \qquad \text{(Eq. 2.5)}$$

where ρ is the effective resistivity of the composite, ρ_f is the resistivity of the filler, ϕ_f is the volume fraction of the filler, ϕ_c is the percolation threshold, and t is the critical exponent corresponding to the percolation theory.[64]

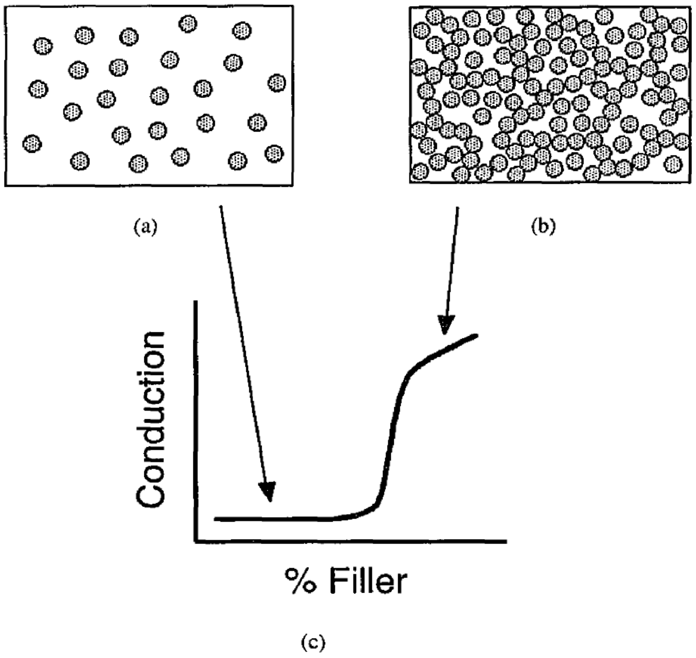

Figure **2-5**: In agreement with percolation theory, (a) Low volume fraction of a conducting filler in an insulating matrix yields to low conductivity of the composite, (b) High volume fraction of a conducting filler yields to highly conductive composites, (c) The inflection point in the plot determines the percolation limit. Figure reproduced from reference.[62]

2.5.2 Mixing rules for composite dielectric materials

There are a number of properties for which the composite property coefficient depends on the corresponding coefficients of their constituent phases.[33] Some of these properties include the dielectric permittivity, elastic stiffness, and magnetic permeability, to name a few. To determine the effective permittivity (ε_{eff}) of a composite, several models have been proposed by calculating the effect of the permittivity of each phase and their arrangement within the microstructure. An initial model presented by Clausius and Mossotti offers an equation to calculate the effective permittivity of a composite, considering uniformly distributed spherical fillers. Later, Maxwell proposed a mixing rule which was useful to fit experimental data with spherical fillers. Lichtenecker's mixing rule (Figure 2-6) is based on statistical principles that allow for deviations in the particles' geometry, considering filler orientations that are connected in series or parallel, in reference to the applied electric field. For a microstructure with uniformly distributed and randomly oriented fillers, modeled as a mixture of series and parallel connections among the phases, Lichtenecker's mixing rule is commonly known as the logarithmic mixing rule.[2, 64–70] Table 2-2 provides the equations of some of the commonly used mixing rules for composite dielectric materials.

Table **2-2**: Mixing rules for effective permittivity (ε_{eff}) of heterogeneous composites, where ε_1 is the relative permittivity of matrix, ε_2 is the relative permittivity of filler, and θ is the volume fraction of filler.

Mixing rule	Equation	
Clausius-Mossotti First mixing rule for heterogeneous dielectric models. Spherical fillers are assumed.[70]	$\frac{\varepsilon_{eff}}{\varepsilon_2} = \frac{(\varepsilon_1 + 2\varepsilon_2)(\varepsilon_2 - \varepsilon_1)^{-1} - 2\theta}{(\varepsilon_1 + 2\varepsilon_2)(\varepsilon_2 - \varepsilon_1)^{-1} + \theta}$	(Eq. 2.6)
Maxwell Good fit to experimental data. Spherical fillers are assumed.[71]	$\frac{\varepsilon_{eff}}{\varepsilon_1} = \frac{2\varepsilon_1 + \varepsilon_2 + 2\theta(\varepsilon_2 - \varepsilon_1)}{2\varepsilon_1 + \varepsilon_2 - \theta(\varepsilon_2 - \varepsilon_1)}$	(Eq. 2.7)
Rayleigh Approach from *Clausius-Mossotti* for dilute dispersions (θ <<1)[70]	$\frac{\varepsilon_{eff} - \varepsilon_2}{\varepsilon_{eff} + 2\varepsilon_2} = \frac{\theta(\varepsilon_1 - \varepsilon_2)}{\varepsilon_1 + 2\varepsilon_2}$	(Eq. 2.8)

Fricke Includes a "shape factor" (x') for prolate or oblate spheroidal inclusions.[72]	$\varepsilon_{eff} = \dfrac{\varepsilon_1\varepsilon_2(1+x'\theta)+\varepsilon_2{}^2x'(1-\theta)}{\varepsilon_{eff}(1-\theta)+\varepsilon_2(x'+\theta)}$	(Eq. 2.9)
Hashin-Shtrikman Defines upper and lower bounds for spherical fillers coated by a shell of matrix.[65]	$\varepsilon_{HSL} = \varepsilon_2 + \dfrac{\theta}{(\varepsilon_1-\varepsilon_2)^{-1}+\dfrac{1-\theta}{3\varepsilon_2}}$ $\varepsilon_{HSU} = \varepsilon_1 + \dfrac{1-\theta}{(\varepsilon_2-\varepsilon_1)^{-1}+\dfrac{\theta}{3\varepsilon_1}}$	(Eq. 2.10) (Eq. 2.11)
Banno Derived from remanent polarization of ferroelectric ceramics as function of closed pores, based on a modified cubes model.[66]	$\dfrac{1}{\varepsilon_{eff}} = \dfrac{1-\theta}{\varepsilon_1}+\dfrac{\theta}{\varepsilon_2}$	(Eq. 2.12)
Lichtenecker **General expression** From statistical principles, allows for deviations in particles' geometry.[69]	$\varepsilon_{eff}^n = \theta\varepsilon_1^n + (1-\theta)\varepsilon_2^n$ $where\ (-1 \leq n \leq 1)$	(Eq. 2.13)
Lichtenecker, n = -1 Boundary condition where the filler material is connected in **series** with the applied electric field.[69]	$\dfrac{1}{\varepsilon_{eff}} = \dfrac{\theta}{\varepsilon_2}+\dfrac{(1-\theta)}{\varepsilon_1}$ $where\ n = -1$	(Eq. 2.14)
Lichtenecker, n = 1 Boundary condition where the filler material is connected in **parallel** to the applied electric field.[69]	$\varepsilon_{eff} = \theta\varepsilon_2 + (1-\theta)\varepsilon_1$ $where\ n = 1$	(Eq. 2.15)
Lichtenecker, n = 0 The filler material is evenly **mixed** in series and parallel connections with respect to the applied electric field. Commonly known as logarithmic mixing rule.[69]	$log\varepsilon_{eff} = \theta log\varepsilon_2 + (1-\theta)log\varepsilon_1$ $where\ n = 0$	(Eq. 2.16)

The selection of the mixing rule to be employed should be determined upon the microstructural design of the investigated composite system. In the following chapters of this dissertation, the relationship between each composite system model and the mixing rule employed for its analysis will be further discussed.

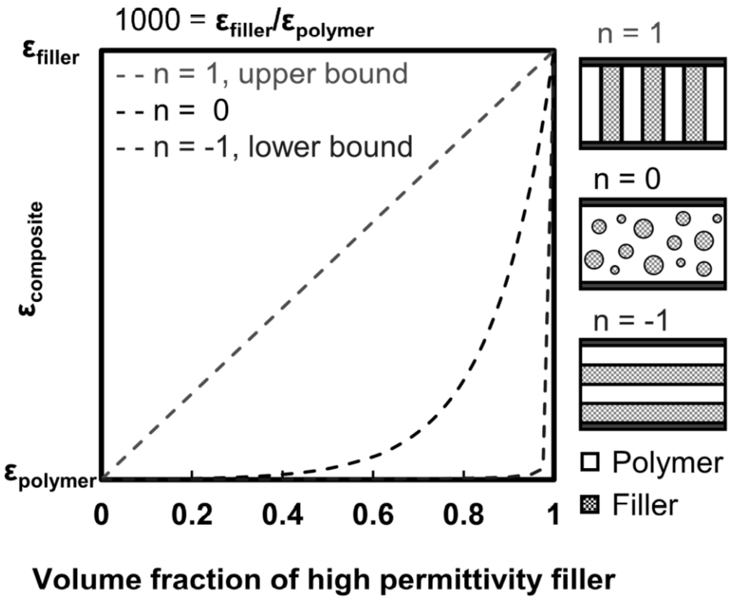

Figure **2-6**: Effective permittivity of electroceramic composite as a function of the filler's volume fraction calculated using Lichteneker's mixing rule. Figure reproduced from reference.[2]

2.6 Zinc oxide varistors

Zinc oxide is one of the most frequently used materials for the fabrication of Voltage-Dependent Resistors (VDR), also commonly known as Varistors. This type of electronic component is used to protect a circuit connected in parallel from high voltage discharges, and it does so by varying its resistance value in response to the magnitude of the applied voltage. Miller, Moulson and Herbert, Levinson, and Philipp, are some of the researchers who have extensively studied and reported the relation between the structure and properties, including the conduction mechanisms of ZnO varistors.[39, 71, 73–75] They have defined the current-voltage (I-V) non-ohmic response of VDRs by the equation

$$I = KV^{\alpha} \qquad \text{(Eq. 2.17)}$$

where I is the current, V is the applied voltage, K is a proportionality constant and α is the exponential term corresponding to the non-linear response.

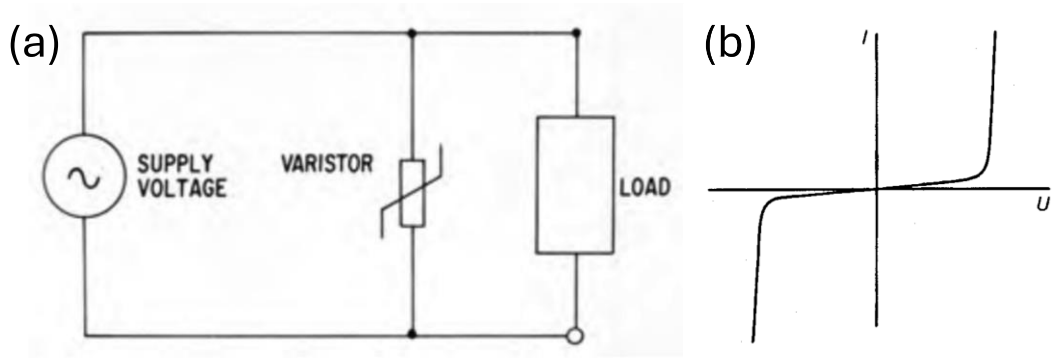

Figure **2-7**: (a) Application of ZnO varistor as protective component. (b) Current (I) – voltage (U) relation for a ZnO varistor. Figure adapted from reference.[74]

The VDR behavior of ZnO results from electron states that are formed on the surfaces of the crystals as a consequence of their discontinuity. These surface states act as acceptors for electrons from the crystal, which acts as a n-type semiconductor. Electrons will be withdrawn from the region near the surface and replaced by a positive space charge. This will give rise to two oppositely oriented Schottky barriers on each side of the intergranular layer (IGL), limiting the flow of electrons from one grain to its neighboring one. Therefore, when a voltage is applied to the varistor element, electrons flow from the grain to the IGL at the forward biased junction, while at the reversed biased junction thermally activated electrons will flow from the IGL into the grain at low voltages, and electrons will tunnel in the same direction at high voltages.[7, 72, 76, 77]

The flow of thermally activated electrons that occurs in the reverse biased junction at low voltages can be described by the Schottky Thermionic Emission phenomenon by the equation

$$J = AT^2 \exp\left(\frac{\beta {E_{GB}}^{1/2} - q\Phi_B}{k_B T}\right) \qquad \text{(Eq. 2.18)}$$

where J is the current density, A is a proportionality constant, T is the temperature, β is

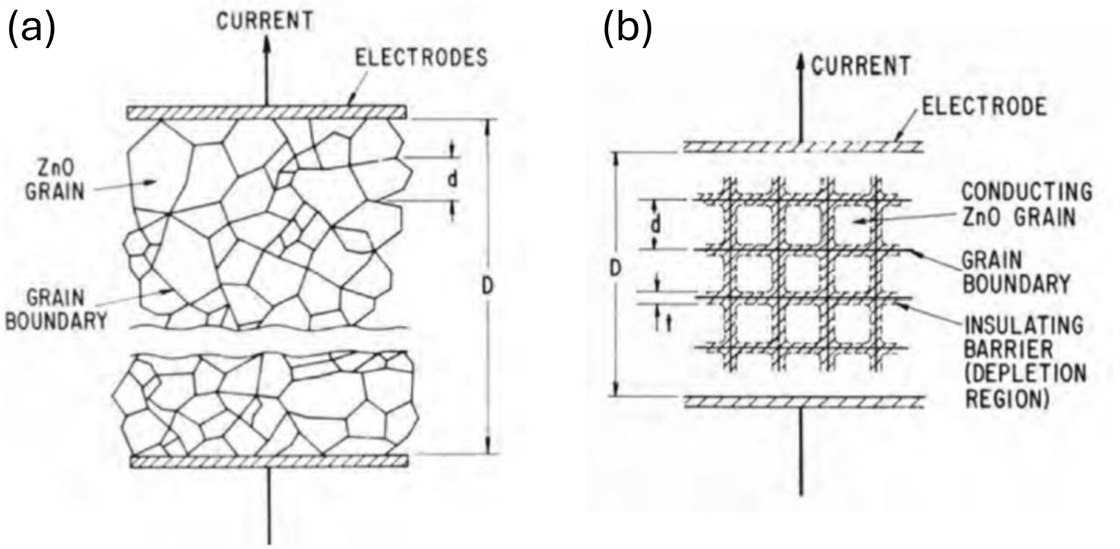

Figure **2-8**: (a) Schematic of a typical polycrystalline microstructure in a ZnO VDR. The average grain size is represented by d. (b) Block model of ZnO varistor. The IGL depletion layer is represented by t. Figure adapted from reference.[74]

determined by the slope ($=\beta/k_BT$) in the Schottky Emission plot ($ln(J/T^2)$ *vs* $E_{GB}^{1/2}$), E_{GB} is the applied electric field and $q\varphi_B$ is the Schottky barrier height. The $q\varphi_B$ can be calculated from Eq. 2.18 at E_{GB}=0 by

$$q\Phi_B = -k_B\, T\; *\, ln\left(\frac{J}{T^2}\right) \qquad \text{(Eq. 2.19)}$$

For high voltages, the quantum mechanism known as Fowler-Nordheim tunneling takes place allowing the flow of electrons from the IGL into the ZnO grain at the reverse biased junction. This quantum conduction mechanism is described by the equations

$$J = AE_{GB}{}^2 \exp\left(-\gamma/E_{GB}\right) \qquad \text{(Eq. 2.20)}$$

$$\gamma = \frac{8\pi\sqrt{2m^*}}{3qh}\left(q\varphi_B\right)^{3/2} \qquad \text{(Eq. 2.21)}$$

where γ is an activation term, q is the elementary charge, h is the Planck constant and m^* is the effective mass of tunneling.

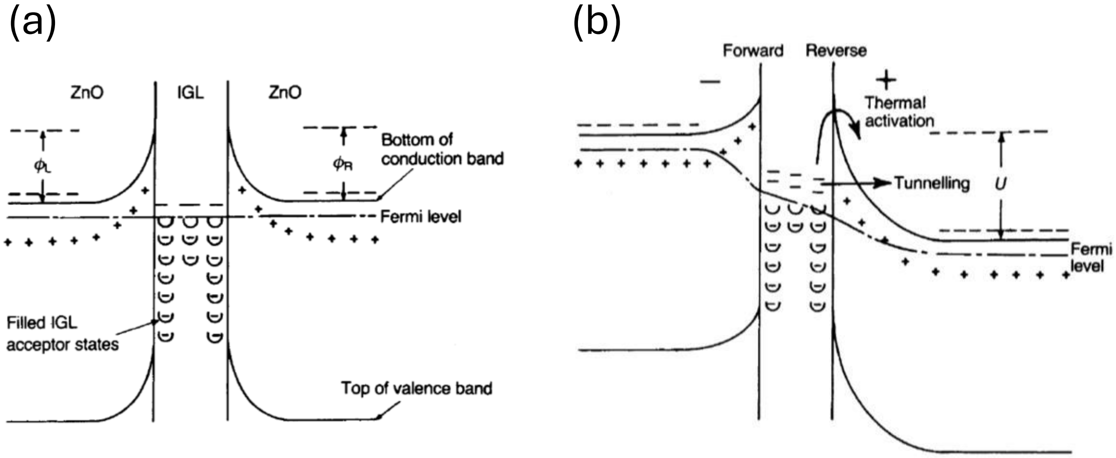

Figure **2-9**: Descriptive diagrams of the Schottky thermionic emission (thermal activation) at low voltages and Fowler-Nordheim quantum mechanism (tunneling) at high voltages (a) when no voltage is applied, and (b) with applied voltage. Figure adapted from reference.[71]

2.7 Microwave ceramic substrates

Electronic packages are sophisticated combinations of glasses, ceramics, and metals that provide the necessary mechanical support and rigidity to produce a reliable, functional circuit, to form compact, cost-effective solutions for a variety of applications.

Substrates constitute the fundamental building blocks of any electronic product, on which circuit traces and components are mounted and supported, enabling the connectivity of the different elements in a circuit assembly.

Ceramic substrates provide high wiring density capabilities due to their feasibility to be processed into multilayered cofired substrates. They also exhibit a high chemical resistance to tolerate processing chemicals used in etching and plating. A highly dense ceramic with low porosity is desired to avoid the entrapment of moisture or contaminants that could cause malfunctions such as arcing, tracking or metal migration.[78]

Among the appropriate physical properties for ceramic substrates, a low relative permittivity (ε_r) is the most important one, because the parasitic capacitance effects to the circuit are directly proportional to the dielectric constant. A low dielectric loss ($tan\ \delta$) is necessary to limit the electrical losses in the substrate material, which can be exacerbated at higher operating frequencies. High electrical resistivity (ρ) and high breakdown voltage (E_b) are required to prevent electrical leakage current between the conductor tracks on the substrate, especially in high power applications. High thermal conductivity (κ) is desired to dissipate the heat produced by the active electronic components mounted on the substrate. An appropriate Coefficient of Thermal Expansion (CTE) matching the expansion coefficients of the other components of the assembly, would minimize the thermal-mechanical stresses of the connections during thermal and power cycling.[79]

Considering the desired properties listed above, some of the most popular, and therefore, widely used ceramics in the industry include $Mg_2Al_4Si_5O_{18}$ Al_2O_3, SiC, Si_3N_4, AlN, and SiO_2.[78–80] These substrates can be fabricated into electronic components or circuits using thin-film, conventional additive thick-film, or multilayer ceramic technologies. The multilayer technology of low temperature cofired ceramics (LTCC) is popular for applications that require hermetic packages and very high circuit densities, and it has been gaining popularity for microwave applications due to its design flexibility and low loss at higher frequencies. This particular capability positions ceramic substrates as an excellent alternative for advanced communication technologies operating at frequencies of tens or hundreds of GHz. Other popular applications for ceramic substrates include high-power circuits such as motor drives and power conversion equipment.[80]

Chapter 3

Experimental Methods

The experimental methods are discussed within each chapter of this thesis. This includes the raw materials used in the synthesis steps. In addition, details of the processing steps are discussed to aid future researchers' verification of the processing. This thesis involves a large number of characterization methods covering property determinations of electrical conduction and dielectric properties across a variety of frequencies and temperatures, along with thermal conductivity properties. To complete the structural-property-process-performance relations, the studies utilized structural analysis throughout to aid the successful formation and understanding of the various composites. The structural analysis includes x-ray diffraction and FTIR spectroscopy, along with microstructure analysis with electron microscopy methods such as scanning electron microscopy and transmission electron microscopy. Energy X-ray dispersive imaging was also used to determine the chemical gradients and phase distributions of the composites throughout the investigation.

Chapter 4

Integration of a Ferroelectric Polymer at the Grain Boundaries of Zinc Oxide via Cold Sintering

In this study, the cold sintering process (CSP) is used to design ceramic-polymer composites with polyvinylidene fluoride trifluoroethylene (PVDF-TrFE), a ferroelectric co-polymer, as an active intergranular grain boundary phase in a semiconducting zinc oxide (ZnO) electroceramic matrix. The conductivity is modelled with Schottky thermionic emission and Fowler-Nordheim tunneling as a function of both temperature and voltage. In addition, the dielectric characterization shows a high effective permittivity resulting from a space charge relaxation of the PVDF-TrFE. The Maxwell-Wagner-Sillars (MWS) model was used to predict ~ 3 nm as the thickness of the intergranular PVDF-TrFE phase controlling the electrical properties of the composite. Transmission electron microscopy (TEM) investigation of the grain boundary phase confirms the polymer thicknesses at the dimensions predicted from the electric measurements and modeling.

4.1 Introduction

Cold sintering offers unique opportunities to design composites with a wide variety of materials that are typically difficult or impossible to co-process. Cold sintering uses a non-equilibrium thermodynamic chemo-mechanic process known as pressure solution creep to drive diffusion at extremely low temperatures to permit inorganic particulate materials to sinter into a dense body with over 95 % theoretical densities.[29] To enable this process, a transient chemical phase along with an applied pressure and temperature is used to drive a series of consecutive mechanisms, namely dissolution at the compressed contact points between particles, diffusion of solute along the grain boundaries and reprecipitation at pore surfaces, following local chemical potential gradients.[31, 81–83] The transient phases must be carefully considered to drive the kinetics of these processes, to permit the densification at pressures on the order of a few tens of MPa, and temperatures below 400°C.[84] Figure 4-1 shows a schematic of these pressure solution creep processes enabling the low temperature sintering of the bulk materials, multilayers, or composites.[19, 26, 85–88] In cold sintering, various passive insulating polymers of different types have been successfully integrated at the nanometer scale into the grain boundaries. These include thermosets such as PDMS (Polydimethylsiloxane)[89] and thermoplastics such as PTFE (Polytetrafluoroethylene)[1], PEEK (Polyether ether ketone)[42], PEI (Polyethylenimine)[90], and PPO (Poly(p-phenylene oxide)[53], among others. In this study, a more electrically functional co-polymer was considered: PVDF-TrFE. PVDF-TrFE is a semicrystalline system with two crystalline polymorphs: a non-ferroelectric a-phase and a ferroelectric β-phase. The β-phase can undergo a ferroelectric to paraelectric phase transformation at $T_C \sim 124°C$, has a relative permittivity or dielectric constant of $\varepsilon_r \sim 11$ at 1 kHz, and melting point at $T_m \sim 150°C$.[91] These are subject to change, depending on crystallinity and the physical confinement of PVDF-TrFE.[92] The objective of this study is to incorporate a ferroelectric polymer into the grain boundary of a densified ZnO, to form a new type of nanocomposite and investigate the associated varistor electrical properties with respect to the microstructure with non-linear conduction models.

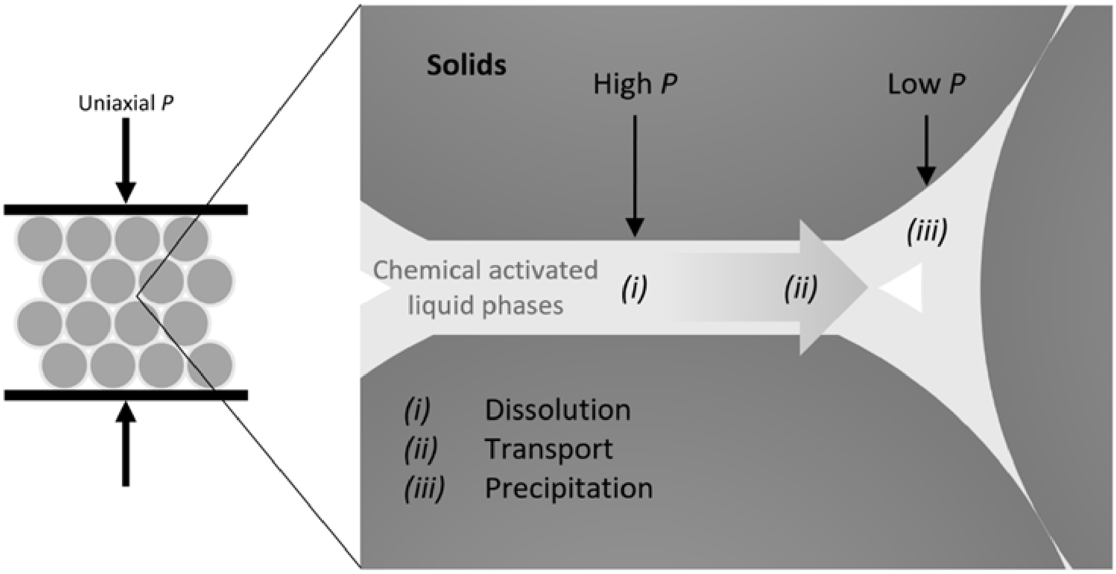

Figure **4-1**: Schematic illustration of the pressure solution creep mechanism that drives the sintering of bulk materials in cold sintering, Figure adapted from reference[85] with permission.

4.2 Materials and methods

4.2.1 Selection of materials

4.2.1.1 Zinc oxide

Zinc oxide (ZnO) is a direct wide band gap *n*-type semiconductor ($E_g \sim 3.3$ eV). It has the wurtzite structure, Space group $P6_3mc$, Point group *6mm*, which allows pyroelectric properties along <001>. The interest in ZnO for CSP investigations lies in its recognized properties for applications in varistors, phosphors and transparent conducting films, to name a few.[1, 7, 93–95]

4.2.1.2 PVDF-TrFE copolymer

Polyvinylidene fluoride (PVDF) and Trifluoroethylene (TrFE) are commonly used ferroelectric polymers in the electrocomponents industry.[96] The widely studied copolymer PVDF-TrFE presents an average molar mass $M_W = 560 - 880$, a number average molar mass $M_N = 190 - 320$ and Dispersity index $M_W/M_N = 2.6 - 2.9$ (per 75/25 mol Arkema Piezotech FC^{TM} 25 Data Sheet), average density $\rho = 1.88$ g cm^{-3}, a ferroelectric to paraelectric phase transformation at $T_C \sim 118°C$, a dielectric constant $\varepsilon_r \sim 11$ at 1 kHz for room temperature, $\varepsilon_r \sim 45$ at 1 MHz for T_C, and melting point at $T_m \sim 150°C$.[91, 97]

4.2.2 Experimental methods

4.2.2.1 Powder preparation

Zinc oxide powder was obtained from Alfa Aesar (NanoArc^{TM} ZN-0605) and PVDF-TrFE was obtained from PolyK Technologies (75/25 mol Arkema Piezotech FC^{TM} 25). The PVDF-TrFE particles were cryo milled at -196°C for 9 cycles of low energy (5 motions/second for 60 seconds) and high energy (25 motions/second for 180 seconds) alternating milling steps using a Retsch Cryomill. Differential Scanning Calorimetry (DSC) was conducted on the PVDF-TrFE powder as received and after the cryomilling process, using a TA Instruments Q2000, first heating up the sample at 1°C/min, from 40°C to 170°C, and then cooling down the sample at -1°C/min from 170°C to 40°C.

4.2.2.2 Cold sintering process (CSP)

Dense pellets were fabricated by CSP, using 15 wt.% acetic acid (2 mol/L) manually mixed with ZnO powder and 2, 6 and 10 vol.% of PVDF-TrFE in an agate mortar for 10 min. The mixture was then put into a die (13 mm diameter) and uniaxially pressed at 300 MPa. The temperature of the die was increased from room temperature to 140°C at a heating rate of 20°C/min, then maintained at 140°C for 4 hours and finally cooled down to room temperature. Representative pictures of the powder preparation and pellet fabrication by cold sintering are shown in Fig. 4-S1 (Supporting Information). Reported relative densities of cold sintered pellets were obtained by dividing the bulk density (determined by the geometric method) and the theoretical density of ZnO or ZnO/PVDF-TrFE composites.

4.2.2.3 Materials characterization

Fourier Transform Infrared (FTIR) Spectroscopy was conducted on composite cold sintered pellet with 10 vol.% of PVDF-TrFE by attenuated total reflection (ATR) analysis with diamond ATR crystal. Microstructures were observed on fracture surfaces by Field Emission Scanning Electron Microscope (Thermo Fisher FESEM Verios G4) and grain-boundary-grain interfaces by Transmission Electron Microscopy (TEM Talos F200X) and Energy Dispersive Spectroscopy (EDS) mapping. ZnO/PVDF-TrFE samples were polished with a # 1200/P4000 sandpaper and ethanol. Conducting 200 nm thick platinum electrodes were deposited using a Sputter Coater (Quorum Q150R). Dielectric measurements were performed using a precision LCR meter (Keysight E4980A) at 1 MHz. The Current-Voltage (I-V) DC analysis was conducted using Hewlett-Packard 4140B pA Meter / DC Voltage source and a Trek model 10/10B-HS High voltage amplifier from 50 to 1000 V and temperatures in the 85-140°C range, with incremental steps of 50 V and 5°C, respectively.

4.3 Results and discussion

4.3.1 Fabrication of ZnO – PVDF-TrFE composite pellets by cold sintering

It is extremely important to optimize the homogeneity and control of the microstructures throughout the design of these nano-composites. So the processing steps need to be carefully considered towards this end. As an example, the critical processing steps for ZnO/PVDF-TrFE composite pellets fabricated via CSP were explored for volume fractions of 2, 6 and 10 vol.%. For homogeneous distribution of PVDF-TrFE powder in the ZnO matrix, the PVDF-TrFE powder was cryomilled, and the average particle size decreased from 98 μm to 9 μm, as illustrated in Figure 4-2. DSC was conducted on both the initial condition and the cryomilled PVDF-TrFE. Results of the DSC profiles indicated that the Curie Temperature (T_C) did not change after the particle size reduction as shown in Fig. 4-S2. Several DSC profiles were run presenting similar results, where T_C does not change even after several heating-cooling cycles, indicating that the ferroelectric activity of the material was preserved.

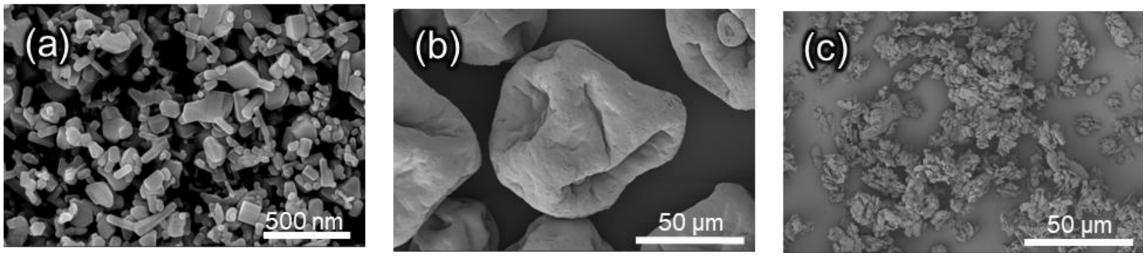

Figure **4-2**: SEM images of (a) initial condition of ZnO powder d = 142 nm, (b) initial condition of PVDF-TrFE powder d = 98 μm and (c) cryomilled condition of PVDF-TrFE powder d = 9 μm.

4.3.2 Analysis of structure-property relationships of the composites

As previously stated, a homogenous distribution of the ferroelectric polymer in the composite is essential to accurately interpret microstructure/properties relationships. Figure 4-3 illustrates the microstructure of ZnO/PVDF-TrFE composites with different volume fractions of the polymer. Composites with a volume fraction of PVDF-TrFE of 6 % and above (Figure 4-3.c,d) highlight polymer segregation within the microstructure. Segregation when using a high volume fraction of thermoplastic polymers was already observed in other cold sintered systems.[1, 89, 90] Smaller amounts of PVDF-TrFE with good dispersion can lead to less segregation, providing an intergranular polymer barrier through the microstructure, as shown in Figure 4-3.b for the sample with 2 vol% PVDF-TrFE. This impacts many of the electrical properties of the composite, and these signatures of dispersed polymer can be used to aid the processing control. Homogeneous distribution and minimum segregation of the polymer can be achieved and identified from relative simple electrical measurements. One example is the suppression of the dielectric loss relative to the samples with no polymer, as shown in Figure 4-S3.

The microstructure of the ZnO/PVDF-TrFE composite was analyzed by Transmission Electron Microscopy (TEM) and Energy Dispersive X-Ray Spectroscopy (EDS). This analysis confirmed the integration of the polymer between the grain boundaries of ZnO grains. From the TEM image shown in Figure 4-4, the grain boundary thickness can be estimated to be approximatively 3 nm. However, and to be expected, segregation of polymer in pores also occurs at the larger volume fraction of 10 vol.%. Such effects have been reported in earlier studies.[1, 89]

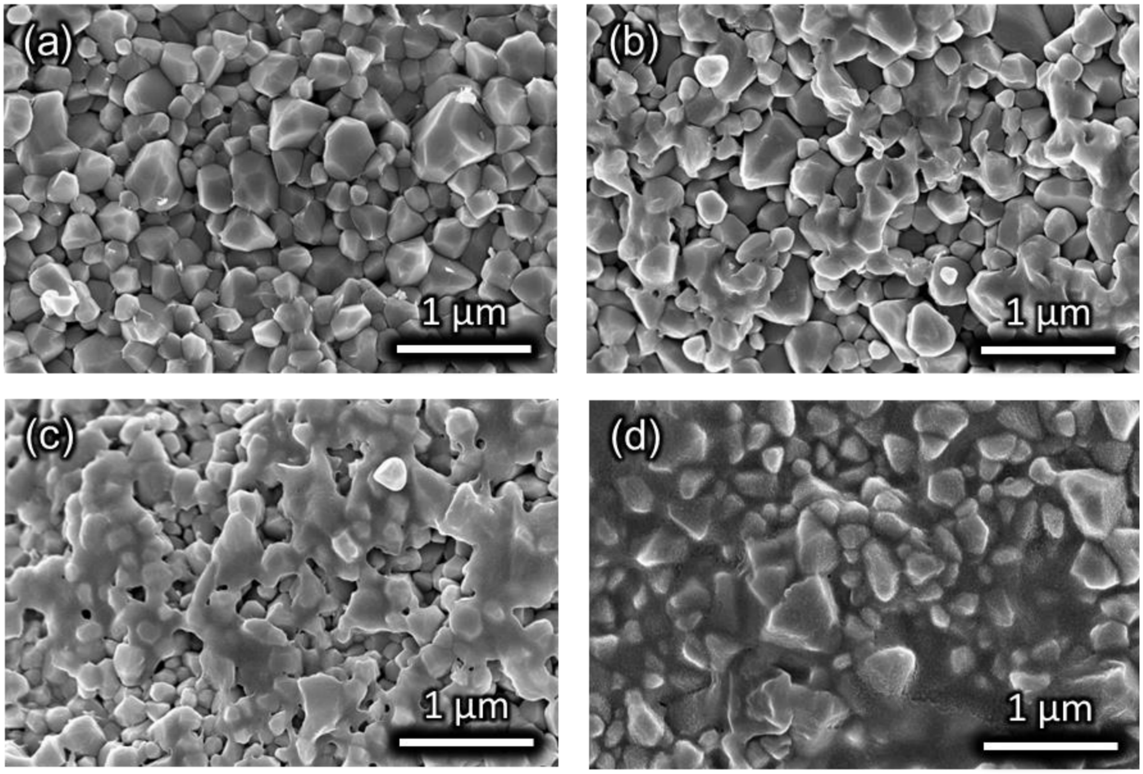

Figure **4-3**: Microstructure of ZnO/PVDF-TrFE composite with filler volume fractions of (a) zero vol. %, (b) 2 vol.%, (c) 6 vol.% and (d) 10 vol.%.

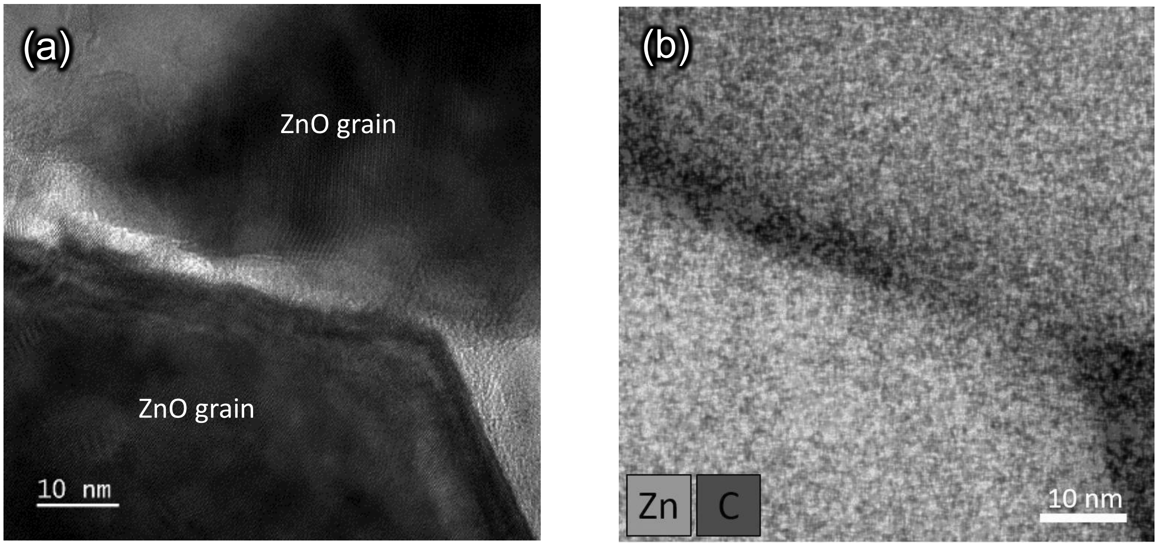

Figure **4-4**: (a) TEM image of PVDF-TrFE ferroelectric polymer (10 vol.%) located at the interface between ZnO grains. (b) EDS mapping image showing in red the preferential presence of carbon between the grains, confirming location of PVDF-TrFE. Note the larger segregated polymer region in the nanometric void where grains converge towards a tripe point.

The cold sintered composite with 10 vol.% of PVDF-TrFE was analyzed at room temperature by Fourier Transform Infrared (FTIR) spectroscopy. For the 700-1500 cm^{-1} range, the peaks of the PVDF-TrFE α-phase spectrum correspond to 759, 981 and 1222 cm^{-1} wavenumber values, while for the β-phase the corresponding values would be 845, 1076 and 1289 cm^{-1}. The corresponding vibrational assignments to these peaks are indicated in Table 4-S1. [98, 99] The analysis in Figure 4-5 indeed reveals the presence of the ferroelectric phase of the PVDF-TrFE, known as β. The presence of this β-phase is necessary for the PVDF-TrFE to be ferroelectric. However, with the polymer being confined to constrained volumes at the grain boundaries, restrained mobility of the polymer chains may be expected for this phase, leading to a shift of the Curie Temperature of phase transition.[92]

Zhao et al. demonstrated that thermal activation energies for the electrical conduction at the grain boundaries of a ZnO-PTFE composite do not significantly vary for polymer content above 0.5 vol.%. This phenomenon is attributed to the fact that the matrix ZnO has to densify and there can only be a limited amount of polymer confinement; otherwise this would limit the cold sintering densification. Earlier, Tsutsumi et al. reported the depression of crystallinity and repression of molecular mobility of confined PVDF-TrFE thin films for thickness under 100 nm.[92] However with thermal annealing at 150°C the crystallinity and the ferroelectric properties improved at 20 nm thicknesses. Despite the nanometer scales observed here, it appears that with the cold sintering temperatures the ferroelectric properties are stable. In the following section, the dielectric measurements of the cold sintered composites support that there were no limitations to the formation of the β-phase, as no shift of the Curie point was observed.

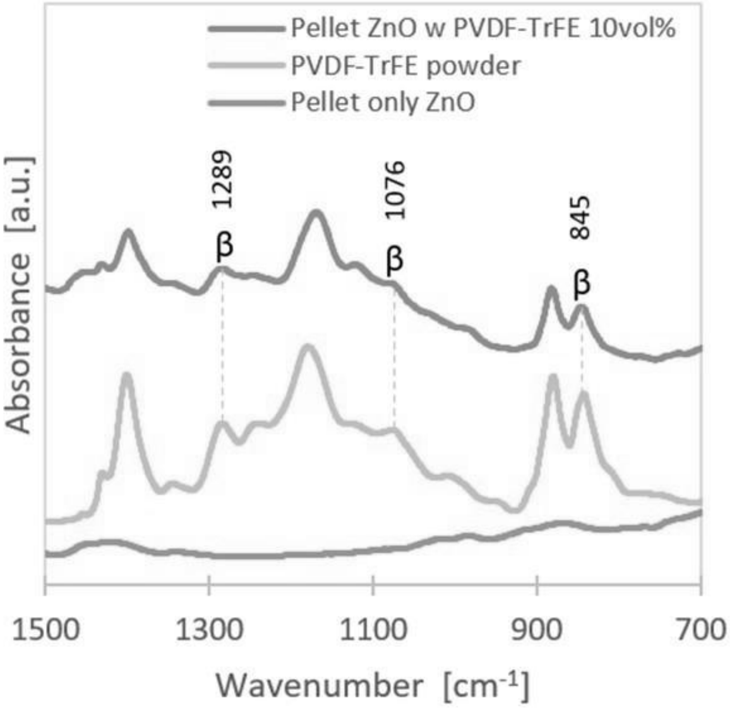

Figure **4-5**: FTIR spectrum of ZnO/PVDF-TrFE 10 vol.% cold sintered composite, PVDF-TrFE powder and a cold sintered pellet with only ZnO.

4.3.2.1 Dielectric characterization

Characterization of electrical properties was conducted on ZnO samples with zero, 2, 6 and 10 vol.% of PVDF-TrFE. These samples exhibited a peak of relative permittivity values at the ferroelectric-paraelectric $T_C \sim 124°C$, consistent with the ferroelectric properties of the polymer after CSP. This characteristic peak of the relative permittivity, along with suppression of dielectric loss are shown in Figure 4-6 for measurements at 1 MHz of sample containing 10 vol.% of PVDF-TrFE.

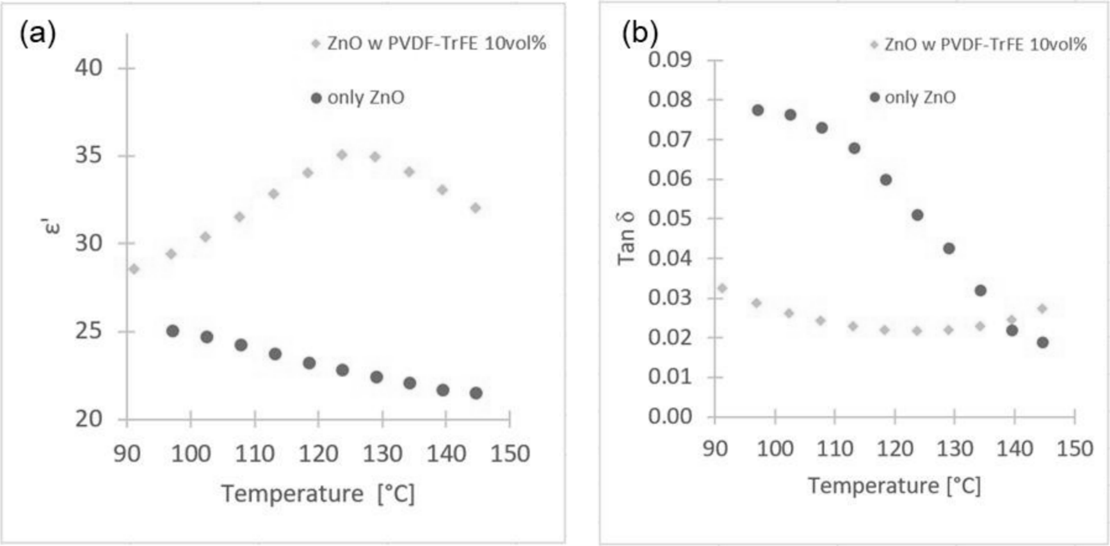

Figure **4-6**: (a) Relative permittivity and (b) *Tan δ* values for ZnO/PVDF-TrFE composites as a function of temperature on heating measured at 1 MHz.

Considering the dielectric data as a function of frequency and temperature, the dielectric response has a strong relaxation behavior that is consistent with space charge polarization. The space charge is the result of the semiconducting ZnO grains and the insulating polymer acting as barriers at each grain boundary. Thermal Activation Energies (E_A) were determined from dielectric relaxations (ε_r'') measured as a function of frequency (from 1 kHz to 1 MHz), from the Arrhenius equation 4.1:

$$\omega_r = \omega_0\, exp\left(\frac{-E_A}{k_B T}\right) \qquad \text{(Eq. 4.1)}$$

Figure 4-7 shows that the calculated activation energies did not vary significantly ($E_A \sim$ 0.4 eV) among the samples with 2 vol.%, 6 vol.% and 10 vol.% of filler (standard least squares error of the estimates = 0.23, 0.20 and 0.34 1/s, respectively).

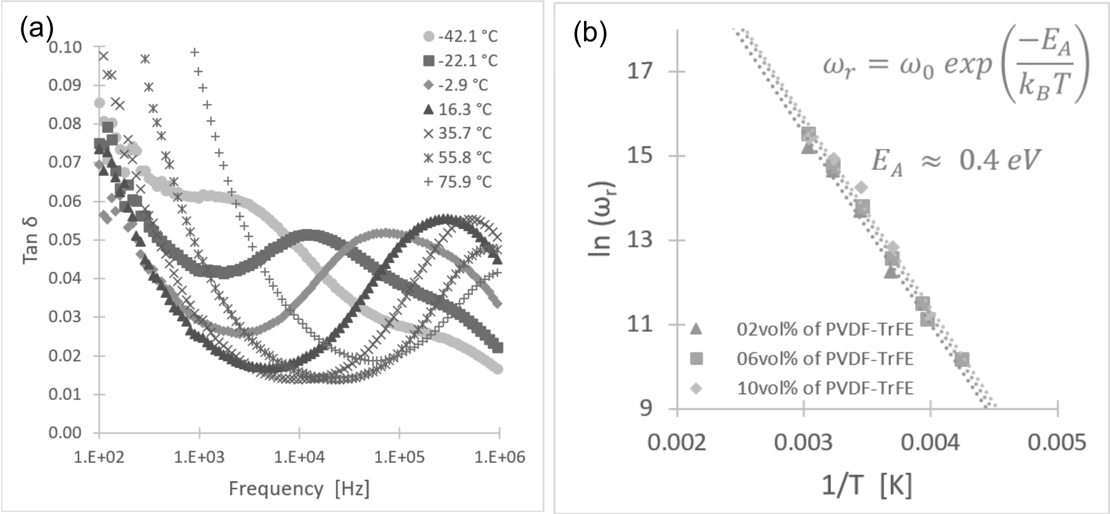

Figure **4-7**: (a) Dielectric relaxations (ε_r'') of ZnO/PVDF-TrFE 10 vol.% composite, and (b) corresponding Arrhenius plot illustrating determination of thermal activation energies for 2, 6 and 10 vol%.

The Maxwell-Wagner-Sillars (MWS) effect is a mechanism that describes interfacial space charge contributions to dielectric loss as a function of frequency, due to the charge buildup at the electrode/sample interface. Thereby the segregated polymer in pores has less impact on the overall dielectric properties than the serial distribution of the intergranular PVDF-TrFE. Therefore, we can approximate the relaxation frequency with the MWS model. The peak frequency f_{MWS} describes the polarization present at internal boundary layers within an inhomogeneous sample[72, 100] and is given by Equation 4.2:

$$f_{MWS} = \frac{\sigma_{sam}}{2\pi\varepsilon_0(\varepsilon'_{sam} + (l_{sam}/l_{ins})\varepsilon'_{ins})} \qquad \text{(Eq. 4.2)}$$

where ε'_{sam}, ε'_{ins}, l_{sam} and l_{ins} correspond to the real permittivities, grain size and insulating intergranular polymer grain boundary layers, respectively. Taking for example the case of the ZnO/PVDF-TrFE (10 vol.%) composite, the relaxation frequency $f_{MWS} \sim 2.48 \times 10^5\ Hz$ (illustrated in Figure 4-7.a) at room temperature, is used as verification method for the average grain boundary layer thickness throughout the bulk sample. The following values were considered for the calculation of the average PVDF-TrFE thickness: $\varepsilon'_{sam} = \varepsilon'_{ZnO} = 25$ (from experimental data of this work at room temperature), $\varepsilon'_{ins} = \varepsilon'_{PVDF-TrFE} = 11$ (from technical data sheet of 75/25 PVDF-TrFE PolyK Technologies), $\sigma_{sam} = \sigma_{ZnO} = 9.68 \times 10^{-3}\ \Omega^{-1}m^{-1}$ at room temperature[101], $\varepsilon_0 = 8.854\ \times 10^{-12}\ s\Omega^{-1}m^{-1}$ and $l_{sam} \sim 300\ nm$ (ZnO grain size in this work). A computed value from Eq. 4.2 gives an average grain boundary thickness $l_{ins} \sim 4.9\ nm$. This value is consistent with the TEM observation, as grain boundary thicknesses of $\delta_{PVDF\text{-}TrFE}$ is approximatively 3 nm as illustrated in Figure 4-4.a.

4.3.2.2 Current-voltage (I-V) analysis

The PVDF-TrFE based barriers are expected to give non-linear conduction processes across the composite. Electrical characterization revealed an enhancement on the non-ohmic response with the addition of the ferroelectric polymer (Fig. 4-S4). The α values from the I-V analysis in Figure 4-8 were 1.3 and 3.5 at 120°C for the pellets containing zero and 2 vol.% of PVDF-TrFE, only increasing marginally to ~4.0 with 10 vol.% of the polymer. Therefore, a more detailed analysis of the composite with 2 vol.% PVDF-TrFE was provided.

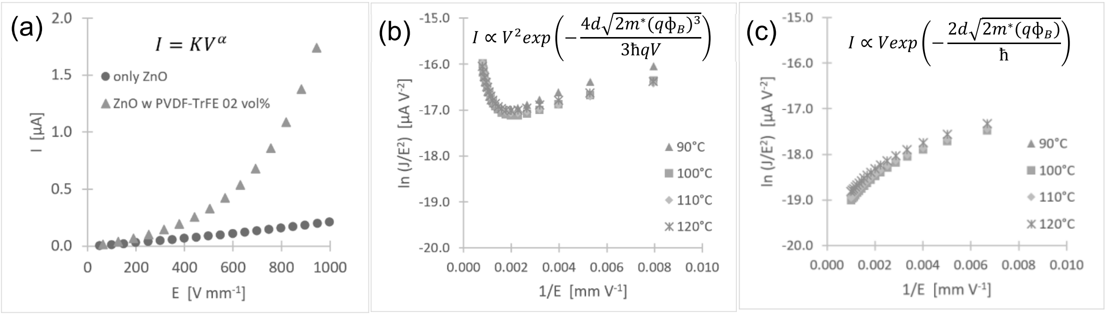

Figure **4-8**: (a) Current as a function of applied electric field shows an enhance in the non-ohmic response of composite sample, contrasting with the near to linear α coefficient value for the pure ZnO polycrystalline pellet. (b) Current density as a function of reciprocal applied electric field shows an increase at higher voltage values presenting a Fowler-Nordheim characteristic, here shown for the ZnO/PVDF-TrFE composite with 2 vol% filler. (c) Response from pure ZnO polycrystalline sample, presenting a direct tunneling behavior.[102, 103]

Considering the calculated activation energies for the dielectric relaxation of the ZnO/PVDF-TrFE reported in Figure 4-7.b and noting these did not significantly vary for the different amounts of polymer amount in the composite, to a first order approximation, bulk PVDF-TrFE properties were used to consider more details of the composite, as applied below, into the parameterization of the dielectric media at the interfaces.

To determine the electronic conduction mechanism across the grain boundaries of the composite material, the applied electric field should be calculated per grain boundary length E_{GB} according to Equation 4.7:

$$E_{GB} = E\frac{d}{\delta} \qquad \text{(Eq. 4.7)}$$

where E is the applied electric field, d is the average grain size and δ is the depletion layer or grain boundary thickness. For this analyzed system, $d \sim 293$ nm and $\delta \sim 3$ nm.

4.3.2.2.1 Low voltage analysis

At low applied voltage, the electronic conduction mechanism could be Schottky thermionic emission (S-E), Poole-Frenkel emission (P-F) or a combination of both mechanisms. To determine which mechanism is dominating the electronic conduction in the system, the natural logarithm of current density (J) over temperature squared (T^2), and the natural logarithm of current density (J) over applied electric field (E_{GB}), must be plotted as function of square root of the applied electric field ($E_{GB}^{0.5}$). The calculated slope values are then used to determine each β value by Equation 4.8:

$$slope = \frac{\beta}{k_B T} \qquad \text{(Eq. 4.8)}$$

where k_B is Boltzmann's constant. The η value is 4 for a Schottky thermionic emission ($\eta_{S\text{-}E} = 4$) and 1 for Poole-Frenkel emission ($\eta_{P\text{-}F} = 1$)[77, 104, 105], and it is calculated by Equation 4.9:

$$\eta = \frac{q^3}{\beta^2 \pi \varepsilon_0 \varepsilon_\infty} \qquad \text{(Eq. 4.9)}$$

where q is the fundamental electric charge and ε_∞ is the dynamic permittivity ($\equiv n^2$).

The plots illustrated in Figure 4-9 show the slope of linear response at low voltages used to determine $\eta_{S\text{-}E}$ and $\eta_{P\text{-}F}$. To calculate η using Eq. 4.9, the considered value of the dynamic permittivity was the refractive index squared of the ferroelectric polymer in the 0.5 – 2.5 THz frequency range, $\varepsilon_\infty \rightarrow \varepsilon_{r\ \mathrm{PVDF\text{-}TrFE(0.5\text{-}2.5\ THz)}} = 3$.[106] The electron transport across an insulating polymer media would be expected to have a slower mobility, and therefore the refractive index would be more appropriately taken from the THz frequency range than the optical.[106]

The computed $\eta_{S\text{-}E}$ values were between 4.9 and 10.2 for a temperature range from 120 °C to 85 °C; and between 36.9 and 504.5 for $\eta_{P\text{-}F}$ within the same temperature range. Both S-E and P-F conduction mechanisms are well known field-assisted thermally stimulated processes. With temperature rise, the electron's energy increases to cross the insulating grain boundary by Schottky thermionic emission due to the applied field; similarly, in the Poole-Frenkel mechanism the temperature rise facilitates the thermal detrapping of an electron from the bulk material into the conduction band.[104] Consequently, as the temperature increases, the $\eta_{S\text{-}E}$ and $\eta_{P\text{-}F}$ values approach 4 and 1 respectively. Therefore, these results indicate the Schottky thermionic emission to be the dominating conduction mechanism over Poole-Frenkel, between grain boundaries at low voltages. From Eq. 4.4 at $E_{GB} = 0$, the Schottky barrier height was calculated to be $q\varphi_B = 1.1$ eV for the ZnO with 2 vol% of PVDF-TrFE composite.

Table **4-1**: Calculated η values in the 85 – 120°C temperature range.

Temperature	η_{S-E}	Standard least squares error of the estimate [A mm^{-2} K^{-2}]	η_{P-F}	Standard least squares error of the estimate [A mm^{-1} V^{-1}]
85°C	10.2	± 0.016	504.5	± 0.026
90°C	7.3	± 0.025	157.8	± 0.036
100°C	5.3	± 0.034	69.7	± 0.043
110°C	4.7	± 0.023	43.5	± 0.038
120°C	4.9	± 0.015	36.9	± 0.016

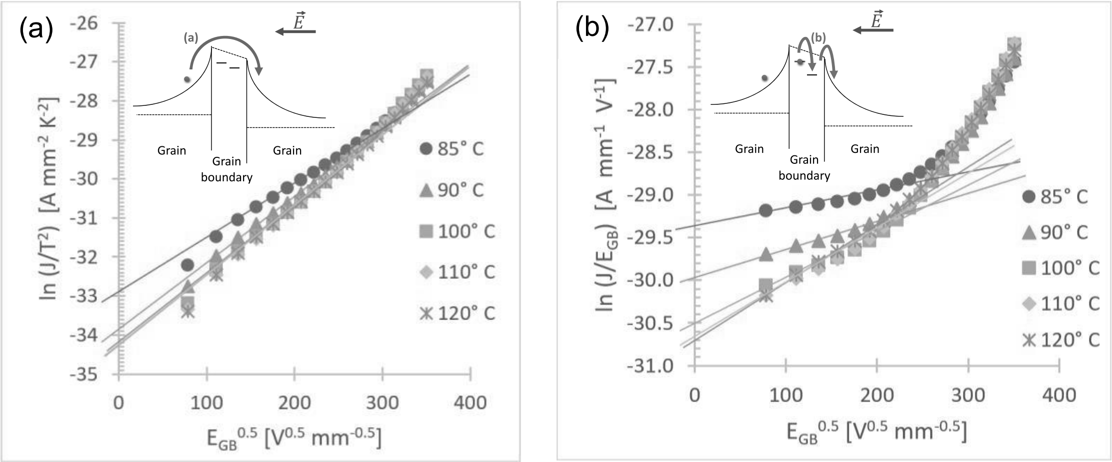

Figure **4-9**: (a) Schottky emission plot and (b) Poole-Frenkel plot, from ZnO/PVDF-TrFE (2 vol% filler) composite (diagrams of Schottky emission and Poole-Frenkel mechanisms based on model of Mahan et al. [75, 77]

The current-voltage-temperature data in Figure 4-9 describe the low field behavior with the Schottky-emission conduction across the grain boundaries as η closely matches the expected values of 4, relative to the values of Poole-Frenkel where η=1, and the experimental data under this analysis was far off those values, thereby leading to the conclusion that the non-linear conduction is best described by the Schottky-Emission mechanism.

4.3.2.2.2 High voltage analysis

The nature of the conduction changes at higher fields, and the cross over can be readily seen in the form of a Fowler-Nordheim plot for these composites. The Fowler-Nordheim plot in Figure 4-10 shows the fitting linear response at high applied voltages, which correlates to values of $\gamma = 0.166$ V nm^{-1} = 0.166×10^9 J C^{-1} m^{-1} (standard error of the estimate = 0.081 A V^{-2}), with A = 4×10^{-17} from Eq. 4.5. Studies of the density functional theory (DFT) within the local density approximation (LDA) of the effective electron mass in ZnO (wurtzite structure), indicate that $m^*_{ZnO} = 0.23\ m_0$,[107] being $m_0 = 8.187 \times 10^{-14}$ J c^{-2}. Using Eq. 4.6, the calculated barrier height of the Fowler-Nordheim tunneling is $q\varphi_B = 0.1$ eV at high fields.

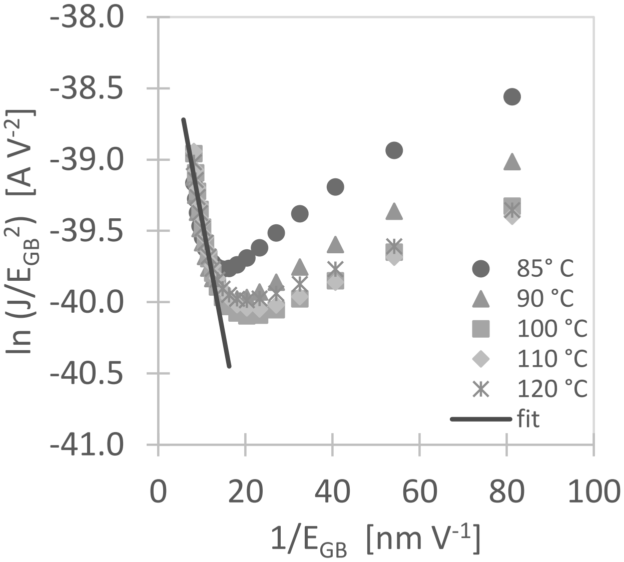

Figure **4-10**: Fowler-Nordheim plot from ZnO/PVDF-TrFE (2vol% filler) composite.[75, 77]

4.3.2.3 Barrier height field dependence

Jinliang He [108] established that, in a general form, the field dependence of the barrier height at the grain boundaries for ZnO varistors can be expressed by Equation 4.10:

$$q\varphi_B = \frac{E_c}{4}\left(1 - \frac{E_{GB}}{E_c}\right)^2, E_{GB} \leq E_c \qquad \text{(Eq. 4.10)}$$

where E_{GB} is the applied electric field at the grain boundary and E_c is a critical voltage at which the barrier height vanishes as illustrated in Figure 4-11. Here this dependence is considered under the Fowler-Nordheim tunneling conduction described by Eq 4.11 and also the Schottky Emission conduction described by Eq. 4.12:

$$q\varphi_B^{F-N} = \frac{E_c^{F-N}}{4}\left(1 - \frac{E_{GB}}{E_c^{F-N}}\right)^2, E_{GB} \leq E_c^{F-N} \qquad \text{(Eq. 4.11)}$$

$$q\varphi_B^{S-E} = \frac{E_c^{S-E}}{4}\left(1 - \frac{E_{GB}}{E_c^{S-E}}\right)^2, E_{GB} \leq E_c^{S-E} \qquad \text{(Eq. 4.12)}$$

where E_c^{F-N}~0.6 V/nm and E_c^{S-E}~ 4.5 V/nm. This coincides with the smaller barrier height obtained at high applied voltages (0.1 eV for Fowler-Nordheim conduction), compared to the larger barrier height at low applied voltages (1.1 eV for Schottky emission). The transition regime was also considered, averaging E_c^{trans} ~ 2.6 V/nm and a with a barrier height corresponding calculated value $q\varphi_B^{trans}$ ~ 0.6 eV.

By considering the results obtained in these analyses of the electrical characterization of ZnO/PVDF-TrFE composite, it is noticeable that the presence of the ferroelectric polymer integrated at the grain boundaries enables the Fowler-Nordheim tunneling conduction mechanism in contrast with the direct tunneling characteristic of the only ZnO sample, as shown in Figures 4-8.b,c. Additionally, it was observed that the barrier height at the grain boundaries decreases at higher applied electric fields as described by He[108] and Blatter and Greuter[109], as illustrated in Figure 4-11. These features are valuable to assess for new application opportunities of electroceramics in varistors, energy harvesting and actuators on flexible substrates.

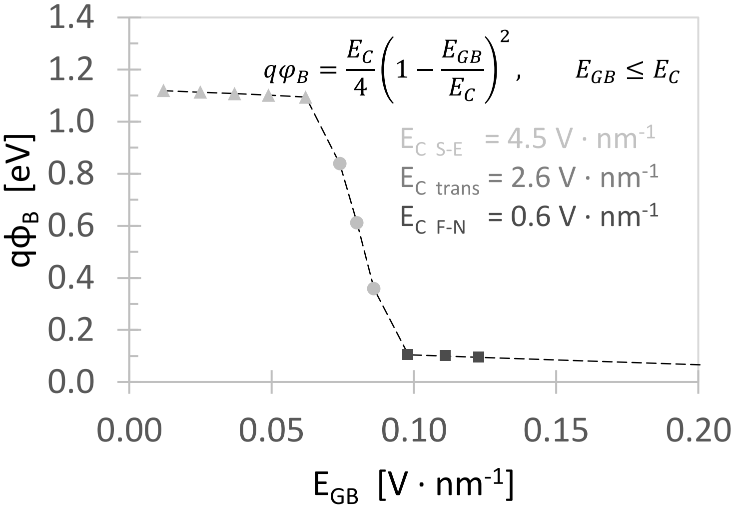

Figure **4-11**: Barrier height as a function of applied electric field at the grain boundaries, shows a decreasing behavior in correlation with Eq. 4.10 and its corresponding schematic from Blatter and Greuter. [109]

4.4 Conclusions

The cold sintering process enabled the fabrication of ZnO/PVDF-TrFE ceramic-polymer composite samples to relative densities >95 % for volume fractions of 2, 6 and 10 vol.% at temperatures as low as 140°C. Through a TEM analysis, the thickness of the PVDF-TrFE was measured to be ~ 3 nm at grain boundaries. The ferroelectric properties of PVDF-TrFE were preserved after the cold sintering process within these confined regimes, this being demonstrated by the presence of the polymer's β phase peaks in FTIR spectroscopy and by the anomaly of the composite dielectric permittivity maxima at T_C ~ 124°C. From the frequency dependence at different temperatures the dielectric relaxation could be correlated via the Maxwell-Wagner-Sillars (MWS) effect using the f_{MWS} relaxation frequency, identified in dielectric measurements of imaginary permittivity. This provides a calculated barrier thickness with all the expected physical properties of the ZnO and the PVDF-TrFE in good agreement with TEM observations. To better understand the nature of the conduction across these grain boundaries, a more comprehensive current-voltage (I-V) analysis performed on ZnO-PVDF-TrFE composites revealed a non-ohmic behavior, indicating that at low voltages applied, the conduction mechanism present across grain boundaries was Schottky thermionic emission with a barrier height of 1.1 eV. At higher voltages the conduction transitioned to a Fowler-Nordheim tunneling with effective reduction of the barrier to 0.1 eV. The field dependence of the barrier height is also tested with a phenomenological model. This study points to the ability to introduce functional polymers into the grain boundaries of ceramics, and correlate physical trends in the properties.

4.5 Supplemental figures and tables to Chapter 4

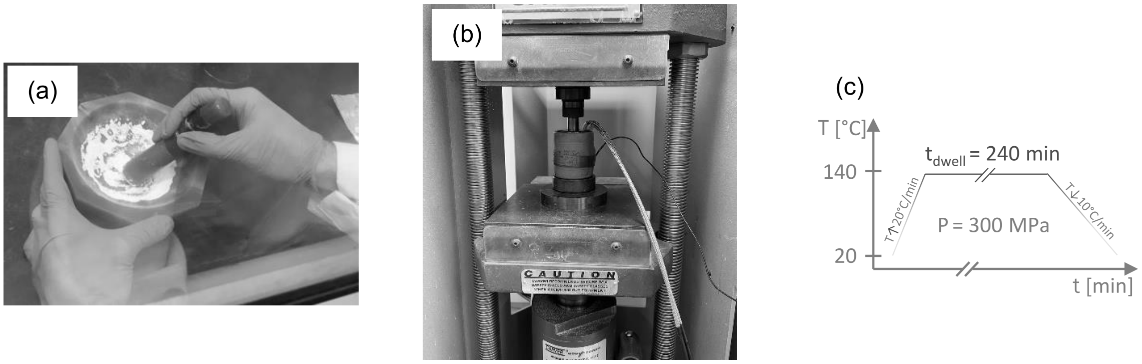

Figure **4-S1**: (a) Mixing by hand of ZnO, PVDF-TrFE and acetic acid. (b) CSP setup and (c) thermal profile for fabrication of pellet samples.

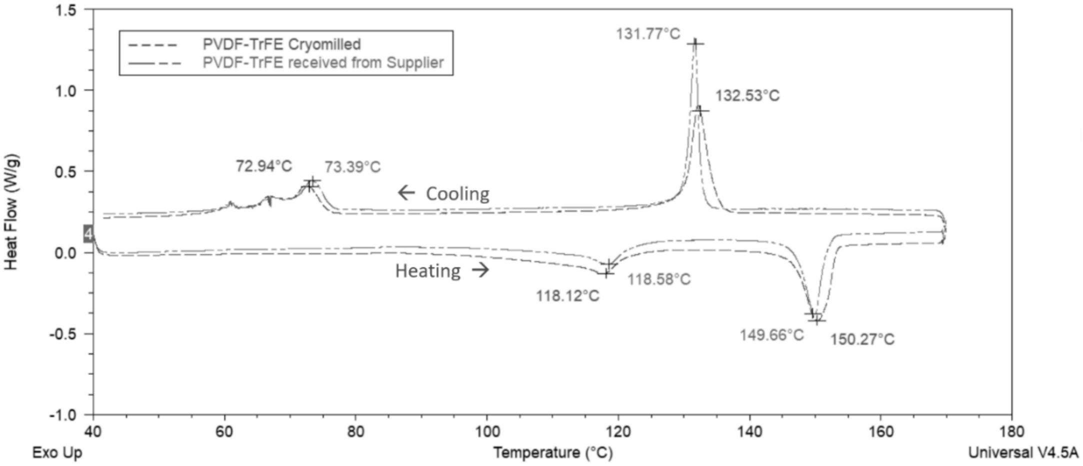

Figure **4-S2**: DSC profiles of PVDF-TrFE copolymer in the initial condition and in the cryomilled condition.

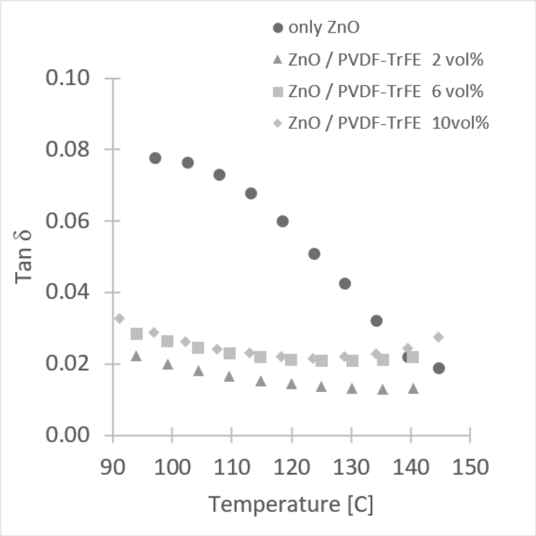

Figure **4-S3**: Suppression of dielectric loss at 1 MHz, observed for the composite with different volume fractions of PVDF-TrFE, relative to the sample containing only ZnO.

Table **4-S1**: Vibrational assignment of β phase [98] identified in FTIR spectrum of PVDF-TrFE.

Wave-numbers [cm^{-1}]	Vibrational assignment
845	CF_2 symmetry stretch
1076	CH_2 wag, CC stretch
1289	CH_2 scissor, CC stretch, CF_2 symmetry stretch

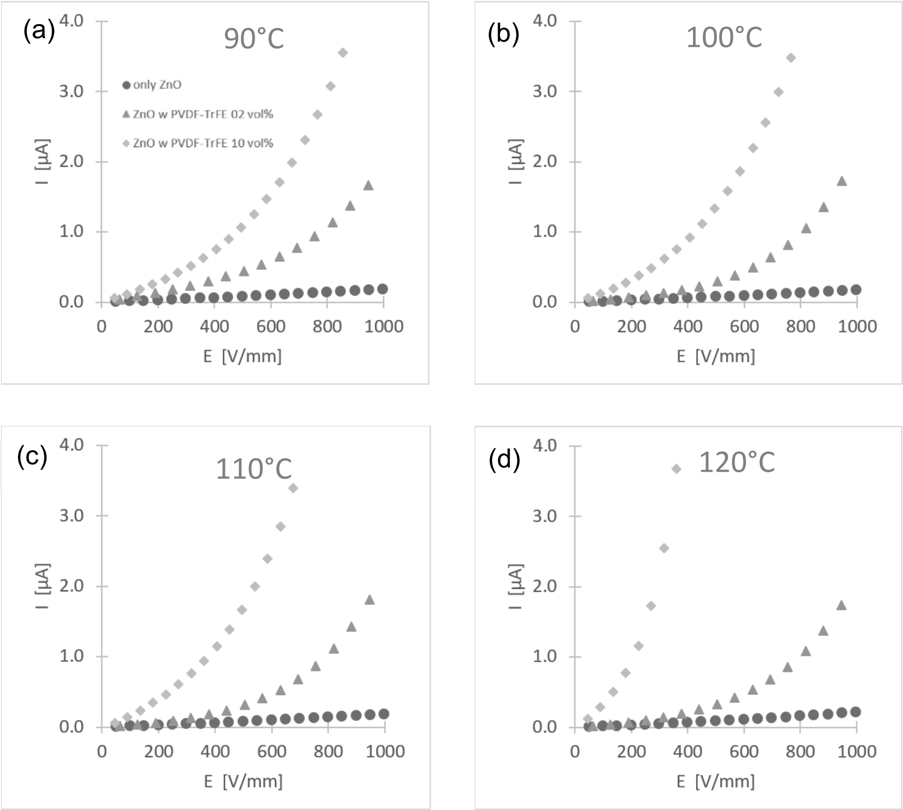

Figure **4-S4**: Non-ohmic response of current-voltage analysis of ZnO samples with zero, 2 and 10 vol.% of PVDF-TrFE at (a) 90°C, (b) 100°C, (c) 110°C and (d) 120°C.

Chapter 5

Sodium Molybdate-Hexagonal Boron Nitride Composites Enabled by Cold Sintering for Microwave Dielectric Substrates

In order to fulfill the demands for more bandwidth in 5G and 6G communication technologies, there's a crucial need for innovative dielectric substrates that can be co-fired into devices, offering low dielectric loss (*tan* δ) and heightened thermal conductivity (κ). The motivation for this study lies in designing composites adept at minimizing dielectric loss and boosting thermal conductivity, while also restricting electrical conductivity, for microwave applications involving high-power and high-frequency. The research encompasses the fabrication of dense ceramic matrix composites (CMC), employing Sodium Molybdate $Na_2Mo_2O_7$ (NMO) as the model dielectric material for cold sintering, along with hexagonal boron nitride (hBN) as filler to enhance the thermal conductivity. Physical properties of these composites were thoroughly analyzed as a function of filler volume fraction, temperature and frequency. Furthermore, this investigation extends the understanding of dielectric, electrical, and thermal properties, particularly focusing on the relative permittivity (ε_r), dielectric loss (*tan* δ), electrical resistivity (ρ), breakdown strength (E_b) analyzed through Weibull statistics, and the anisotropic thermal conductivity (κ) influenced by filler crystal structure. Through systematic characterization under varying conditions, this analysis underscores the potential of engineered ceramic matrix composites as a viable alternative for microwave substrate materials, as demonstrated through cold sintering.

5.1 Introduction

Traditional ceramic packaging materials used in high power and high frequency electronic applications are approaching the end of their usability as devices continue to push to higher frequencies and power densities, resulting in increased heating.[110] In spite of extensive efforts in materials innovation and discovery, the pace of innovation in packaging materials selection and processing has been outpaced by device design and power density scaling.[111] In the case of dielectric substrates, there is co-design required for material properties including low temperature dependence, low dielectric loss (*tan δ*) and high thermal conductivity (κ). As operational frequencies increase to provide more bandwidth in 5G and 6G communication or finer resolution and longer range in radar systems, there is a compounding problem where the increased dielectric loss in the material, combined with the demand for higher total power densities to provide usable range at these frequencies, will result in significant power dissipation leading to localized heating of nearby materials. As a result, materials that have both excellent thermal conductivity and dielectric performance are urgently needed, as their impact would be felt in a range of application areas from electronic packaging in data farms, to power electronics and various 5G and 6G infrastructures. Typically, low temperature cofired ceramics have dielectric properties of relative permittivity (ε_r) in the range of 4 – 12, dielectric loss in the range of 0.0007 – 0.006 at 1 MHz , and thermal conductivity in the range of 2.0 – 4.5 W m^{-1} K^{-1}. [112]

Cold sintering is a low temperature densification process that has been introduced and demonstrated across a wide array of material systems and devices. In cold sintering, the densification usually occurs at temperature below 300 °C, and under applied pressures of a few hundred MPa in the presence of a transient chemistry that enables the process. The overall chemo-mechanical process is described by a pressure solution mechanism, which determines the dissolution, transport and precipitation collectively sintering the particles. Details of the mechanism can be found in a number of early works. [26, 30, 83, 87, 113–115] One of the major attractions of the cold sintering process is its ability to provide a densification of bulk and thick film materials in new composites that previously could not be realized. Under conventional processes, high temperatures would lead to decomposition and deleterious reactions between various phases that would limit the driving force for densification and also create unwanted interfaces limiting the composite design.

With cold sintering, the low temperatures and fast kinetics circumvent these problems, and allow densification to take place with mixing of many new types of material systems. Provided there is one phase that is the major volume fraction in the composite (the matrix) that can undergo sintering, other phases (the filler) can be integrated into the body and from a composite. [38, 41, 116–119]

A range of works have demonstrated that novel phases and materials, such as polymers (thermoplastics and thermosets) [1–6], 2-D materials [7, 8], and buckminsterfullerene [9] can all be readily incorporated into the grain boundaries of a sintered ceramic material. Previously, a number of examples have been made in the cold sintering of low loss dielectrics with other fillers. [10, 11, 20, 21, 12–19] To this point, there have been no attempts to consider composites that maintain high frequency dielectric properties and high electrical resistivity, while simultaneously enhancing thermal properties.

In many cases, can dramatically reduce the overall thermal performance of a material, presenting as large thermal resistances to phonon and/or electron-dominated thermal transport in homogeneous materials. [120, 121] However, cold sintering offers the opportunity to design the grain boundaries to utilize this interconnected network as a path for phonon transport around other materials in the composite.

The objective of this study is to produce high thermal conductivity through the incorporation of high-κ hexagonal boron nitride (hBN) on grain boundaries, while also optimizing the dielectric properties for minimal loss. Prior efforts to utilize boron nitride nanosheets, graphene and diamond nanoparticles have yielded a large variation of observed effective thermal conductivity [122] and often required a significant volume fraction of the high-κ filler (50% or more). Accomplishing this in practice can be challenging, since although the filler material has a large κ, the interfacial thermal resistance between adjacent filler elements and the effective area of the intergranular thermal network will serve to limit the achievable effective κ in the composite. Cold sintering can serve to enable improvements in both of these areas, promoting intimate contact between adjacent filler material through confinement of the grain boundary network, as well as a reduction in the required volume fraction of filler needed to reach the percolation threshold where the thermal network can have an observable impact. A challenge to overcome in using hBN, which has an extremely large band gap, is to ensure that these inclusions will not be deleterious to the dielectric losses. As a final benefit to the cold sintering process, the ability to manufacture multilayers with printed electrodes that can all be integrated on metal substrates in a single cold sintering step offers further viability to cold sintering as a key fabrication process in high frequency and high power applications moving forward.[123]

The general goals to be achieved in this investigation are: the fabrication of high density electroceramic composites via cold sintering, using a sodium molybdate $Na_2Mo_2O_7$ (NMO) ceramic matrix and hBN as a filler with high thermal conductivity; the characterization of physical properties of the composites as a function of filler volume fraction, temperature and frequency; and the fitting and modeling of the measured properties according to the microstructural design enabled by cold sintering.[45]

5.2 Experimental procedure

5.2.1 Powder preparation

Stoichiometric amounts of Na_2CO_3 (15.1 g of 99.95%, Alfa Aesar) and MoO_3 (41.1 g of 99.5%, Alfa Aesar) were mixed in a PTFE 1L container, using 8 mm zirconia milling media and 300 ml of ethanol in a ball mill for 24 hours. The volume of the container was distributed to be approximately 1/3 zirconia milling media, 1/3 air and 1/3 ethanol plus powder. The resulting slurry was dried for 6 hours in a 120°C oven. This powder was subsequently calcined at 500°C for 5 hours, following the reaction:

$$Na_2CO_3 + 2MoO_3 \rightarrow Na_2Mo_2O_7 + CO_2$$

The calcinated condition of the sodium molybdate $Na_2Mo_2O_7$ (NMO) [90, 124] powder and its corresponding XRD pattern are documented in Figure 5-S1. A subsequent ball milling was performed in dry condition on the calcined powder for 30 minutes to break the agglomerates of NMO grains to isolated particles. Figure 5-S2 shows the obtained NMO powder with unimodal particle size distribution and a mean size of 2.4 ± 0.9 µm. The pure NMO powder was mixed with 0.5 - 50 vol.% of hBN (99.8%, 70-80 nm, Nanoshel) for the cold sintering of composites.

5.2.2 Cold sintering process

For the fabrication of each pellet, the NMO matrix powder and hBN filler powders were weighed for each sample according to the intended filler volume fraction. The weighed powders were put together in a glass vial and mixed using a planetary centrifugal mixer (Thinky, AR-250) for 10 cycles of 1 minute each. After centrifugal mixing, 25 wt.% of deionized water was added to the homogeneously mixed powder using a pipet, and the powder and the transient chemistry, H_2O, were manually mixed in an agate mortar with a pestle for ~10 minutes until a homogeneous appearance was obtained. The moistened powder was then placed in a stainless steel die for cold sintering. Pellets for characterization of their dielectric properties in the 75 – 110 GHz frequency range, were fabricated using a die to make samples of 25 mm diameter and 4 mm thickness; for 9 – 13 GHz the dimensions of the pellets were 13 mm diameter and 6 mm thickness, while for 10^5 and 10^6 frequency measurements the samples' dimensions were 13 mm in diameter and 2 mm in thickness. The pellets intended for measurements of electrical resistivity, electrical breakdown strength and anisotropic thermal conductivity analysis, were fabricated in a die for samples of 13 mm in diameter, with thicknesses of 2 mm, 1 mm and 13 mm, respectively. A uniaxial pressure of 250 MPa was applied using a press (Carver, model CH4386) at room temperature, and then heated at a heating rate of ~15°C/min up to 180°C for 2 hours using a heating jacket wrapped around the die controlled by a PID loop feedback mechanism. The thermocouple was positioned in the lower piston of the die. After the dwell time, the pellet was ejected from the die and it was left to cool down to room temperature under ambient conditions. Finally, the cold sintered pellets were dried out in air at 200°C for 12 hours. This optimized overall cold sintering procedure yielded relative densities >96% for NMO pellets and NMO-hBN composite samples with volume fractions of 0.5 - 50 vol.%.[45] Finally, the surfaces and edges of all samples were manually polished using a 1200 grit silicon carbide sandpaper using ethanol as a lubricant. The thickness of pellets fabricated for electrical breakdown testing was reduced by manual polishing from 1mm to ~0.4 mm. Figure 5-S3 summarizes the processing steps for the synthesis of NMO powder and the cold sintering of the NMO-hBN composite pellets.

As previously described in Figure 4-1, the dissolution, transport and precipitation steps of the cold sintering process involve the presence of transitory chemical products to achieve the densification of the polycrystalline ceramic. For the cold sintering of Sodium Molybdate using water as the transient liquid phase, it must be considered that NMO has high solubility in H_2O (of 3 g/L at room temperature, atmospheric pressure and neutral pH)[125]. The mass transport/precipitation following dissolution under stress, can be described as the interdiffusion at an interfacial aqueous phase with high concentration of Sodium Hydroxide (NaOH) and Molybdic Acid $(MoO_3)(H_2O)_3$ complexes, that transitions into a gel and then a glassy phase with the systematic dehydration process.[124]

5.2.3 Dilatometry study

A dilatometry study was conducted to measure the relative densification of powders under cold sintering and monitored as a function of time. This was performed using an Enerpac system hydraulic press with attached digital contact sensor Keyence GT2-H32. A uniaxial pressure of 250 MPa was applied at $t_0 = 0$, and the linear displacement of the sample was measured with a resolution of 0.5 µm every 1 second interval. The height shrinkage of the pellet sample was defined by

$$\frac{\Delta h_t}{h_0} = \frac{(\Delta d_t - \Delta d_0)}{\Delta d_0} \qquad \text{(Eq. 5.1)}$$

where $\Delta h_t \ / \ h_0$ is the height shrinkage of the pellet at a given time t, Δd_t is the displacement difference between the sample and a calibration at a given time t and Δd_0 is the initial displacement difference at t_0.[84] A description of the dilatometry setup and study used on the cold sintered samples is documented in Figure 5-S4.

5.2.4 Characterization

The synthesized NMO powder was analyzed by X-ray diffraction (XRD) via a PANalytical Empyrean system operated at 45 kV and 40 mA with Cu Kα radiation. The powder particle size was measured using Field Emission Scanning Electron Microscope (SEM, Thermo Fisher FESEM Verios G4) images at 10,000X magnification. Relative densities were obtained by dividing the measured geometrical density of the pellets by their theoretical density ($\rho_{NMO} = 3.682$ g/cm^3, $\rho_{hBN} = 2.1$ g/cm^3).

For dielectric characterization, the pellets were polished with 1200/P4000 sandpaper and ethanol. Platinum electrodes of 200 nm thickness were Sputter Coated (Quorum Q150R). Dielectric measurements (ε_r, $\tan\delta$) at low frequencies of 10^5 and 10^6 Hz were performed on pellets with diameter of 13 mm and thickness of 2 mm, using a precision LCR meter (Keysight E4980A) at 10^5 and 10^6 Hz. Dielectric measurements at high frequencies (ε_r, $\tan\delta$, f_{res}, Q) of 9 – 14 GHz were performed on pellets with diameter of 13 mm and thickness of 6 mm, by the Hakki-Coleman dielectric resonator method [126] using a Network Analyzer (Keysight P9374A). The relative permittivity (ε_r) and dielectric loss ($tan\ \delta$) at 75 – 110 GHz microwave frequencies were measured using a Swiss to 12 MCK WR-10 dielectric material characterization text fixture connected to a Keysight P5027A Vector Network Analyzer

The temperature coefficient of resonance frequency was measured by the Cavity resonance method across a temperature range of 20 – 80 °C, with the resonance being measured by a Network Analyzer (Keysight P9374A).

To assess the electrical resistivity, 13 mm diameter and 2 mm thick pellets were prepared and polished. Additionally, 200 nm thick platinum electrodes were Sputter Coated (Quorum Q150R) on both flat surfaces. The samples were subjected to a voltage of 1 V which was held for 4 minutes to allow for current stabilization using a Hewlett-Packard 4140B pA Meter / DC Voltage source.

To determine electrical breakdown strength, 13 mm diameter pellets were polished to reduce their thickness from 2 mm to 0.4 mm. The test was conducted applying a DC voltage gradually increasing at a rate of 500 V/s until the electrical breakdown failure occurred on the sample, in reference to the IEEE Std 930™-2004 Guide for the Statistical Analysis of Electrical Insulation Breakdown Data.

The thermal conductivity of the pellets was measured by the Transient Plane Source (TPS) method and by calculation ($\kappa = \alpha\rho C_p$) using the density (ρ), heat capacity (C_p) and thermal diffusivity (α) determined for each sample. The thermal diffusivity (α) was measured using a laser flash system (LFA-467 HT HyperFlash®, Germany). Specific heat (C_p) was measured by differential scanning calorimetry (Netzsch DSC 214, Germany). The uncertainties in thermal conductivity was determined to be ±2%. The hBN-NMO interfaces were analyzed by High Resolution Transmission Electron Microscopy (TEM Talos F200X) and Energy Dispersive Spectroscopy (EDS) mapping.

For characterization of the anisotropic thermal conductivity of NMO-hBN composite, samples with 40 vol.% of filler were fabricated to have 13 mm diameter and 14 mm height. The pellet was cut into two pieces using a slow wire cutter to measure the in-plane direction from one piece and the out-of-plane direction from the other. The thermal conductivity in each anisotropic direction was calculated ($\kappa = \alpha\rho C_p$) using the density (ρ), heat capacity (C_p) and thermal diffusivity (α) determined for each piece of the sample.

5.3 Results and discussion

5.3.1 Cold sintering of NMO and NMO-hBN composites

Bulk pellets of pure NMO and composites of NMO-hBN with filler volume fractions of 0.5 - 50 vol.% were cold sintered and successfully densified to relative densities above 94%, as indicated in Figure 5-1.a, which illustrates the composite samples of NMO-hBN maintaining a consistent average relative density >96% with error bars range determined with Confidence Interval of 95%, for volume fractions of 10 – 50 vol.%. A dilatometry study comparing the relative densities of pure NMO and the NMO-hBN with 40 vol.% of filler demonstrated rearrangement of hBN 2-D flakes in the first few minutes after the application of the uniaxial pressure. The contribution of the rearrangement of hBN flakes to the densification process was calculated by subtracting the relative density of pure NMO from the relative density of the NMO-hBN composite. As indicated in Figure 5-1.b, the maximum contribution of the rearrangement of filler to the bulk relative density is 8%, which is reached in approximately 2 minutes after the application of the uniaxial pressure. After these first 2 to 3 minutes of the cold sintering process, the rearrangement contribution dominates and after a few minutes the densification follows the kinetics associated with the pressure solution processes that control the cold sintering of the pure NMO. The rearrangement and stress shearing of the hBN flakes among NMO particles within the first minutes followed by the longer cold sintering time of the NMO provides an ideal microstructure for these composites. A schematic diagram in Figure 5-1.c, illustrates the condition of the hBN powder particles sheared out as 2-D flakes, as a result of the applied uniaxial pressure, acting then as a mechanical lubricant to optimize the arrangement of NMO grains, with hBN flakes filling in the gaps and uniformly spreading among the ceramic matrix towards percolation. The applied uniaxial pressure during cold sintering process, is sufficient to break the Van der Waals bonds between 2-D planes in the hBN crystal structure, causing the shearing and dispersion of individual hBN flakes around the NMO grains through the matrix. A preferential alignment of the hBN flakes results with its *ab* plane perpendicular to the uniaxial direction of the applied pressure. The microstructure and phase distributions from the microscopy observations are consistent with the schematic diagram. This engineered microstructure of filler 2-D flakes interconnecting to each other and surrounding the matrix grains in the composite, was confirmed by SEM analysis and EDS mapping images in Figure 5-1.d and Figure 5-1.e, respectively. Progression of the composite microstructure with the addition of hBN filler is documented in Figure 5-S5.

5.3.2 Dielectric properties in radio frequency range ($\leq 10^6$ Hz)

The dielectric properties of the cold sintered samples were measured at low frequency of 10^5 Hz and temperatures between 20 and 100°C, as reported in Figure 5-2. The dielectric loss of the NMO-hBN composites was too low to be measured within the capabilities of the LCR meter equipment, therefore the measured dielectric losses at 10^5 Hz are reported here. The composite samples exhibited a systematic decrease of the relative dielectric permittivity as function of filler volume fraction, from $\varepsilon_r = 12.0$ for pure NMO, to $\varepsilon_r = 7.3$ for NMO-hBN 40 vol.% composite, at room temperature. This systematic trend remains present for all the measured temperature range, and while the pure NMO increases its relative permittivity to $\varepsilon_r = 12.8$ at 100°C, the relative permittivity of NMO-hBN 40 vol.% composite only changes to $\varepsilon_r = 7.4$, indicating a contribution from the filler addition to stabilize the relative permittivity for different temperatures. The stability of the permittivity value is improved with the addition of filler volume fraction, in the measured temperature range. The dielectric loss of all samples was measured at 10^5 Hz, resulting in low tan $\delta = \varepsilon''/\varepsilon'$ values between $3.4 \times 10^{-4} – 0.003$ at room temperature, and again a systematic increasing trend was observed for *tan* δ values between 0.001 – 0.019 at 100°C.

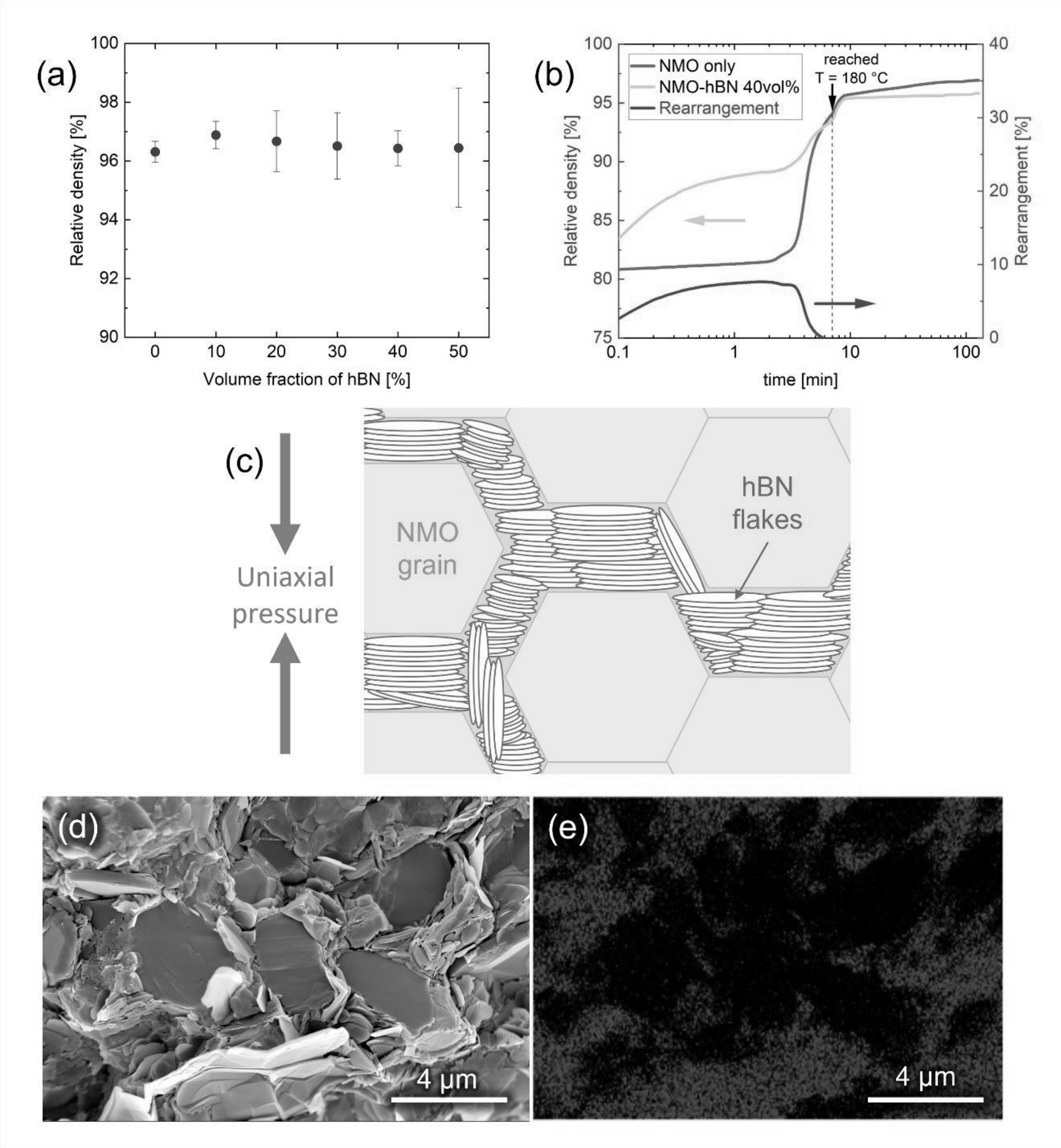

Figure 5-**1**: (a) Relative densities of cold sintered pellets of pure NMO and NMO-hBN composites. (b) Results of the dilatometry study show relative density as a function of time for pure NMO and NMO-hBN composites with 40 vol.% of filler. (c) Engineered microstructure of NMO-hBN cold sintered composites. (d) SEM image of engineered microstructure of NMO-hBN with 40 vol.% of filler, enabled by cold sintering. (e) EDS mapping image of hBN flakes (in red) interconnected towards percolation condition among NMO matrix grains.

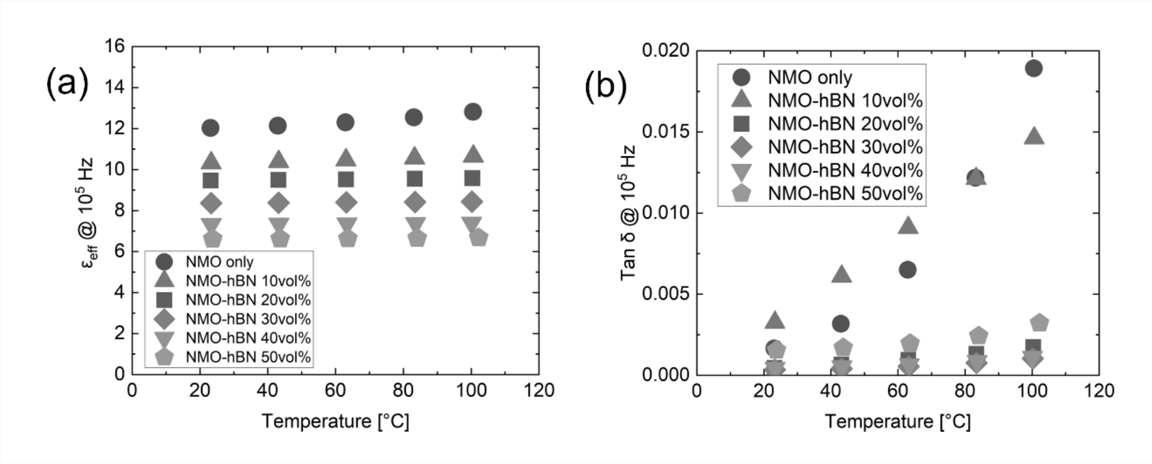

Figure **5-2**: (a) The effective relative permittivity shows a systematic decreasing trend with the addition of filler volume fraction in the composite. (b) Low dielectric loss was reported for all samples within the measured temperature range.

5.3.3 Relationship between microstructure and dielectric properties

Relative permittivity measurements conducted at 10^6 Hz and room temperature, indicate that the effective relative permittivity of NMO-hBN composites fits within the limits of Lichtenecker's general composite mixing law [69, 127], as shown in Fig. 5-3.a. The most general form of the composite mixing law can be expressed as

$$\tilde{\phi}^n = \sum_{i=1}^{N} f_i \phi_i^n \tag{Eq. 5.2}$$

where ϕ_i is the property of the ith phase, f_i is the volume fraction of the ith phase. This is summed over the N-phases making up the composite. $\tilde{\phi}$ is the property that is averaged through the composite mixing, and n is the exponent that ranges from $-1 \leq n \leq +1$. The n value is indicative of the series or parallel mixing that reflects the spatial connectivity of the respective phases.

Laturia et.al., have reported relative permittivities in plane $\varepsilon_{hBN}\parallel = 6.93$ and out of plane $\varepsilon_{hBN}\perp = 3.76$, for the anisotropic properties of hBN. [128] The resulting effective permittivity of hBN

$\varepsilon_{hBN\ eff}$ = 4 would then be attributed to a higher contribution from the permittivity corresponding to the out of plane ($\varepsilon_{hBN}{}^{\perp}$) direction. The systematically decreasing trend in ε_{eff} towards the previously reported out of plane value suggests that the hBN flakes are highly oriented in the out of plane direction, which is strongly supported by the dielectric measurements, HR-TEM and STEM images in this section, as calculated by considering the limiting exponent of $n \rightarrow 0$ in the logarithmic mixing law

$$log\tilde{\varepsilon}_r = f_1 log\varepsilon_{r1} + f_2 log\varepsilon_{r2} \qquad \text{(Eq 5. 3)}$$

HR-TEM analysis was conducted at the interface between NMO grain and hBN flake, revealing a clean interface without secondary phases. The crystallinity of the NMO grain clearly contrasts with the *ab* 2D-planes of hBN filler, which is observed preferentially aligned parallel to the grain boundary of the ceramic matrix. The HR-TEM image in Figure 5-3.b, together with the STEM image and EDS mapping in Figures 5-3.c and 5-3.d, correlates this preferential alignment of the hBN flakes with the relative permittivity measured and calculated.

5.3.4 Dielectric properties at microwave frequencies (9-13 GHz)

The Hakki-Coleman method was used to determine the relative permittivity and dielectric loss at the dielectric resonance frequency of the samples at room temperature. The resonance frequencies of the samples were measured within the range of 9 – 13 GHz, and the corresponding dielectric properties are shown in Figure 5-4. As in the low frequency measurements, the relative permittivity of the samples fit within the limits of the composite general mixing law for hBN effective permittivity of $\varepsilon_{hBN\ eff}$ = 4. The dielectric loss of pure NMO was 3.0×10^{-4}, while the NMO-hBN composites exhibited *tan δ* values within the range of 6.5×10^{-4} to 7.5×10^{-4}. The corresponding $Q \times f$ values of pure NMO was 21,900 and for the NMO-hBN composites it varied between 13,000 – 16,000. These measured dielectric properties position the NMO-hBN cold sintered composite as an adequate candidate for microwave substrate applications. [129]

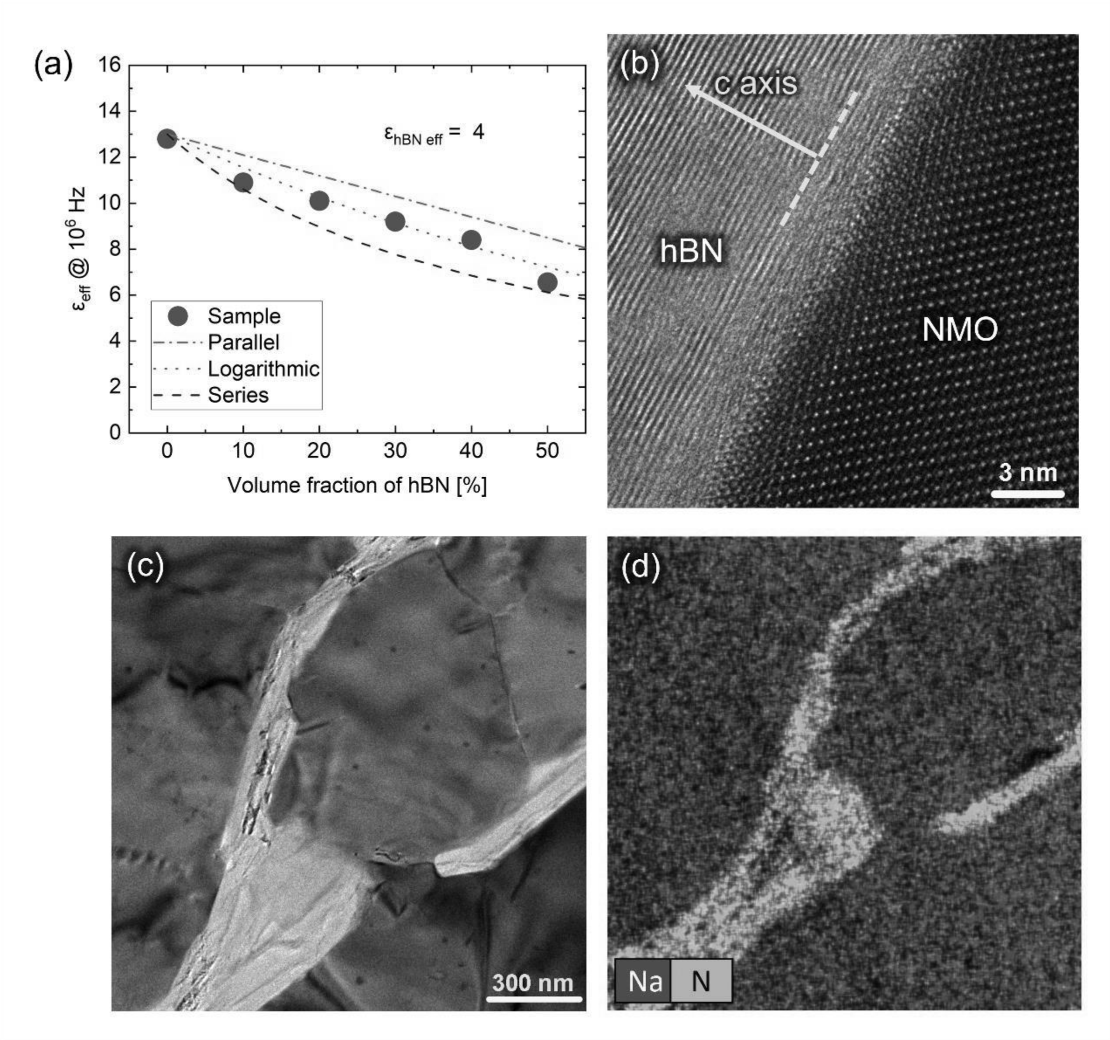

Figure **5-3**: (a) Dielectric measurements at 1 MHz show the effective relative permittivities (ε_{eff}) for NMO-hBN composites. (b) HR-TEM image confirms the preferential alignment of hBN flakes parallel to the grain boundary of NMO. (c) STEM image of hBN flakes surrounding the NMO grain towards percolation condition, with preferential alignment parallel to the grain boundaries. (d) EDS mapping of hBN (blue) surrounding NMO grains (red).

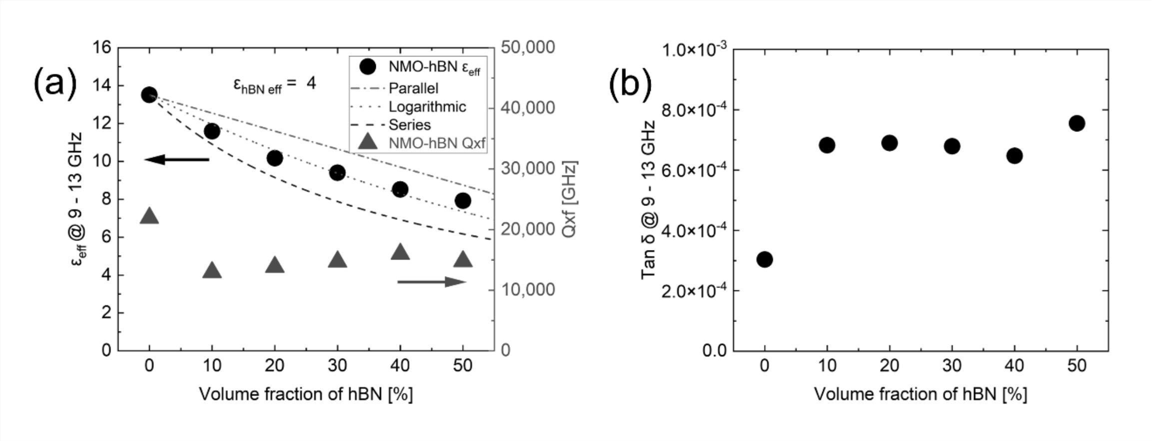

Figure **5-4**: (a) Dielectric measurements at resonance frequencies of 9 – 13 GHz show that the effective relative permittivities (ε_{eff}) for NMO-hBN composites fit a logarithmic mixing law calculated by $\varepsilon_{hBN\ eff} = 4$. (b) Low dielectric loss was measured for pure NMO and NMO-hBN composites.

5.3.5 Dielectric properties at microwave frequencies (75-110 GHz)

Dielectric properties of cold sintered samples were analyzed at 75-110 GHz microwave frequencies. At room temperature, the dielectric constant (ε_r) of composites systematically decreased with increasing filler volume from $\varepsilon_r = 13.4$ in pure NMO, to $\varepsilon_r = 8.4$ in NMO-hBN 40 vol.% composite. The corresponding dielectric loss ($tan\ \delta = \varepsilon''/\varepsilon'$) showed low values between 3.9×10^{-3} and 6.8×10^{-3}. This behavior illustrated in Figure 5-5, aligns with structure-dielectric properties relationship in grain boundary engineered NMO-hBN composites at lower frequencies, again fitting well Lichtenecker's mixing power law.

For high microwave frequencies between 75 – 110 GHz, the effective permittivity of hBN was also determined as $\varepsilon_{hBN\ eff} = 4$. This value is consistent with previous measurements at lower frequencies on cold sintered NMO-hBN composites. It primarily reflects the permittivity in the out-of-plane direction ($\varepsilon_{hBN}{}^{\perp}$). This outcome is systematically linked to the engineered microstructure of grain boundaries, where 2D hBN flakes are preferentially aligned perpendicular to the uniaxial pressure applied during cold sintering. Calculations for the composites' relative permittivity, utilizing a logarithmic mixing law with a limiting exponent n→0 (Eq. 5.3), reinforce the suitability of NMO-hBN cold-sintered composites for microwave substrate applications.

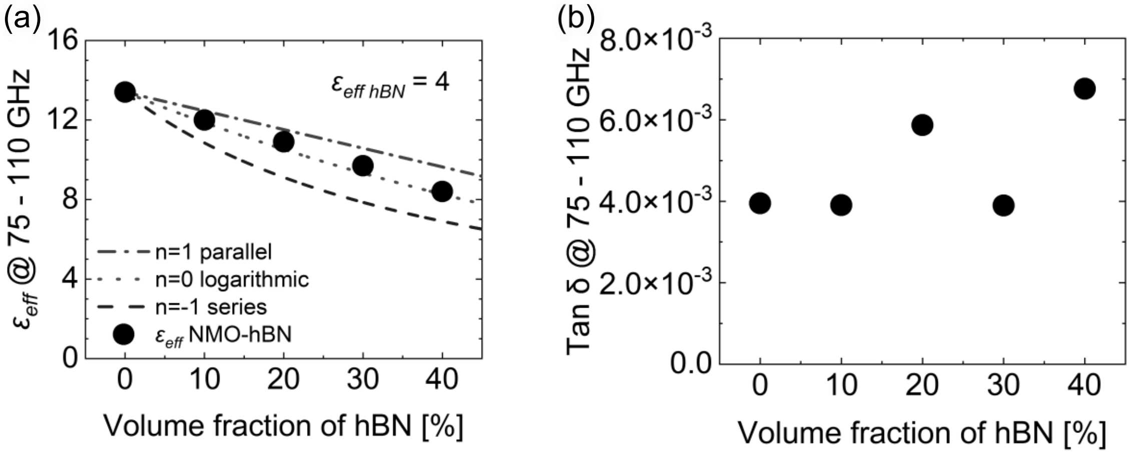

Figure **5-5**: (a) Evolution of the effective relative permittivity (ε_{eff}) at 75-110 GHz, fitting a logarithmic mixing law with $\varepsilon_{hBN\ eff} = 4$, and (b) corresponding dielectric loss as function of filler volume fraction.

5.3.6 Temperature coefficient of resonance frequency

The thermal coefficient of resonance frequency of the NMO-hBN composite was also studied as the individual input of each phase contributes to an effective thermal coefficient of the microstructurally engineered composite. The analysis of this property begins from the previously mentioned general composite mixing law (Eq. 5.2). In the case of spatially mixing of series and parallel connectivity, the limiting exponent of n→0 is considered. In this limit, as in the case of the mixing law for relative permittivity (ε_r), the Lichtenecker's logarithmic mixing law for a diphasic composite is obtained, which is Equation 5.3. If this is differentiated with respect to temperature, we readily obtain the mixing law for the temperature coefficient of relative permittivity, TC_ε

$$TC_{\varepsilon} = \frac{1}{\tilde{\varepsilon}}\frac{d\tilde{\varepsilon}}{dT} = f_1 TC_{\varepsilon 1} + f_2 TC_{\varepsilon 2} \qquad \text{(Eq. 5.4)}$$

So the temperature coefficients scale with a linear dependence of the respective volume fractions and the independent temperature coefficients of these phases.

The temperature coefficient of frequency of a dielectric resonator is given by

$$TC_f = -\left(\frac{1}{2}TC_{\tilde{\varepsilon}} + \tilde{\alpha}\right) \qquad \text{(Eq. 5.5)}$$

where $\tilde{\alpha}$ is the linear coefficient of thermal expansion of the composite.

The $\tilde{\alpha}$ is also able to be estimated with a mixing law. This was first given by Turner as

$$\tilde{\alpha} = f_1\alpha_1 + f_2\alpha_2 \qquad \text{(Eq. 5.6)}$$

Collecting all these equations and substituting into Eq. 5.3 gives a simple linear mixing law for the TC_f

$$TC_f = f_1 TC_{f1} + f_2 TC_{f2} \qquad \text{(Eq. 5.7)}$$

so very much like the temperature coefficient of relative permittivity, the temperature coefficient of resonance also scales linearly.

The pure NMO and NMO-hBN composite samples were measured at high frequencies (9 – 13 GHz) by the cavity method at different temperatures to determine how its resonance frequency shifts as a function of temperature. These measurements were used to calculate the temperature coefficient of resonance frequency (*TCF*) [16, 130], according to the Equation 5.8.

$$TCF = \frac{1}{f_0}\frac{\Delta f}{\Delta T} \times 10^6 \quad [ppm/°\mathrm{C}] \qquad \text{(Eq. 5.8)}$$

The plot in Fig. 5-5 illustrates that the pure NMO sample exhibited a TCF = -43 ppm/°C while for the NMO-hBN composites, their TCF_{eff} values varied between ranges of -33 to -13 ppm/°C, for temperatures between 20 °C and 80 °C. The linear regression of these values was calculated by the least squares method, for a standard error of the estimate = 1.67 ppm/°C. With the addition of hBN filler volume fraction, the TCF_{eff} values become closer to zero. This is a desired feature in materials for microwave substrate applications, minimizing the shift of resonance frequency as function of temperature within the operation conditions, preventing the necessity of additional circuitry adjustments.

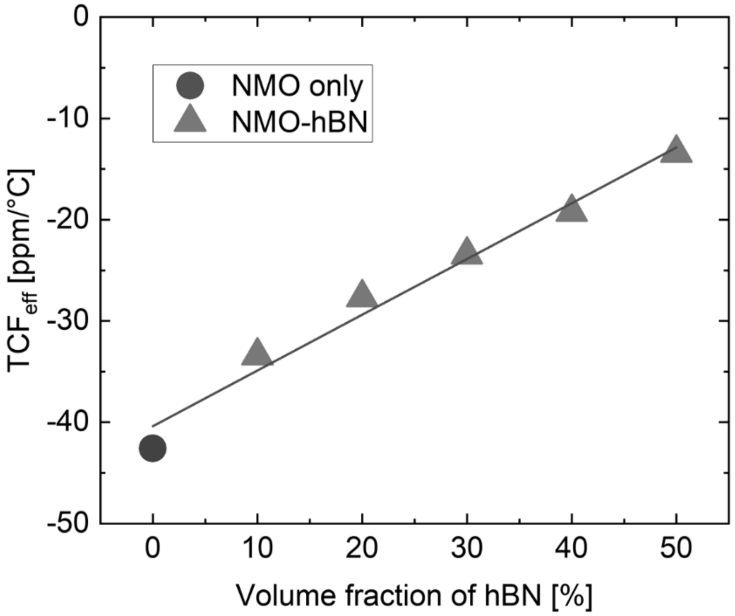

Figure **5-6**: The effective temperature coefficient of resonance frequency (TCF_{eff}) becomes closer to zero with the addition of filler volume fraction in NMO-hBN composites, within the temperature range of 20°C – 80°C.

5.3.7 Thermal conductivity

The thermal conductivity of pure NMO and NMO-hBN composites was measured by the Transient Plane Source method, which showed an improvement in thermal conductivity (κ) as a function of the filler volume fraction, from 1.7 W m^{-1} K^{-1} for pure NMO, up to ~12 W m^{-1} K^{-1} for 50 vol% of hBN filler. The non-linear improvement of thermal conductivity fits closely to the n=0 logarithmic mixing law for $\kappa_{hBN\ eff}$ = 70 W m^{-1} K^{-1}. The thermal conductivity was additionally calculated via Equation 5.9

$$\kappa = \alpha \rho C_p \qquad \text{(Eq. 5.9)}$$

in which κ is the thermal conductivity, α is the thermal diffusivity as measured by LFA, ρ is the density and C_p is the specific heat capacity as measured by DSC. The improvement in thermal conductivity (κ) from the LFA/DSC calculation as a function of the filler volume fraction ranged from 1.7 W m^{-1} K^{-1} for pure NMO, to ~6 W m^{-1} K^{-1} for 50 vol% of hBN filler. By this second method, the non-linear improvement of thermal conductivity fits closely to the n=0 logarithmic mixing law for $\kappa_{hBN\,eff} = 30$ W m^{-1} K^{-1}. [131, 132] These results are shown in Figure 5-7. The discrepancy of thermal conductivity obtained from LFA and DSC for nanocomposite materials is heavily dependent on the homogeneity of nanoparticles, e.g., hBN filler. The insufficient or excessive hBN in the sample for heat capacity measurement can either lead to lower or higher measured thermal conductivity, respectively. It is also important to note that LFA is a cross-plane one dimensional measurement of thermal conductivity, while transient plane source (TPS) volumetrically samples both the in- and cross-plane thermal conductivities. As such, the TPS measurements see an increased benefit to the thermal conductivity from the hBN network as it becomes a larger volume fraction of the sample. The TPS measurement more closely mimics the dissipation of heat from a hot spot that may be representative of its use in high power, high frequency applications. Up to a volume fraction of 30% the measured thermal conductivity values are similar between TPS and the LFA/DSC measurements. Even with the discrepancy between the values at high hBN volume fractions, the thermal conductivity of composites at room temperature from TPS and LFA/DSC increase with the increase of hBN, which is desired for new dielectric substrates materials.

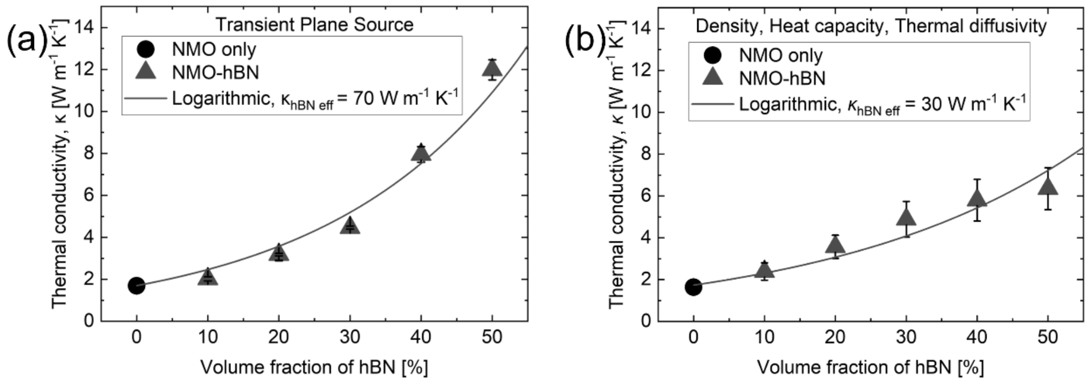

Figure **5-7**: The improvement of thermal conductivity as a function of filler volume fraction was evident for the NMO-hBN composites. The measurements of this thermal property conducted by (a) transient plane source and (b) calculations by density, specific heat capacity and thermal diffusivity.

5.3.8 Anisotropic thermal conductivity of NMO-hBN composite

Results in the previous section have shown that thermal conductivity (κ) of cold sintered pure NMO is ~1.7 W m^{-1} K^{-1} , and for NMO-hBN composites it increases with the filler volume, following a logarithmic mixing law with an effective $\kappa_{hBN\ eff}$ = 30 W m^{-1} K^{-1}.[45, 46, 131, 132] As previously mentioned, the cold sintering process, involving uniaxial pressure, results in the hBN flakes aligning perpendicularly to the applied force, leveraging its anisotropic thermal conductivity. This anisotropy arises from the strong covalent bonds in the in-plane direction, enhancing thermal management capabilities compared to the out-of-plane direction. For the NMO-40 vol.% hBN samples, thermal conductivity was assessed in both directions using Equation 5.9. Figure 5-8 illustrates the anisotropic thermal conductivity of the NMO-40 vol.% composite, which remains steady between 25°C and 100°C. As anticipated, conductivity is greater in the in-plane direction, a result of the hBN flakes aligning preferentially under the uniaxial pressure applied during the cold sintering process.

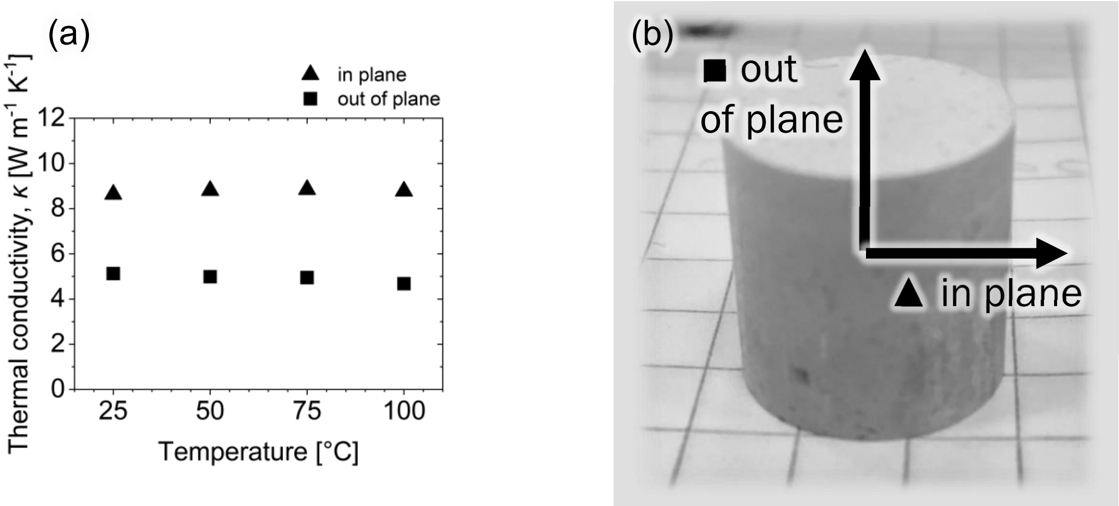

Figure **5-8**: (a) In-plane and out-of-plane thermal conductivity versus temperature for cold sintered NMO-40 vol.% hBN composite. (b) Photo of the NMO-40 vol.% hBN composite with measurement directions. The dimensions of the pellet in the image are 13 mm in diameter and 14 mm in height.

5.3.9 Resistivity and fit to percolation theory

The electrical resistivity of NMO-hBN composites varies with filler volume fraction, calculated from the electrical current and pellets' physical dimensions using the following Equation 5.10:

$$\rho = \frac{R \cdot \pi r^2}{l} \qquad \text{(Eq. 5.10)}$$

where *ρ, R, r* and *I* respectively represent the resistivity, resistance, radius, and thickness of the pellet.

Pure NMO samples exhibited a resistivity around 10^{11} Ω•cm while composite samples with hBN reached resistivity levels up to 10^{14} Ω•cm. A notable increase in resistivity at 2 vol.% hBN, as illustrated in Figure 5-9, introduces an intriguing aspect to the concept of percolation, challenging traditional expectations where a filler enhances percolation in a non-conductive matrix.

Typically, percolation is considered with a filler phase in a non-conducting matrix. In this study, a reasonable microwave dielectric material NMO is used as a highly resistive ceramic matrix, and then an even higher resistivity material is added into the grain boundaries. For cold sintered NMO-hBN composites, the hBN flakes are blocking the conduction paths and thereby improving the resistivity with increasing volume fraction of fillers. This is a most interesting and beneficial observation of the cold sintered composites. It is noteworthy that this change is different from the pure mixing law variation with dielectric and thermal properties.

The 2D nature of the hBN made such behavior possible given its ability to shear upon the applied stress of the press during the cold sintering process. As a result, the sheared layers of resistive hBN easily enveloped the NMO grains, forcing conduction between the NMO grains to pass through the resistive layer. This dispersion of material amongst the grain boundaries allows for a swifter change in resistive behavior compared to random filler distribution. Shearing the 2D material yields a greater surface area of contact with the NMO grains per volume fraction of filler as the hBN is wedged between the grain boundaries. The resulting percolation trend for measuring the composite's resistivity is composed of two sections. The fitting curve below the percolation threshold is described by the Equation 5.11:

$$\rho = \rho_m \left(\frac{\varphi_c - \varphi_f}{\varphi_c} \right)^{-s} \qquad \text{(Eq. 5.11)}$$

where ρ is the effective resistivity of the composite, ρ_m is the resistivity of the ceramic matrix, ϕ_f is the volume fraction of the filler, ϕ_c is the percolation threshold, and s is the critical exponent corresponding to the percolation theory. For the fitting curve above the percolation threshold, the fitting equation (Eq. 5.12) is:

$$\rho = \rho_f \left(\varphi_f - \varphi_c \right)^{t} \qquad \text{(Eq. 5.12)}$$

where ρ is the effective resistivity of the composite, ρ_f is the resistivity of the filler, ϕ_f is the volume fraction of the filler, ϕ_c is the percolation threshold, and t is the critical exponent corresponding to the percolation theory.[64]

For fitting the effective electrical resistivity (ρ) of the composites to percolation theory (Eqs. 5.11 and 5.12), the parameters were as follows: matrix resistivity $\rho_m = 10^{11}$ Ω•cm, filler resistivity $\rho_f = 10^{15}$ Ω•cm, percolation threshold $\phi_c = 2.0$ vol.% hBN, and critical exponents s and t at 2.0 and 0.8, respectively. These findings are consistent with numerous studies on 2D materials as fillers, which often report percolation thresholds under 2.0 vol.% filler content. This is particularly evident in the electrical properties of composites using materials like graphene as filler.[133–136]

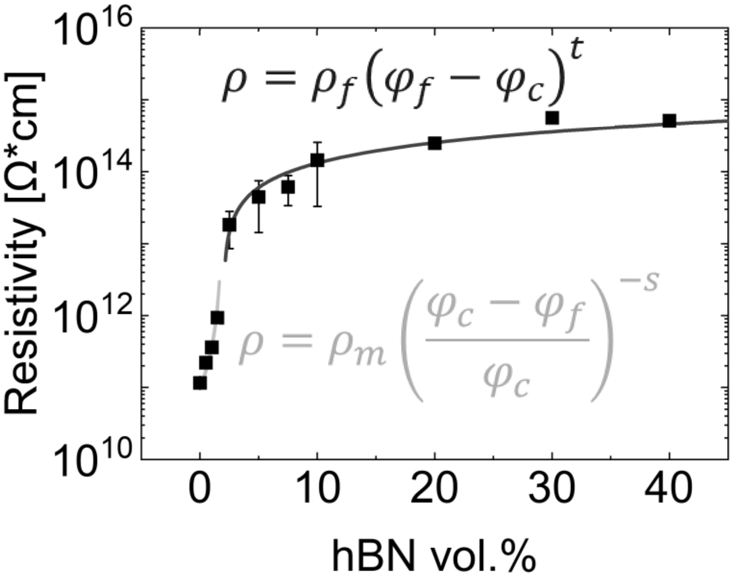

Figure **5-9**: Resistivity as a function of hBN volume fraction in NMO-hBN composites. Light and dark blue lines on the graph represent fits to equations Eq. 5.11 and Eq. 5.12, for regions below and above the 2 vol.% percolation threshold, respectively.

5.3.10 Electrical breakdown strength

From earlier works on cold sintered ceramic matrix composites, it is known that grain boundary inclusions can impact the breakdown field.[43, 53, 90, 137] It could be anticipated that the controlling breakdown strength in the NMO is a thermal breakdown process. The increase in thermal conductivity and the increase in electrical resistivity should be of benefit to raising dielectric breakdown strength. This is rationalized for the case of thermal breakdown, where there is a balance between the thermal properties and the Joule heating as shown by Equation 5.13:

$$C_v \frac{dT}{dt} - div\,(\kappa\, grad\, T) = \sigma E^2 \qquad \text{(Eq. 5.13)}$$

here C_v is the specific heat per unit volume, κ is the thermal conductivity, T is the temperature, t is the time, σ is the electrical conductivity, and E is the applied electric field. Equation 5.13 is a balance between the heat absorbed and the heat lost to the surroundings with heat conducted away, with the first and second term on the left hand side of the equation, the term on the right hand side is the Joule heating that is continuously being generated from the conduction, and/or the dielectric loss mechanism.[138, 139]

To assess the quality of the solid dielectric strength of the samples, the scatter of the electrical breakdown voltage in the experimental results was analyzed according to the Weibull probability distribution described by Equation 5.14:

$$F(V) = 1 - exp\left\{-\left(\frac{V}{\alpha}\right)^{\beta}\right\} \qquad \text{(Eq. 5.14)}$$

where V is the breakdown voltage, α is the scale parameter which represents the voltage required for 63.2% of the tested samples to fail, and β is the shape parameter which represents a measure of dispersion of the breakdown voltages.[140, 141]

Electrical breakdown (E_b) tests on NMO-hBN composites revealed enhanced electrical breakdown strength and β values with hBN addition. While the composite samples show a unimodal distribution according to Weibull statistics, the distribution for pure NMO exhibits a bimodal characteristic, with β values of 5.7 ± 1.2 and 2.7 ± 0.6 as determined through a Weibull mixture model. With the addition of 20 vol.% of hBN, the E_b = 96.3 kV/mm, approaching the maximum capability limits of the high voltage DC source of 30 kV applied. For samples at 30 vol.% and 40 vol.% hBN, 30 kV did not induce breakdown, suggesting higher resilience. These samples had a 13 mm diameter and thickness ranging from 0.3 to 0.5 mm. As shown in Figure 5-10, Weibull analysis demonstrated consistent improvements in E_b and the shape parameter (β) with increased hBN content, pointing to a narrower breakdown voltage range.

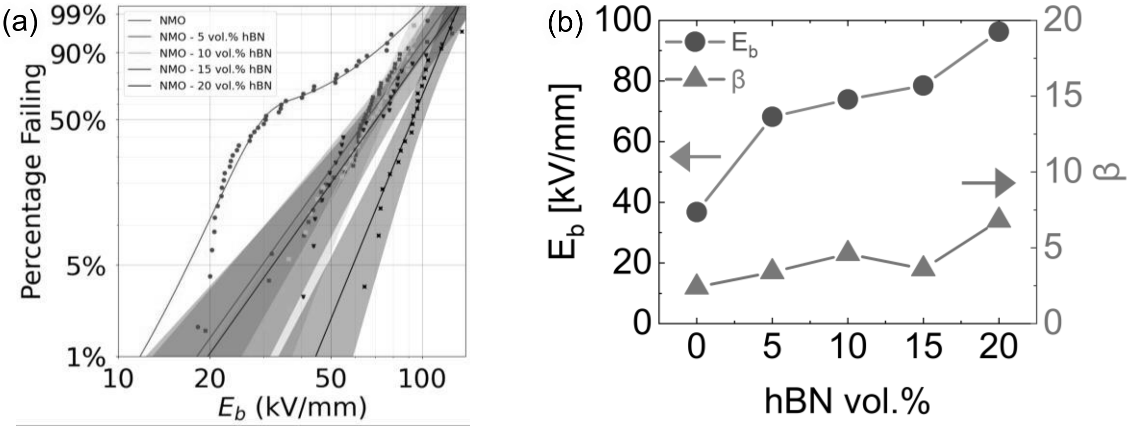

Figure 5-**10**: (a) Weibull statistical analysis and (b) results of electrical breakdown strength (E_b, β) for NMO-hBN composites as function of filler volume fraction.

5.4 Conclusions

NMO powder was synthesized with unimodal particle size distribution to successfully fabricate pellet samples of NMO-hBN composite by the cold sintering process. The cold sintered composites present an engineered microstructure of interconnected hBN filler flakes in a percolation condition, achieving mean relative densities greater than 96% for filler volume fractions between 0.5 and 50 vol.%.

A dilatometry study demonstrated the influence of hBN flakes rearrangement among the NMO grains to rapidly reach higher relative density than the pure NMO sample during the first minutes of the cold sintering process.

The dielectric properties of the composites were measured at low frequencies of 10^5 and 10^6 Hz, revealing that the effective relative permittivity of hBN filler is strongly determined by its anisotropic properties and by the preferential alignment parallel to the grain boundaries of NMO grains, enabled by the uniaxial applied pressure during the cold sintering process. This preferential alignment of the hBN flakes was confirmed by HR-TEM analysis, STEM and EDS mapping. Dielectric measurements were also performed at high frequencies of 9 – 13 GHz, and as in the low frequency measurements, the relative permittivity of the NMO-hBN composites also fit within the limits of the Lichtenecker general mixing law for filler volume fractions between 10 – 40 vol.%, and their dielectric loss is low enough to meet the required values for microwave substrates applications. The $Q \times f$ values of the composites were within the range of 13,000 – 16,000 GHz. Dielectric testing at 75-110 GHz frequencies and room temperature showed that relative permittivity aligns with the Lichtenecker general mixing law, having an effective hBN permittivity ($\varepsilon_{hBN\ eff}$) of 4 for 10-40 vol.% filler fractions, with dielectric loss ($tan\ \delta$) ranging from 3.9×10^{-3} to 6.8×10^{-3}.

The temperature coefficient of resonance frequency was determined for the pure NMO and NMO-hBN composites, indicating closer measurements to the desired value of zero with the increase of filler volume fraction.

The thermal conductivity was measured by the Transient Plane Source method showing an increase from 1.7 W m^{-1} K^{-1} for pure NMO to ~12 W m^{-1} K^{-1} for NMO-hBN composite with 50 vol% of filler. The thermal conductivity calculated by measuring the density, specific heat capacity and thermal diffusivity of the samples, showed an increase to only ~6 W m^{-1} K^{-1} for NMO-hBN composite with 50 vol% of filler. Anisotropic thermal conductivity measurements, influenced by the hexagonal boron nitride's crystal structure, confirmed distinct in-plane and out-of-plane conductivities.

The NMO-hBN composites' resistivity increased with filler addition, consistent with percolation theory predictions. A percolation threshold was noted at 2.0 vol.% hBN. Then, a significant resistivity increase of three orders of magnitude was observed at 10 vol.% hBN, and four orders at 40 vol.% hBN.

The electrical breakdown strength also improved with increments of hBN in the composite, and not only the insulation breakdown increased, but the shape parameter (β) exhibited higher values compared to the pure NMO material, indicating a reduction in the range of the breakdown voltage with the increase of filler volume fraction.

These findings on the dielectric, electrical, and thermal behaviors of cold sintered NMO-hBN reinforce its potential as a novel material for high-frequency microwave substrate applications, building upon and extending previously reported properties.

5.5 Supplemental figures to Chapter 5

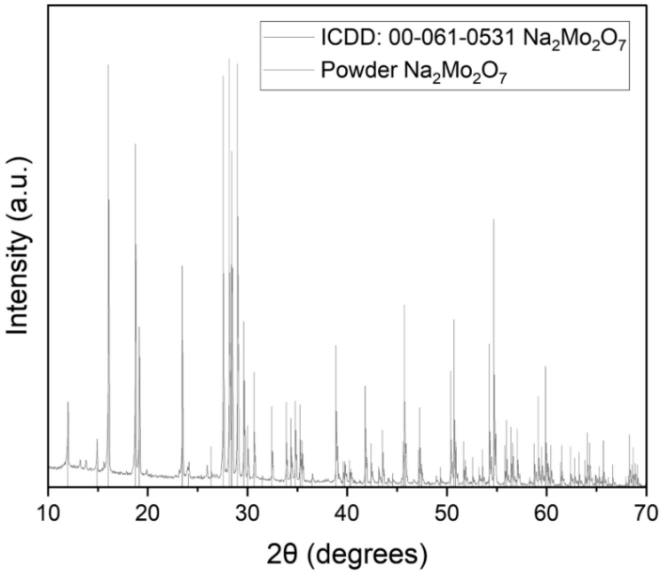

Figure **5-S1**: XRD data of synthesized $Na_2Mo_2O_7$ and its corresponding ICDD 00-061-0531 card standard. Minor intensity peaks at 13.210°, 13.797°, 19.866° and 25.918° correspond to traces of $Na_6Mo_{11}O_{36}$ (ICDD card 00-056-0435).

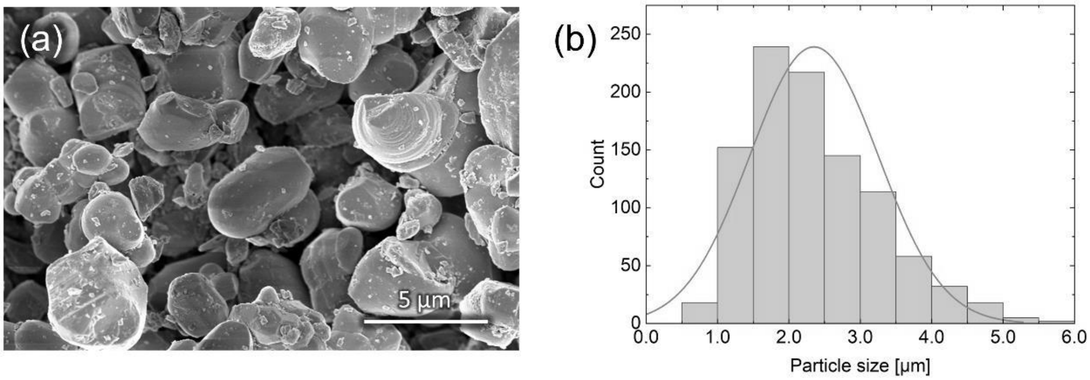

Figure **5-S2**: (a) SEM image showing morphology of individual particles of NMO powder after 30 minutes of dry ball milling. This is the condition of the ceramic particulate as used prior to the cold sintering process. (b) Individual particles were measured from SEM images and a unimodal particle size distribution of the processed NMO powder is shown with mean particle size of 2.4 ± 0.9 µm.

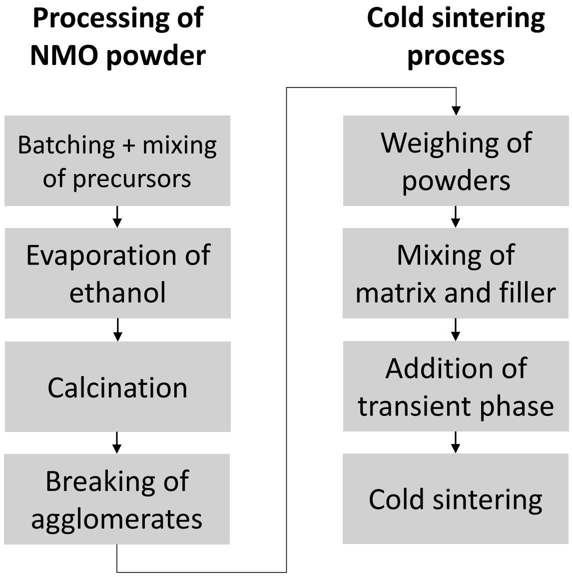

Figure **5-S3**: Process flow diagram of steps for the synthesis of NMO powder and fabrication of NMO-hBN composite pellets by cold sintering process.

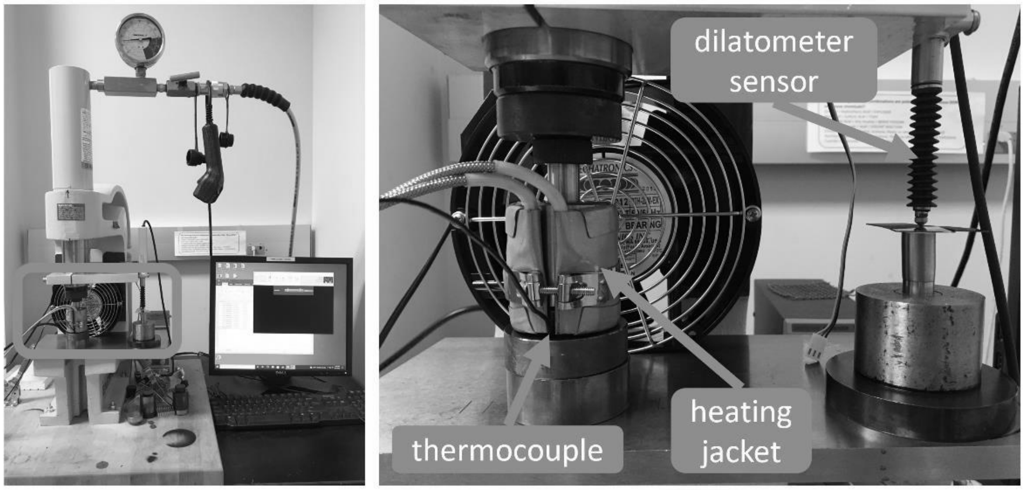

Figure **5-S4**: Setup for dilatometry study.

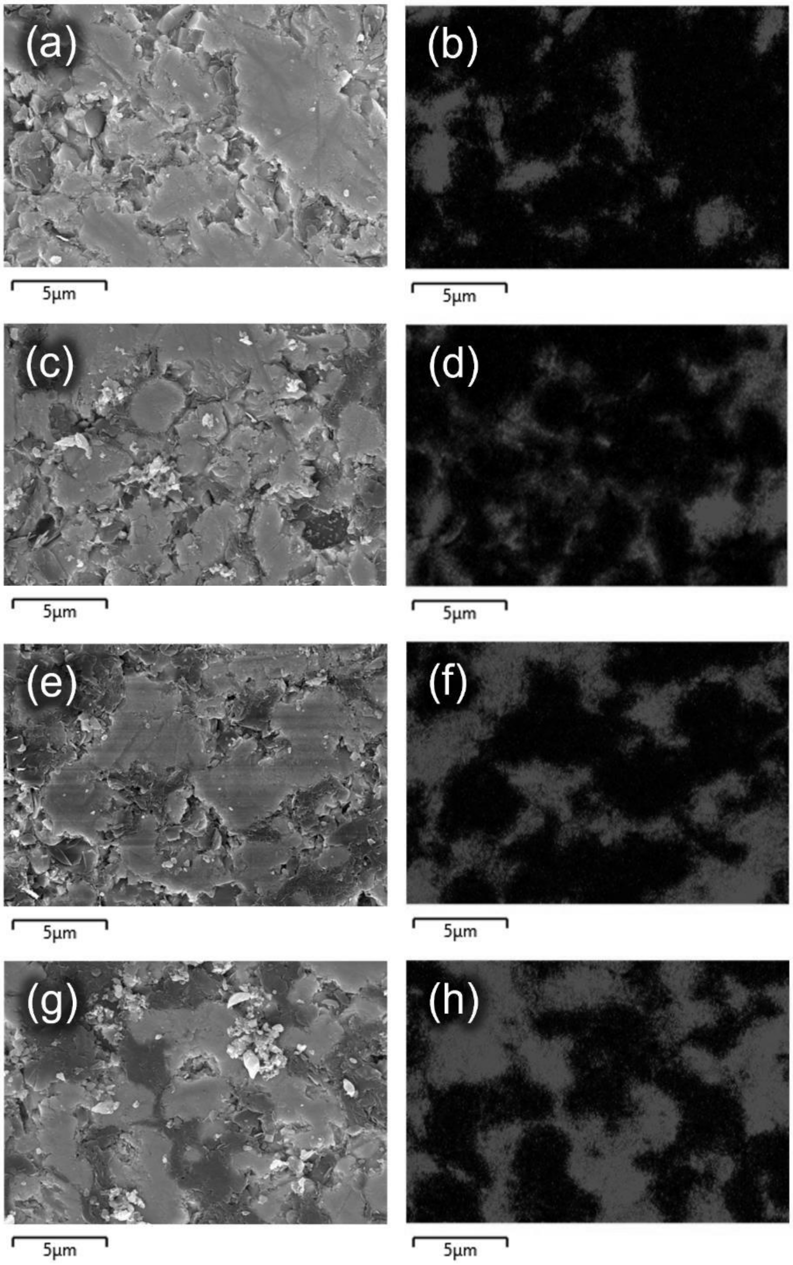

Figure **5-S5**: SEM images of microstructure and EDS mappings of NMO-hBN cold sintered composites with (a,b) 10 vol.%, (c,d) 20 vol.%, (e,f) 30 vol.% and (g,h) 40 vol.%, showing progressive interconnectivity of hBN filler (in red) towards percolation condition among NMO matrix grains.

Chapter 6

Sodium Molybdate-Diamond Dielectric Composites Enabled by Cold Sintering

The increasing demands for more bandwidth across microwave frequency communication technologies constitute a pressing need for the development of novel dielectric substrates capable of seamless integration into packages and devices, with minimal dielectric loss and high thermal conductivity. In this study, dielectric composites of sodium molybdate $Na_2Mo_2O_7$ (NMO) as a ceramic matrix, and diamond as a filler with higher thermal conductivity, are processed via cold sintering, to produce pellet samples with low dielectric loss ($tan\ \delta$) and enhanced thermal conductivity (κ), for microwave applications of high power and frequency. The physical properties of the cold sintered composites were analyzed across a range of filler volume fractions, temperatures, and frequencies. A comprehensive discussion of the results in microstructure and measured dielectric and thermal properties is presented through a systematic analysis of their respective transport mechanisms.

6.1 Introduction

Composite microwave dielectrics are of interest to balance dielectric and thermal properties. $Na_2Mo_2O_7$ (NMO) is used as a model intermediate dielectric material. Figure 6-1 shows the primitive and conventional unit cells of $Na_2Mo_2O_7$ with a space group *Cmca* and the lattice parameters a, b and c are 7.17, 11.83 and 14.70 Å, respectively. There are 4 formula unit cells within the primitive cell. Within the structure there are tetrahedral MoO_4^{-4} groups and octahedral MoO_6^{-6} groups as the polyhedral building blocks.[142–145] Among its applications, $Na_2Mo_2O_7$ is often considered for cryogenic bolometric scintillators for beta decay and dark matter detectors.[146, 147] In addition, it has attractive intermediate dielectric properties as summarized in Table 6-1, and is considered as a potential ultra-low temperature cofired ceramic (ULTCC).[16, 148–150]

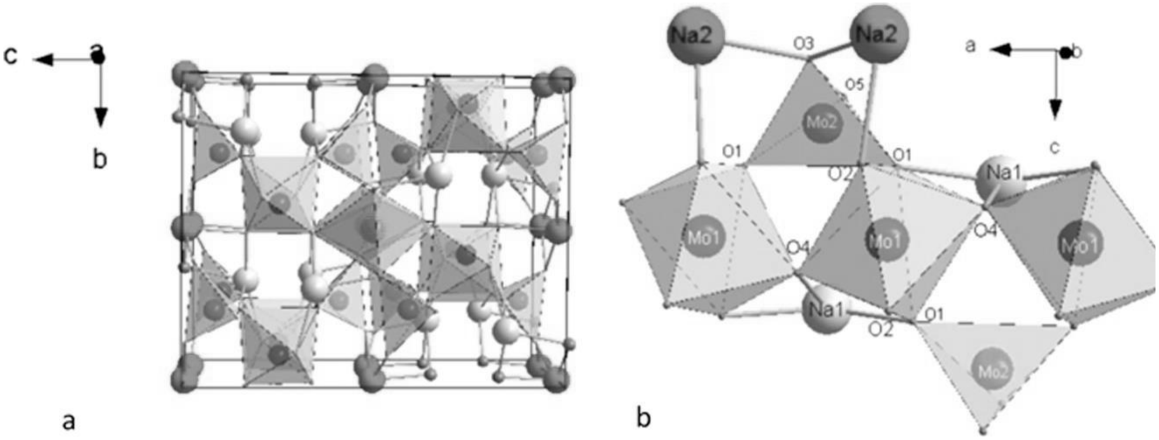

Figure **6-1**: Crystal structure of $Na_2Mo_2O_7$, showing the tetrahedral MoO_4^{-4} and octahedral MoO_6^{-6} distribution along the c axis. Figure reproduced from reference[144] with permission.

Table **6-1**: Microwave dielectric properties of ultra-low temperature sintering $Na_2Mo_2O_7$.[150]

Composition	Sintering Temperature [°C]	f [GHz]	ε_r	$Q \times f$ [GHz]	τ_f [ppm/°C]	Relative density [%]
$Na_2Mo_2O_7$	575	8.415	12.9 ± 0.1	62,400 ± 1,200	-72 ± 1	97

$Na_2Mo_2O_7$ is a ceramic that can be cold sintered into dense material and maintains high performance dielectric properties. Cold sintering is a process that utilizes a non-equilibrium chemomechanical process that densifies ceramic and metal powders using a transient liquid phase, low temperatures (<300°C) and intermediate applied stresses of a few hundred MPa. The mechanism that drives the sintering is known in the geophysics community as pressure solution creep, where it densifies sedimentary rocks over millions of years. With cold sintering, ceramic materials can be sintered in time frames that are attractive to manufacturing processes. Pressure solution creep involves three sequential processes: dissolution, transport along grain boundaries, and precipitation. In the case of $Na_2Mo_2O_7$ the transient liquid phase is water, and the dissolution reaction follows:

$$Na_2Mo_2O_7 + 2H_2O \leftrightarrow 2NaOH + 2(H_2MoO_4) + \frac{1}{2}O_2$$

The Na^+ ion complexes and forms NaOH and the Mo-complexes to form Molybdic acid, so there is a congruent dissolution of the cations. This can form a gel at the interfaces and precipitates in the low chemical potential regions of the pores to complete the densification. The ability to understand the grain growth and the densification of the NMO has been previously discussed by Ndayishimiye, et al.[124] The cold sintering of $Na_2Mo_2O_7$ therefore offers a model system to use as a microwave dielectric matrix phase to test out composite concepts that could impact other microwave materials.

Diamond fillers are an important additive to form a composite with the $Na_2Mo_2O_7$, as it has a high thermal conductivity, and high resistivity. The objective of this study is to explore the structural property processing relations for $Na_2Mo_2O_7$-diamond composites with various volume fractions of fillers. The thermal conductivity of diamond fillers is impacted by the particle sizes, with the thermal conductivity falling rapidly with nano sized diamond. For this investigation, microsized diamond fillers were selected, which are often used in grinding media and are lower cost than nano diamonds.

6.2 Experimental methods

6.2.1 Cold sintering process

The synthesis of sodium molybdate ($Na_2Mo_2O_7$) NMO powder for the cold sintering of the NMO-diamond composites, was the method previously described in Section *5.2.1 Powder* *preparation* of this dissertation. The NMO powder obtained under the specified conditions,[44] was analyzed by X-Ray Diffraction and it showed a pure phase in agreement to ICDD Standard 00-061-053. Following this, the calcinated powder underwent additional ball milling in a dry environment for 30 minutes to disperse the agglomerates of NMO grains into isolated particles.[45] The pure NMO powder was subsequently mixed with 10%, 20%, 30%, and 40% vol. of microsized diamond (natural, 1-3 µm, MANT USA Inc.) for the cold sintering process of composites.

For the fabrication of each pellet, the NMO matrix and diamond filler powders were weighed for every sample in accord with the intended filler volume fraction. These weighed powders were combined in a glass vial and mixed using a planetary centrifugal mixer (Thinky, AR-250) for 10 cycles, each lasting 1 minute. Following centrifugal mixing, 25 wt.% of deionized water was added to the evenly mixed powder using a pipette. Subsequently, the powder and the transient chemistry, H_2O, were manually mixed in an agate mortar with a pestle for approximately 10 minutes until achieving a homogeneous appearance. The moistened powder was then transferred to a stainless steel die for cold sintering. Applying a uniaxial pressure of 250 MPa using a press (Carver, model CH4386), the assembly was heated up to temperatures between 180°C and 220°C for 2 hours using a heating jacket wrapped around the die, controlled by a PID loop feedback mechanism. A thermocouple was positioned in the lower piston of the die to monitor the temperature. After the dwell time, the pellet was ejected from the die and left to cool down to room temperature under ambient conditions. Finally, the cold-sintered pellets were dried out in air at 200°C for 12 hours.

Dilatometry studies were conducted to measure the relative densification of powders under cold sintering as a function of time. This was performed using an Enerpac system hydraulic press with attached digital contact sensor Keyence GT2-H32. A uniaxial pressure of 250 MPa was applied at $t = 0$, and the linear displacement of the sample was measured with a resolution of 0.5

µm every 1 second interval. The height shrinkage of the pellet was defined by Equation 5.1, as previously described in Section *5.2.3 Dilatometry study* of this dissertation.[45, 84]

6.2.2 Characterization

The powder particle size distribution of cold sintered NMO-diamond composites was determined by analyzing images from a Field Emission Scanning Electron Microscope (SEM, Thermo Fisher FESEM Verios G4) at 10,000X magnification. Relative densities were determined by dividing the measured geometrical density of the pellets by their theoretical density (ρ_{NMO} = 3.682 g/cm^3, ρ_{diamond} = 3.547 g/cm^3).

For the characterization of the dielectric properties, the pellets underwent polishing with 1200/P4000 sandpaper and ethanol. Dielectric measurements (ε_r, $\tan\delta$) at low frequency of 10^6 Hz were conducted on pellets with a diameter of 13 mm and a thickness of ~2 mm using a precision LCR meter (Keysight E4980A). High-frequency dielectric measurements of relative permittivity (ε_r) and dielectric loss ($\tan\delta$), at resonance frequencies (f_{res}) between 9 – 13 GHz were measured on pellets with a diameter of 13 mm and a thickness of ~6 mm, utilizing the Hakki-Coleman dielectric resonator method [126] with a Network Analyzer (Keysight P9374A).

To determine electrical breakdown strength, 13 mm diameter pellets were polished to reduce their thickness from 2 mm to 0.4 mm. The test was conducted applying a DC voltage gradually increasing at a rate of 500 V/s until the electrical breakdown failure occurred on the sample, in reference to the IEEE Std 930™-2004 Guide for the Statistical Analysis of Electrical Insulation Breakdown Data.

The temperature coefficient of resonance frequency was determined across a range of 20 – 80°C using the Cavity resonance method, with measurements taken by a Network Analyzer (Keysight P9374A). Thermal conductivity was assessed through the Transient Plane Source (TPS) method and calculated using the formula $\kappa=\alpha\rho C_p$, where density (ρ), heat capacity (C_p), and thermal diffusivity (α) were determined for each sample. Thermal diffusivity (α) was measured using a laser flash system (LFA-467 HT HyperFlash®, Germany), while specific heat (C_p) was determined by differential scanning calorimetry (Netzsch DSC 214, Germany). The uncertainty in thermal conductivity was estimated to be ±2%.

Analysis of the NMO-diamond interfaces was performed using High-Resolution Transmission Electron Microscopy (TEM Talos F200X) and Energy Dispersive Spectroscopy (EDS) mapping.

An ultrasonic immersion system was used to perform measurements (Mistras Group, Princeton Juction, NJ, USA). UTwin software (Mistras) was used to control the gantry as well as view data during the experiment. A JSR pulse receiver (Imaginant) was used to control the transducer’s gain and pulse repetition frequency during testing. An Olympus20 MHz center frequency transducer (element diameter = 6.35 mm, focal length = 50.8 mm) with a pulse-echo setup, was used to produce attenuation maps showing the homogeneity of ultrasonic scans, where one transducer both transmits and receives the signal. The probe was calibrated to be at normal incidence from the top surface of the sample, and the transducer produced only longitudinally polarized waves. The beam width of the transducer is calculated at 0.4 mm, which correlates to a circular spot size of 0.128 mm^2. The transducer was rastered across the sample focused on the back surface, scanning at 0.25mm resolution. The amplitude data was then averaged 10 times at each point at a 1000 MHz sampling rate. Ethylene glycol $(CH_2OH)_2$ was used as an immersion liquid.

This measurement technique relies on a low-attenuation reference sample, in this case, a fused silica cylinder, (ρ=2.214 kg/m^3, c_{silica}=6000 m/s). The attenuation of the silica is assumed to be zero. Since multiple sample thicknesses were tested, silica disks of either 1.5875 mm, 3.175 mm, or 6.35 mm were used based on the thickness of each sample. If the same transducer is used for both the sample and reference, then the attenuation and the wave speed can be determined along with contrast images associated with the inhomogeneities. Details of the non-destructive evaluation (NDE) method used on cold sintered NMO samples have been comprehensively described by Jones et al. [151]

6.3 Results and discussion

6.3.1 Cold sintering and microstructural development

The diamond filler particles were mixed with the NMO powder and with 25 wt.% of deionized water, then after approximately 5 minutes of manual mixing using an agate mortar and pestle, the mixed powder is poured into the stainless steel die. A pressure of 250 MPa was applied at room temperature and the system was heated up to temperatures between 180°C and 220°C and held for 120 mins. A dilatometry study qualitatively describes the densification development during the cold sintering process. Figure 6-2 shows the differences between the densification curves for the NMO ceramic versus composites with high filler content (40 vol.% of diamond). By increasing the temperature in the cold sintering of the composite, high densities can be obtained and this is found to be at temperatures between 200°C to 220°C with a 250 MPa pressure and a hold of 2 hours.

It was also identified that the rearrangement densification is limited with diamond fillers in the first ten minutes relative to an earlier study with hexagonal boron nitride [45]. With the diamond the final densification stage is not completed until the second hour of the densification, so the major densification from compaction to final densities are through the cold sintering process, via the pressure solution creep process in this composite system. The diamond act as an inert phase to the cold sintering with the water as a transient phase, being an obstacle to the $Na_2Mo_2O_7$ densification.

Therefore, longer times are required to transport the species around the diamond fillers, in the transition of density from 85 to 93%, and higher temperatures aid the densification process as well.

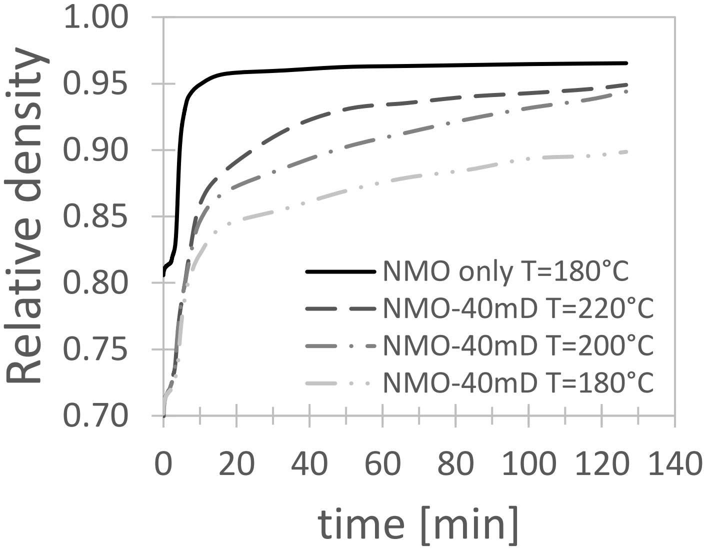

Figure **6-2**: Densification curve of NMO and NMO-40 vol.% diamond composites for held temperatures between 180°C and 220°C.

A series of ceramic composite materials were processed with different volume fractions of diamond fillers with 0, 10, 20 ,30 and 40 volume %. Figure 6-3 shows the variation of the final densities with the composites after the cold sintering process. All the samples have closed porosity with densities above 93% of theoretical density, but there is a systematic decrease of the density with increasing volume fraction of diamond fillers. The theoretical density of the composites was estimated from the following mixing law:

$$\rho = f_1\rho_1 + f_2\rho_2 \qquad \text{(Eq. 6.1)}$$

where f_1 is the NMO volume fraction with a density ρ_1 of 3.682 g/cm^3 , and f_2 is the volume fraction of diamond filler with a density r_2 of 3.547 g/cm^3, and f_1+f_2=1.0. The densities of the composites are determined with a geometric method of ratioing the mass with the physical volume of the cylindrical pellets.

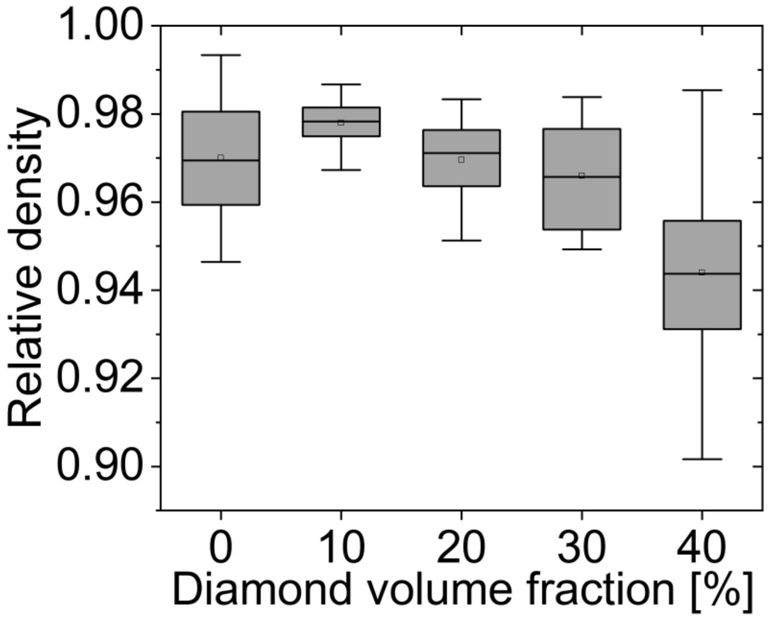

Figure **6-3**: Densification as function of filler volume fraction of NMO composites.

The microstructure of the composites was determined through SEM and an EDS method to locate the diamond, through the carbon x-ray signals. Figure 6-4 shows the images of the composites for 0 to 40 vol.% of filler. It is observable that the diamond is homogeneously dispersed throughout the microstructure, and the grain sizes of the materials are also uniform and relate to the sizes of either the initial powder of the diamond, and the grain size of the $Na_2Mo_2O_7$ relates to the sizes of the single phase $Na_2Mo_2O_7$.

Using both TEM diffraction contrast and lattice imaging it can be seen that interfaces between the diamond and the NMO are clean and in good contact with each other. SEM images also demonstrate that diamond can penetrate the NMO grains, as schematically demonstrated in Figure 6-5.

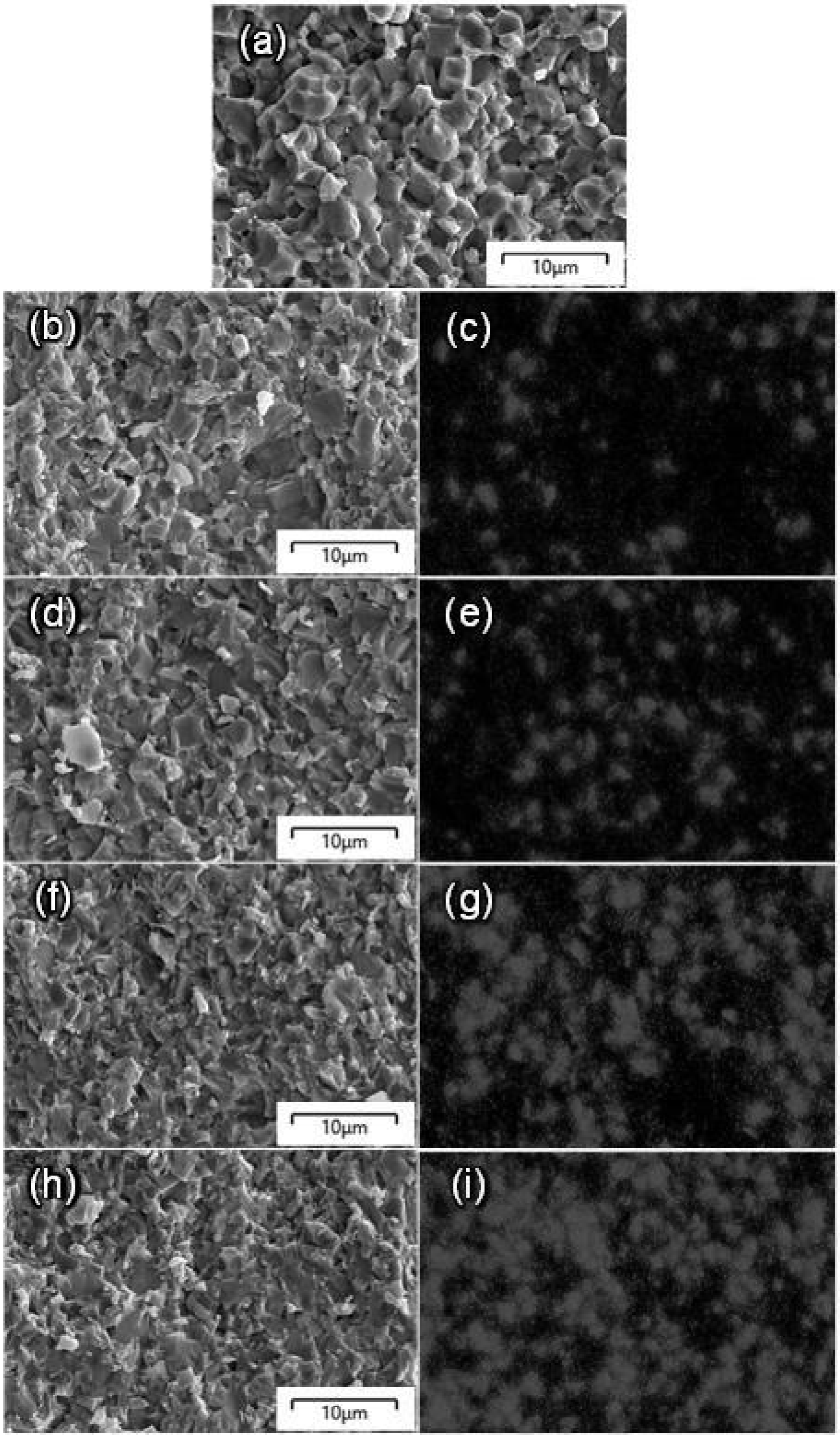

Figure **6-4**: SEM images of microstructures and EDS mapping showing the presence diamond (Carbon element indicated with red) in cold sintered (a) NMO and NMO-diamond composites with (b,c) 10 vol.%, (d,e) 20 vol.%, (f,g) 30 vol.%, and (h,i) 40 vol.% of filler.

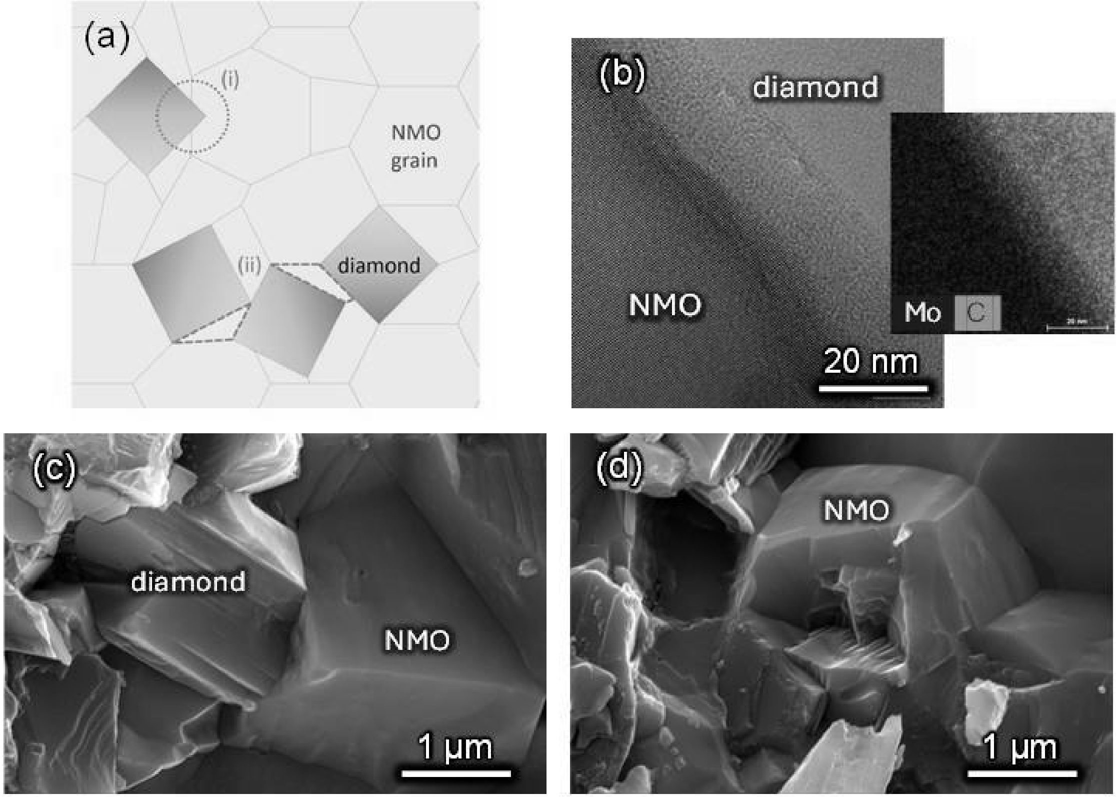

Figure **6-5**: (a) Schematic of features present in microstructure of cold sintered NMO-diamond composites. The light blue circle (i) indicates the condition of diamond particle piercing into a NMO grain. The purple regions mark (ii) NMO grain creep deformation caused by pressure from adjacent diamond particles. (b) STEM-EDS mapping of diamond and NMO presence. SEM images show evidence of (c) puncture of diamond particle into a NMO grain, and (d) indentation mark left of a diamond particle on a NMO grain.

6.3.2 Non destructive evaluation (NDE)

To be sure that there are no macroscopic flaws in the cold sintering conditions, an ultrasonic non-destructive evaluation (NDE) method was used, as a metrology approach to ensure high quality in the cold sintered components. A comprehensive description of the method utilized in this study has been provided by Wheatley.[152] This method uses the longitudinal attenuation and wave speed to characterize sodium molybdate (NMO) materials. The macroscopic inhomogeneity such as pores or microcracks that can occur, or be created, like stress gradients from wedge in the pushers, can be detected with NDE. Figure 6-6 shows NDE images of pure NMO and the composite NMO-40 vol.% diamond samples. The wider distribution of longitudinal modulus in the composite sample would be likely attributed to a density gradient within the sample. Despite the range of longitudinal modulus measured within the samples, it is reasonable to conclude from the NDE mapping that the material is free of fractures, voids or other processing defects.

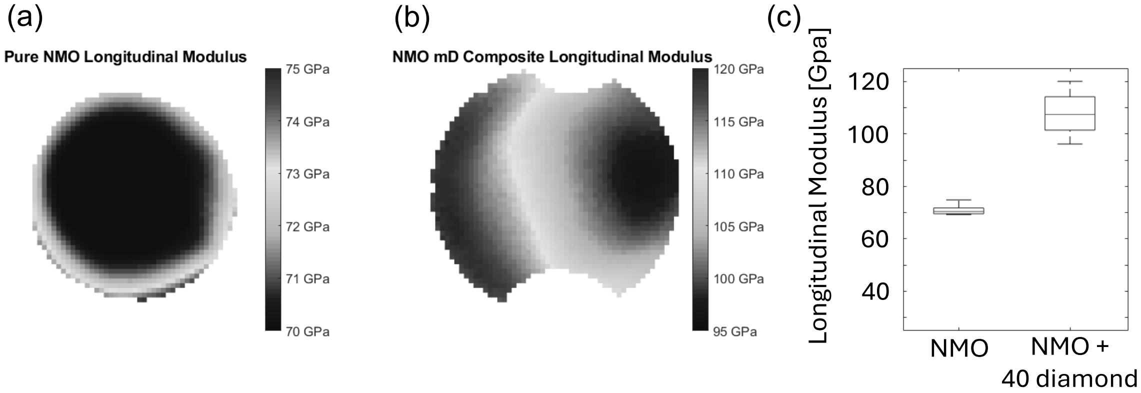

Figure **6-6**: Homogeneous images of NDE by ultrasonic immersion analysis of (a) NMO and (b) NMO-40 vol.% diamond samples. (c) Comparison of the average longitudinal moduli between the pure NMO and 40% diamond-NMO composite.

6.3.3 Electrical characterization

The complex permittivity was characterized in terms of the relative permittivity and the dielectric loss. This was done for low frequencies through making a parallel plate capacitor, of geometrically known area and thickness, to determine the relative permittivity and record the dielectric loss in the form of the *tan δ*, over a temperature range from 20°C to 100°C at an AC frequency of 10^6 Hz. The data is given in Figure 6-7 for composites with the diamond filler having a volume fraction between 0 to 0.4. The room temperature relative permittivity decreases with the diamond filler and changes between 12 to 9, likewise the room temperature *tan δ* changes from 2×10^{-4} to 0.003.

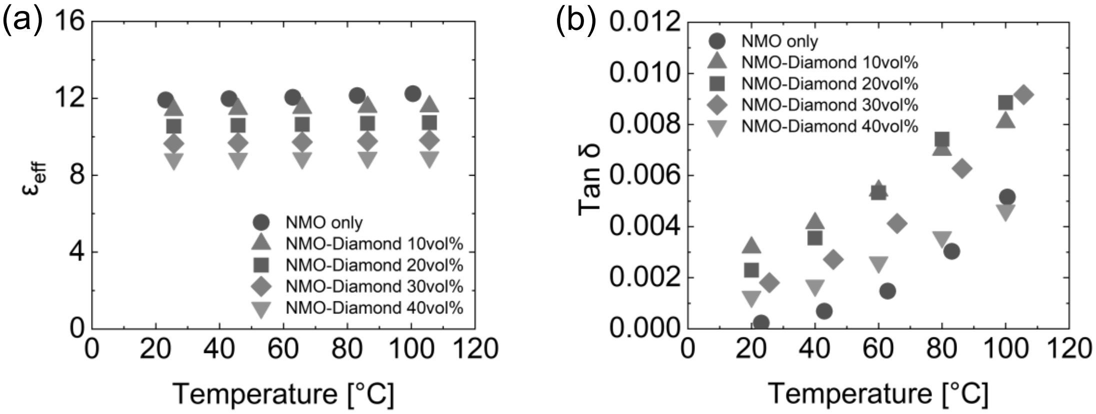

Figure **6-7**: Dielectric properties of (a) relative permittivity and (b) dielectric loss of NMO-diamond cold sintered composites at a frequency of 10^6 Hz.

As these types of composites will be of greater importance for higher frequency applications, the dielectric properties were also characterized in the microwave range, using the Hakki-Coleman technique. Here the room temperature relative permittivity ranged from 13 to 9, and the *tan δ* from 3×10^{-4} to $1.5\text{x}10^{-3}$. Figure 6-8 shows the relative permittivity at room temperature varying with volume fraction of diamond and the $Q\times f$ factor. The $Q\sim\Delta f/f_0$ and $\tan\delta\sim1/Q$. The Δf is the frequencies at 3db down from the resonance signal. At room temperature, $Q\times f$ ranges from 22,000 down to 6,000 with the 0.4 volume fraction diamond in NMO. The relative permittivity closely follows the trend as given from the logarithmic mixing law.

Heating the sample in a resonance cavity and monitoring the frequency change with temperature allows to determine the temperature coefficient of frequency (TCF) given by Equation 5.8, as previously described in Section *5.3.6 Temperature coefficient of resonance frequency* of this dissertation.

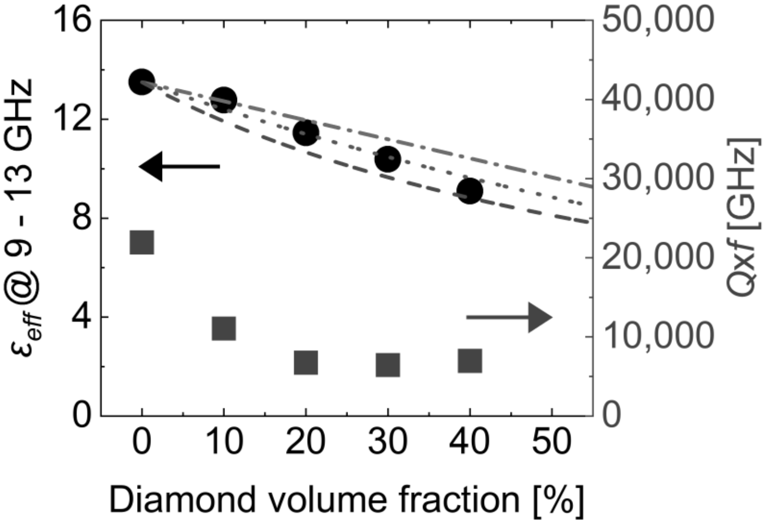

Figure **6-8**: The variation of effective relative permittivity for NMO-diamond composites at room temperature for microwave frequencies between 9 – 13 GHz, fitting within the boundary parameters of a logarithmic mixing law.

The plot in Figure 6-9 illustrates that NMO exhibited a TCF = -43 ppm/°C, while NMO-diamond composites varied their TCF_{eff} values between ranges of -37 to -16 ppm/°C, for temperatures from 20°C to 80°C. The linear regression of these values was calculated by the least squares method, for a standard error of the estimate = 0.9 ppm/°C. With the addition of diamond volume fraction, the TCF_{eff} values become closer to zero. This is a desired feature in materials for microwave substrate applications, minimizing the shift of resonance frequency as function of temperature for the operation conditions, preventing the necessity of additional circuitry adjustments.

The dielectric breakdown strength of the NMO-40 vol.% diamond composite, relative to the pure NMO ceramic was also studied. The data were collected on many samples with the same dimensions at an increasing rate of 500 V/s for the applied field. The data plotted on in Figure 6-10 shows that Weibull analysis revealed an improvement in both the breakdown strength (E_b) and the shape parameter (β) with increased diamond content, indicating a narrower breakdown voltage range.

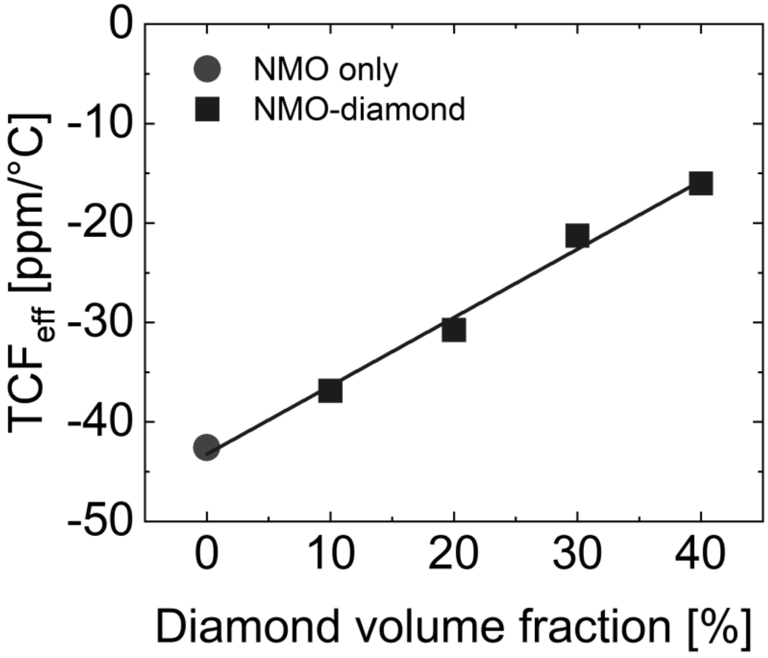

Figure **6-9**: The effective temperature coefficient of resonance frequency (*TCF$_{eff}$*) becomes closer to zero with the addition of filler volume fraction in NMO-diamond composites, within the temperature range of 20°C – 80°C.

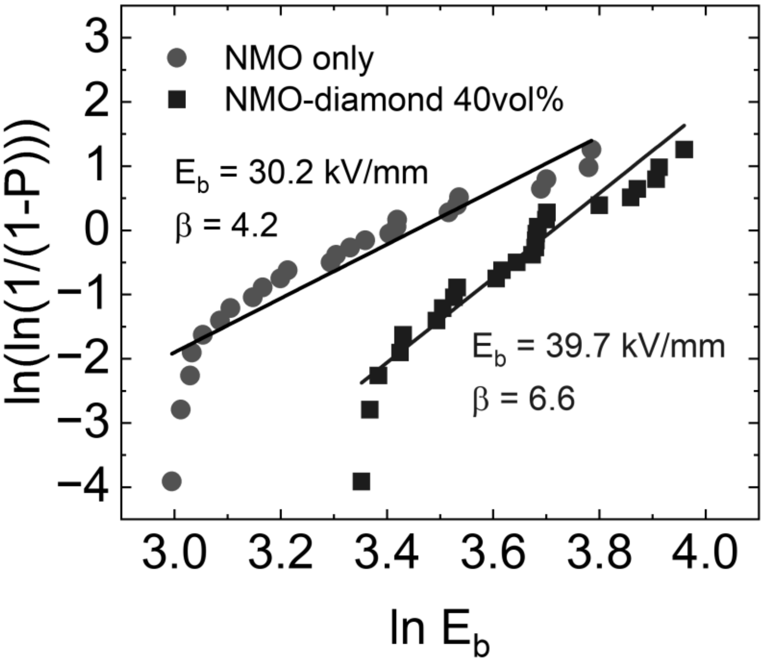

Figure **6-10**: Weibull statistical analysis and of electrical breakdown strength for NMO and NMO-40 vol.% diamond composite.

6.3.4 Thermal characterization of the composites

An important design aspect in these composites is to maintain high performance dielectric properties for the dielectric substrates and increase of thermal conductivity. In this study, the thermal conductivity was determined form a series of properties and calculated by Equation 5.9, as described in Section *5.3.7 Thermal conductivity* of this dissertation.

The trend follows a logarithmic dependence over the 0 to 0.4 filler volume fractions of the diamond with a 3.5X increase in thermal diffusivity. The improvement in thermal conductivity (κ) from the LFA/DSC calculation ranged from 1.7 W m^{-1} K^{-1} for pure NMO, to 4.9 W m^{-1} K^{-1} for 40 vol% of diamond at room temperature. The non-linear improvement of thermal conductivity fits closely to the n=0 logarithmic mixing law [131, 132] for $\kappa_{diamond\ eff}$ = 25 W m^{-1} K^{-1}, as shown in Figure 6-11. With the data following a systematic trend, the results did not show the increase in the thermal conductivity expected from the diamond's intrinsic properties. This means that the thermal conductivity is likely being dominated from phonon scattering at interfaces in the composite.

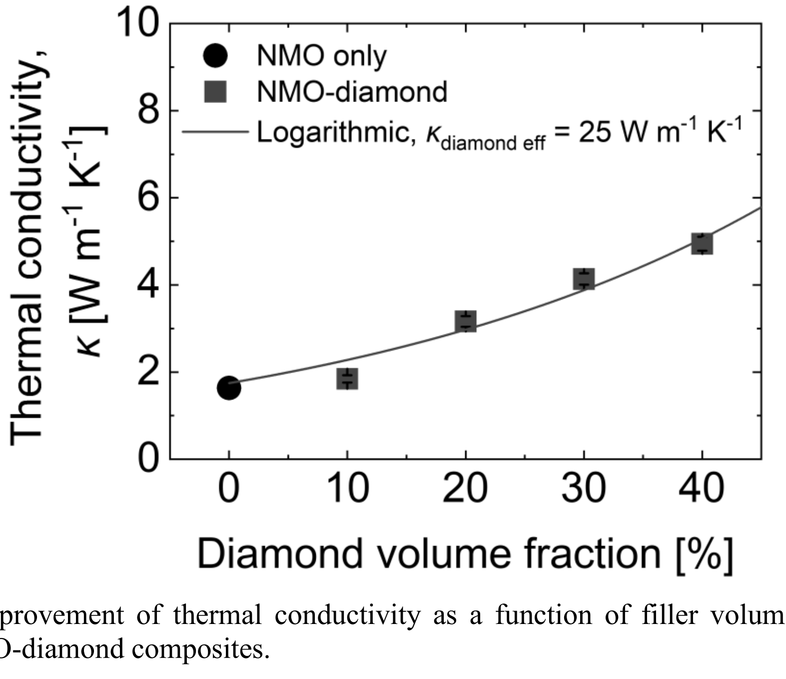

Figure **6-11**: Improvement of thermal conductivity as a function of filler volume fraction was evident for NMO-diamond composites.

6.4 Summary and conclusions

Sodium molybdate powder was synthesized and cold sintering was used to fabricate composite samples of NMO-diamond at filler volume fractions between 0-0.4. The average relative densities were between 94-98% for NMO and the composite samples. The dilatometry study results indicate that the diamond filler play a limiting role to the densification of the cold sintered composites. EDS mapping of composite microstructures show an homogeneous and systematic distribution of diamond with increasing filler volume fraction. SEM microscopy revealed the indentation of diamond particles into the NMO matrix grains due to the applied pressure, this evidence connects microstructural features with the results from densification dilatometry.

The ultrasonic NDE revealed cold sintered pellets free of processing flaws, while providing representative values of longitudinal modulus for the NMO and NMO-diamond composites.

The dielectric properties of the composites were measured at low frequencies of 10^6 Hz, and at high frequencies of 9 – 13 GHz. For both cases the relative permittivity of the composites fit within the limits of the Lichtenecker general mixing law for filler volume fractions between 10 – 40 vol.%, and their dielectric loss is low enough to meet the required values for microwave substrates applications. The Q×f values of the composites were reported within the range of 22,000 – 6,000 GHz.

The temperature coefficient of resonance frequency was determined for the pure NMO and NMO-diamond composites, indicating closer measurements to the desired value of zero with the increase of filler volume fraction.

The electrical breakdown strength also improved with increments of diamond in the composite, and not only the insulation breakdown increased, but the shape parameter (β) exhibited higher values compared to the pure NMO material, indicating a reduction in the range of the breakdown voltage with the increase of filler volume fraction.

The thermal conductivity was calculated by measuring the density, specific heat capacity and thermal diffusivity of the samples, showing an increase from NMO at 1.7 W m^{-1} K^{-1} to 4.9 W m^{-1} K^{-1} for NMO-diamond composite with 40 vol% of filler. The dielectric and thermal properties analyzed for the NMO-diamond cold sintered composites, indicate it to be an adequate innovative material for microwave substrate applications.

Chapter 7

Multiple Creep Mechanisms Driving Densification of Composites Undergoing Cold Sintering

This study considers the densification of a scheelite structured $Na_2Mo_2O_7$ (NMO) ceramic matrix phase that can be cold sintered using a transient liquid of water. This NMO material is cold sintered with composite filler materials of hexagonal boron nitride (hBN) and micro diamond (md) with volume fractions between 0 to 40 %. Both hBN and md perturb the densification of the NMO in the composites. Through the measurement of the shrinkage rates under both different heating rates under isothermal conditions, this study consider the kinetics and mechanisms controlling the densification. Heating rates for the cold sintering of the various composites between 2°C/min to 8°C/min were utilized, with the energetics of the maximum sintering rate being analyzed by the Woolfrey-Bannister method.[153] The sintering activation energy for the pure NMO is found to be ~82 kJ/mol. The sintering exponent, n~3.7 is determined to be consistent across all the NMO composites, with the intermediate sintering stage controlled by the pressure solution creep of the NMO matrix phase. Under the isothermal conditions at temperatures between 180 to 220°C and under applied compressive average stress between 100 to 350 MPa, there is a further densification process in the NMO and NMO-md composites, which is identified as a steady-state diffusion creep process, with stress exponents determined to be n~1 for the pure NMO, consistent with a Nabarro-Herring creep process, and n~2 for the NMO-md composites, suggesting a creep mechanism of interface sliding.[154] Densification and creep analysis is conducted and considered with supporting microstructural analysis. The creep process was found to be mostly related to the penetration of the md into the NMO matrix grains. The effective activation energy of the steady-state creep was ~36 kJ/mol for NMO and the composites with the md inclusions. The md penetration into the NMO is observed with a transmission electron microscopy.

7.1 Introduction

The densification of ceramic materials undergoing the cold sintering process has several stress driven mass transport processes that can enable the high densities at low temperatures. A major mechanism is the pressure solution creep,[155] which involves three serial processes that require the application of an applied pressure and a solution at the interfaces of the particles under the compressive stresses. These serial processes are dissolution, transport, and precipitation.[115] The driving force is a stress difference in chemical potential between the enhanced stresses at the particle-particle contact points that undergo dissolution, and the low stressed pore regions where the precipitation takes place. The natural pressure solution process is a well-known process that drives densification in geological rock formations of minerals, such as ductile behavior of the upper crust with sedimentary rock formation as one example.[31] Geological pressure solution creep processes are slow and can take 100,000 years or more, this is due to relative large particles and water solutions that may not have the suitable pH or temperatures to drive the respective transport processes at high rates.[156]

Sintering is intended to effectively produce much faster rates that will ultimately be of interest to large scale manufacturing processes. The rates can be increased with some of the following strategies: using smaller particle sizes, higher temperatures and transient phases that drive higher rates of dissolution and precipitation. Through these strategies many ceramics and metals have been successfully densified.[26, 82, 114, 117, 119] These materials have not only been densified, but they have also been shown to have properties that are like materials that are sintered at temperatures a few hundreds degrees higher than the cold sintered cases. In addition to the cold sintering of monolithic materials, there has been demonstrated the ability to fabricate composites and multilayer devices with unique properties.[157–160]

There have been a few studies on the kinetics of cold sintering densification, and there is very good evidence that this is through a pressure solution process, as summarized in papers by Bang et al, Ndayishimiye et al, and Villatte et al.[30, 83, 84, 114, 161] Currently there has been no investigation on the quantification of the densification kinetics with the cold sintering of composites. It is the purpose of this study to consider the impact of fillers on the kinetics of the densification in a material that can undergo cold sintering and incorporate filler materials. Here a model system of a scheelite structured, $Na_2Mo_2O_7$ (NMO) was used as the matrix ceramic.[142, 162] NMO has a relatively low melting point with $T_m \sim 632^{o}C$ and therefore in addition to the pressure solution creep, other creep processes could be anticipated with the material subjected to an applied stress at temperatures around 0.4 T_m. As communicated in previous publications, NMO is a ceramic that can undergo cold sintering with a transient liquid phase of water.[90, 123, 124] This material can also be fabricated into composites with fillers of both hexagonal boron nitride (hBN) and micro-diamond (md), these are of interest for dielectric substrates with higher thermal conductivity, and other enhanced dielectric properties such as resistivity, dielectric breakdown strength, and smaller temperature dependences of permittivity, as discussed by Mena-Garcia et al. [46]

7.2 Experimental methods

7.2.1 Powder preparation

The synthesis of NMO powder was conducted as documented in Section *5.2.1 Powder preparation* of this dissertation. The NMO powder was homogeneously mixed with hBN (99.8%, 70-80 nm, Nanoshel) and microsized diamond (md, natural, 1-3 μm, MANT USA Inc.) according to the intended filler volume fractions.

7.2.2 Cold sintering process

For the fabrication of each pellet, the NMO matrix and filler powders were weighed for every sample considering the intended filler volume fraction. These weighed powders were combined in a glass vial and mixed using a planetary centrifugal mixer (Thinky, AR-250) for 10 cycles, each lasting 1 minute. Following centrifugal mixing, 25 wt.% of deionized water was added to the evenly mixed powder using a pipette. Subsequently, the powder and the transient chemistry, H_2O, were manually mixed in an agate mortar with a pestle for approximately 10 minutes until achieving a homogeneous appearance. The moistened powder was then transferred to a stainless steel die for cold sintering. Uniaxial pressures (σ) between 100 and 350 MPa were applied at room temperature using an Enerpac system hydraulic press with attached digital contact sensor Keyence GT2-H32, then the assembly was heated up at rates between 2 and 8°C to temperatures between 180 and 220°C for 2 hours using a heating jacket wrapped around the die, controlled by a PID loop feedback mechanism. A thermocouple was positioned in the lower piston of the die to monitor the temperature. After the dwell time, the pellet was ejected from the die and left to cool down to room temperature under ambient conditions. Finally, the cold-sintered pellets were dried out in air at 200°C for 12 hours.

Dilatometry studies of the cold sintered samples were conducted to measure the relative densification of powders under cold sintering as a function of time. The shrinkage was measured using an Enerpac system hydraulic press with attached digital contact sensor Keyence GT2-H32. The uniaxial pressure was applied at $t = 0$, and the linear displacement of the sample was measured with a resolution of 0.5 μm every 1 second. The height shrinkage of the pellet sample was defined as previously described by the (Eq. 5.1).[45, 84]

7.2.3 Characterization

The crystal structure of the synthesized powder was characterized by X-ray diffraction (XRD) analysis using a PANalytical Empyrean system operated at 45 kV and 40 mA with Cu Kα radiation. The NMO particle size distribution was obtained by processing 10,000 X Scanning Electron Microscopy (SEM) images acquired using a Field Emission Thermo Fisher FESEM Verios G4 microscope. Relative densities were calculated by dividing the measured geometrical density of the pellets by their theoretical density ($\rho_{NMO} = 3.682$ g/cm^3, $\rho_{hBN} = 2.1$ g/cm^3, $\rho_{diamond} = 3.54$ g/cm^3). Details on the characterization of SEM and XRD analysis, are previously reported in Chapter 5 of this dissertation.

7.3 Results and discussion

7.3.1 Pressure solution creep analysis on NMO-hBN and NMO-md composites

Figure 7-1 shows the overall strain change and relative densification trends of the NMO, NMO-hBN, and NMO-md composites with various volume fractions of fillers. The heating rate is at 4°C/min from room temperature up to 200°C, under an applied compressive stress of 250 MPa to the powder in the die.

In Figure 7-1.a the relative strain is plotted as a modulus, the material is under a compressive uniaxially applied pressure in a die and there will be a radial stress from the walls of the die, then the powders will undergo a shrinkage. The strain is negative, but here is plotted as the modulus. Considering the NMO first it is noted that under compression there is first a rearrangement and then after 50°C there is a fast increase in the densification as the material undergoes sintering with the pressure solution mechanisms. With the hBN fillers there is a major densification that occurs with the particle rearrangement that is associated with the shearing of the layers with the hBN fillers. This occurs almost immediately in the sintering process and then further densification takes place with the pressure solution of the NMO phase. The densification rates are reduced with the md fillers, it can be noticed that under the isothermal hold at 200ºC there is further shrinkage, and the total amount of isothermal shrinkage is increased with the increase in the md volume fractions. Further experiments will later show this is associated with a diffusion creep process. There is negligible isothermal creep in the final densification of the hBN filler composites undergoing cold sintering. The relative densities are measured from geometric density measurements and estimated to the appropriate theoretical density from the method of mixtures equation (Eq. 7.1)

$$\rho = \Sigma f_i \rho_i \qquad \text{(Eq. 7.1)}$$

where f_i is the volume fraction of the i^{th} phase, and ρ_i is the density of the i^{th} phase, using the densities of the NMO, hBN and md, as 3.68 g/cm^3, 2.10 g/cm^3 and 3.54 g/cm^3 respectively. A more detailed analysis of the different densification behaviors is shown below, where the pressure solution densification was first considered, and later diffusional creep under isothermal conditions.

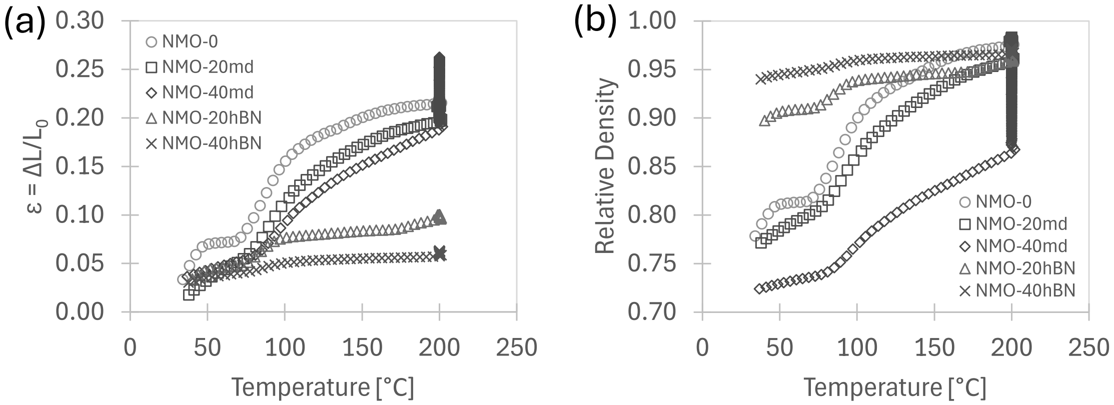

Figure **7-1**: (a) Modulus of the shrinkage strain of NMO-md with 20 and 40 vol.% filler, NMO ceramic and NMO-hBN with 20 and 40 vol% fillers, b) is the equivalent representation with relative density under a pressure of 250 MPa, with a heating rate of 4°C/min, up to an isothermal hold at 200°C.

Under the different heating rates the Woolfrey- Bannister method [84, 153] can be used to monitor the densification rates

$$\frac{d(\Delta L/L_0)}{dt} = K_0 exp\left(-\frac{Q}{RT}\right)\left(\frac{L_0}{L}\right)^{-n} \quad \text{(Eq. 7.2)}$$

Which after further mathematical simplification, is often used in the form of

$$T^2\frac{d(\Delta L/L_0)}{dt} = \left(\frac{\alpha Q}{(n+1)R}\right)\left(\frac{\Delta L}{L_0}\right) \quad \text{(Eq. 7.3)}$$

where α is the heating rate, Q is the effective activation energy of the sintering process, n is the sintering exponent, K_o is a constant, and R is the universal gas constant, and T is the temperature in Kelvin. The n is often related to the rate controlling sintering mechanism.

A series of plots are obtained for the cold sintering densification, and using constant heating rates between 2 and 8 °C/min, the shrinkage kinetics were analyzed to determine the effective activation energy, Q, and the sintering exponent, n, for the various composites with 20 and 40 vol.% of the hBN and md fillers. These plots are found in the supplemental section Figure 7-S1. The important parameters are all compared in Table 7-1, and their calculated errors were determined by the least square fit method.

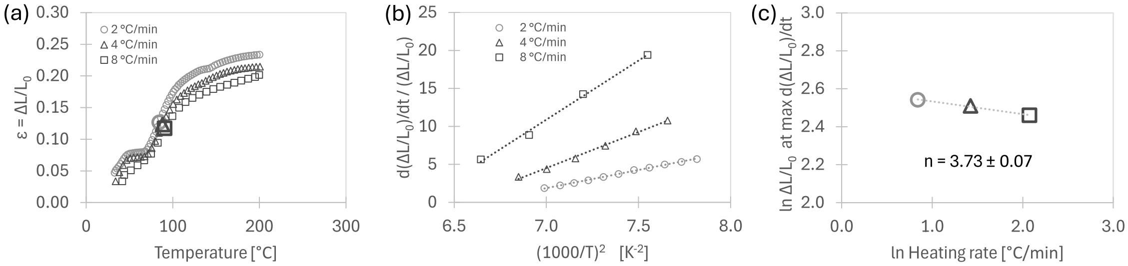

Figure **7-2**: (a) NMO ceramics undergoing cold sintering at different heating rates, 2, 4 and 8°C/min, with the corresponding strain under an applied stress of 250 MPa, (b) shrinkage strain rate versus inverse squared temperature, and (c) natural log-log plot of the strain at maximum strain rate versus heating rate.

Table **7-1**: Average activation energies *Q* and *n* sintering exponent for NMO, NMO-hBN and NMO-md composites.

Composite	Q [kJ/mol]	$\pm \Delta Q$ [kJ/mol]	n [-]	$\pm \Delta n$ [-]
NMO	82	4	3.7	0.07
NMO-20 md	97	7	3.6	0.08
NMO-40 md	62	5	3.5	0.02
NMO-20 hBN	71	6	3.6	0.16
NMO-40 hBN	48	7	3.7	0.08

There is very good correspondence between the different sintering exponents, *n*, that points to the fact that it is the same basic sintering mechanism that controls the sintering in all cases. Within the error, these are statistically equivalent. Similarity in the mechanism is not surprising as the enabling cold sintering phase is the NMO material. The magnitude of the *n* as a sintering exponent is *n*>2, and therefore the mechanism is either through a grain boundary diffusion and/or an interfacial controlled liquid phase[154] sintering process that would be consistent with a

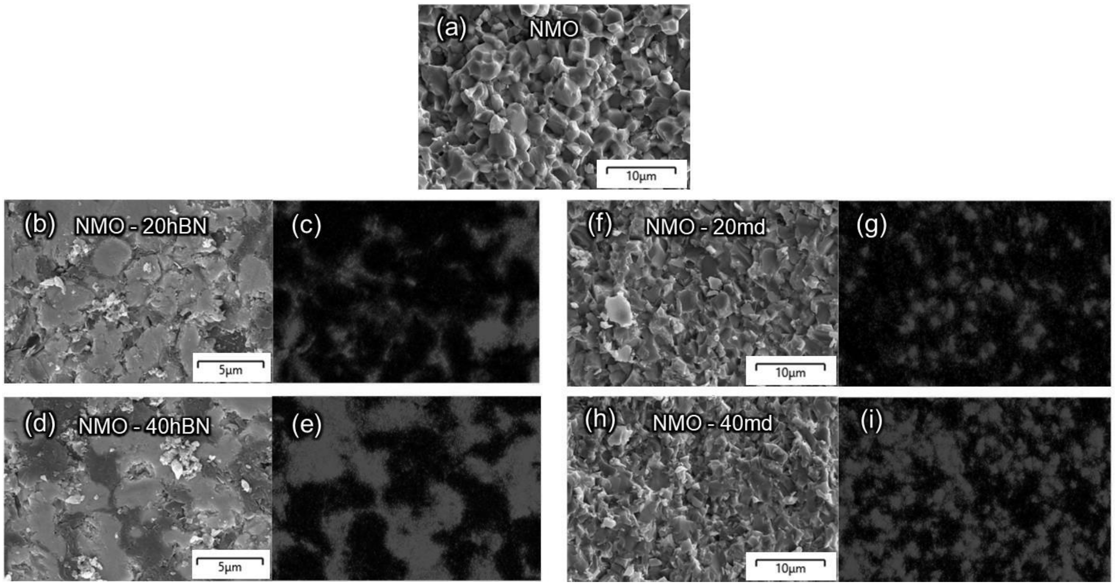

Figure **7-3**: Microstructural evolution of composites with increase of filler volume fraction towards percolation, from (a) pure NMO to the composites exhibiting (b,c) 20 vol.% hBN, (c,d) 40 vol.% hBN, (f,g) 20 vol.% md, and (h,i) 40 vol.% md.

pressure solution creep mechanism.[154, 163, 164] The activation energies are low relative to conventional sintering energies, as to also be expected with pressure solution creep.[82, 114] There is more variation in the effective activation energy from each composite, relative to the pure NMO. All the composites that would have a filler content above the percolation limit have a smaller activation energies than the NMO. In Chapter 5 it has been described how the hBN shears under pressure, causing a low percolation limit of ~ 2 vol.%.[46] The md will not exceed the percolation until volume fractions are above 0.3. It is known that particle packing and different powders even with similar sizes can give relative large scatter in the activation energies of a sintering process, and so this may also be impacting the observed activation energies. Experimentally, the cold sintering methodology was executed carefully and the errors were noted with multiple measures, showing there is good consistency within each constant rate determination, as the important data is considered with the errors from a least square analysis. The microstructure evolution of selective composites is shown in Figure 7-3.

7.3.2 Isothermal steady-state creep in the NMO-md composites

At the temperatures of the cold sintering process, the water is evaporated from the NMO ceramic and the composites. At 200°C, the ceramic material experiences the additional densification that is pointed out in Figure 7-1 under the isothermal holds. Under these conditions in the dilatometer system, the samples are subjected to a constant applied stress, and therefore can have diffusional creep processes contributing to the final stages of the densification, after the non-isothermal heating studies.

For an open system, there can be three main stages that could control creep under these isobaric and isothermal conditions, which can be a primary creep rate where the strain rate can vary with time, there can be a secondary creep rate that has a constant strain rate, and finally a tertiary creep rate when the creep rate increases exponentially with time. In this study, the tested samples were radially confined by the inner walls of the die used for cold sintering, not allowing to see clearly the three stages described above. Therefore, this analysis considers data corresponding to the early isobaric and isothermal conditions, at which the densification exhibits a constant strain rate, characteristic of steady-state creep. Figure 7-4 shows the early constant strain rate as a function of time, in the isobaric and isothermal conditions for the analysis of steady-state creep. This being the case, Norton's general steady-state creep equation can be used, which is given by

$$\frac{d\varepsilon}{dt} = A\sigma^{n} exp\left(-\frac{Q}{RT}\right) \qquad \text{(Eq. 7.4)}$$

where *dε/dt* is the strain rate under isothermal and constant stress conditions, *A* is a proportionality constant, *Q* is the effective diffusion constant controlling the creep process, *n* is a stress exponent that depends on the creep mechanism, *R* is the universal gas constant, and *T* the absolute temperature.[165]

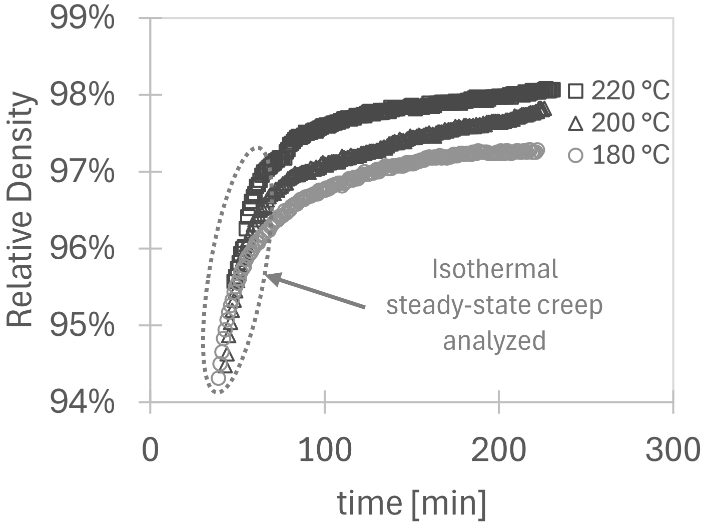

Figure **7-4**: Pure NMO samples at isobaric (σ=125 MPa) and isothermal (T=180, 200 or 220°C) experimental conditions, showing the constant strain rate corresponding to the steady-state creep process analyzed in this study.

Figure 7-5.a shows the respective temperature dependence of the NMO-md composites undergoing steady-state creep in the early stages of sintering under the isothermal holds. Figure 7-1 showed that the higher the volume fraction of md, the larger amount of isothermal shrinkage is required to obtain the higher densities in these NMO-md composites. In terms of the creep exponent, Figure 7-5.b shows an exponent *n*~1 for pure NMO, which would be consistent with a diffusional transport of a vacancy flux towards the high stress, and mass transport of atomic fluxes to the low stress and tensile regions. This is known as either Nabarro-Herring creep with diffusion in the bulk grains or Coble creep along the grain boundaries in pure ceramic or metal systems.[155] For the case of the NMO-md composites, the microdiamond inclusions will apply local stresses within the NMO grains. This feature in the microstructural conditions is reflected in a change of the stress exponent to *n*~2, suggesting a shift to a creep mechanism of grain boundary sliding without the presence of a liquid phase.[166] Table 7-2 presents the experimental parameters and obtained values for thermal activation energy (*Q*), stress exponent (*n*) and *ln A* described in Eq. 7.4.

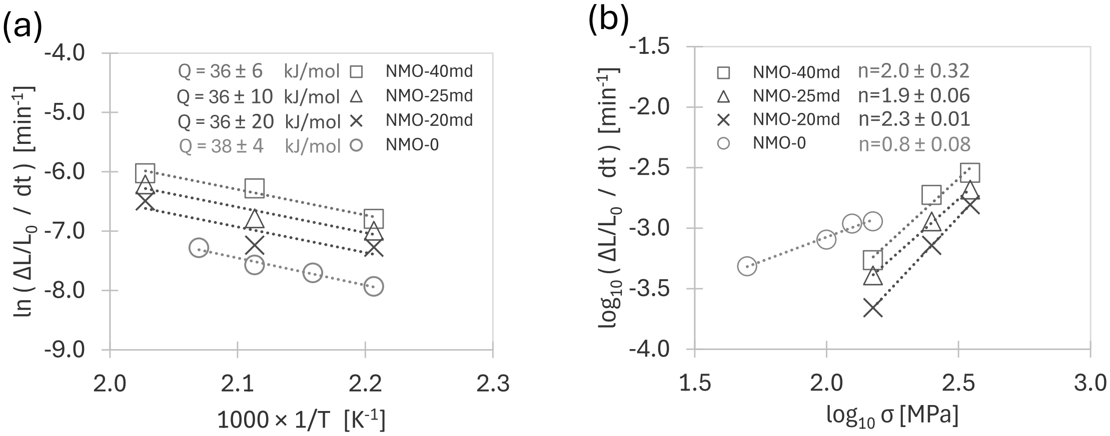

Figure **7-5**: (a) Isothermal steady state creep in the final stages under a stress (σ) of 250 MPa for NMO, and NMO-md composites, and between temperatures of 180 to 220°C, for composites with f = 0, 20, 25 and 40 md filler volume fractions, (b) A log-log plot to determine the stress exponent *n* at 200°C with stresses between 50 to 350 MPa.

Table **7-2**: Experimental parameters, and values obtained from the Norton's general steady-state creep equation (Eq. 7.4).

Sample	Stress σ [MPa]	Temperature [°C]	Activation energy Q [kJ mol^{-1}]	stress exponent n [-]	ln A [min^{-1} MPa^{-n}]
NMO - 0	250	180 - 210	38 ± 4	0.8 ± 0.08	-2.3 ± 1.5
NMO - 20md	250	180 - 220	36 ± 20	2.3 ± 0.01	-10.6 ± 5.1
NMO - 25md	250	180 - 220	36 ± 10	1.9 ± 0.06	-8.0 ± 3.0
NMO - 40md	250	180 - 220	36 ± 6	2.0 ± 0.32	-8.3 ± 3.3

From the transmission electron microscopy (TEM) investigation of the NMO-md composites, it was observed that there is penetration of the md into the NMO grains, with very few dislocations in these regions. It is therefore expected, the diffusion creep processes to be active to accommodate the grain penetration and the shape changes within the microstructure. Figure 7-6 shows the diamond interpenetration into the NMO grains, and a schematic diagram demonstrating the proposed steady state process. For the NMO material, to conformally allow the interpenetration of diamond particles there will be bulk, and grain boundary diffusion, but with $n\sim2$ for the stress exponent, there is likely a grain boundary sliding.

7.4 Summary and conclusions

This work points to the fact that multiple process can impact the densification of composites under cold sintering conditions. With the hBN fillers in NMO ceramics the initial densification at low temperatures is through the shear and particle rearrangement of the powders, which rapidly leads to relative densities >85%, and then on heating to higher temperatures the material undergoes a pressure solution creep process to obtain higher densities ~95% of theoretical density. The pure NMO and the NMO-md composites have only moderate rearrangement, and so, the major densification takes place during the heating ramp. After heating up at different rates, there is a temperature dwell in the sintering profile, thus for NMO and NMO-md composites there is an isothermal stage densification. This densification under isothermal conditions occurs after major loss of the liquid phase, so the pressure solution creep is suppressed, and the densification is then dominated by an additional diffusional steady-state creep process.

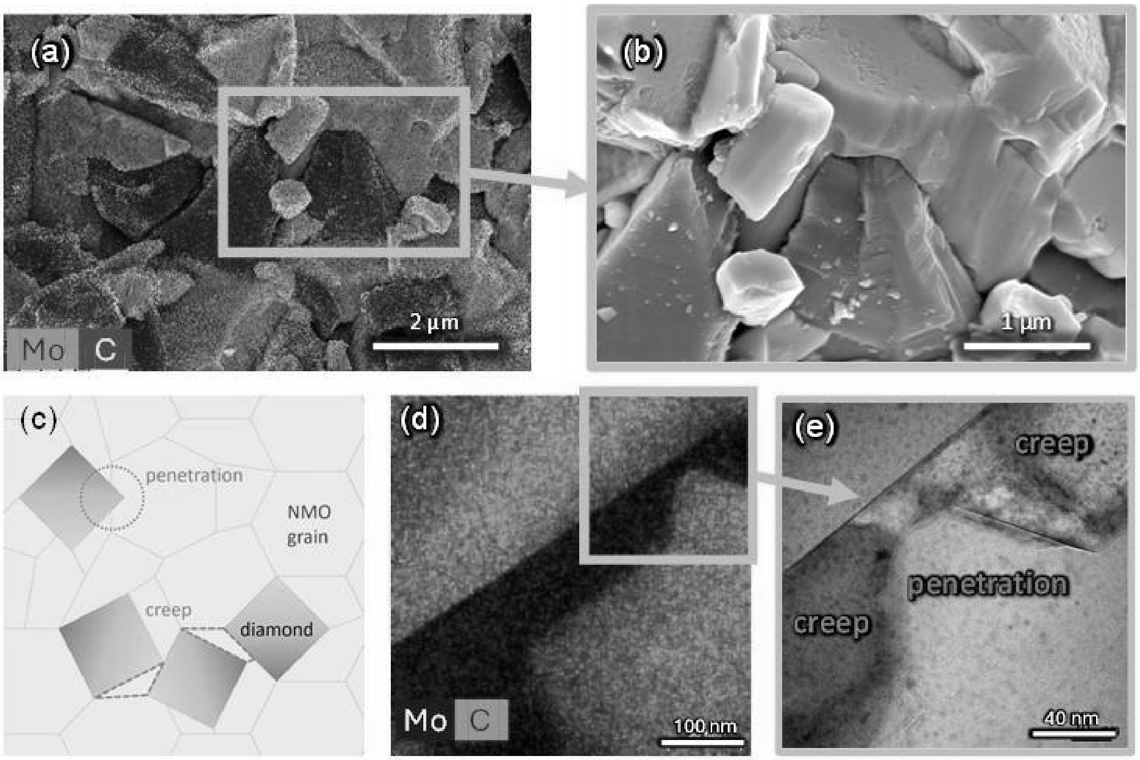

Figure **7-6**: (a) EDS mapping of NMO-40md composite showing presence of NMO (green) and diamond (red). (b) SEM image of diamond particle penetrating a NMO grain. (c) Proposed schematic of steady state creep showing penetration of diamond into NMO grain, and creep of NMO filling gaps among diamond particles. (d) EDS mapping of NMO (blue) and diamond (green) of the (e) TEM image showing the features of NMO creep and penetration of diamond particles.

7.5 Supplemental figures to Chapter 7

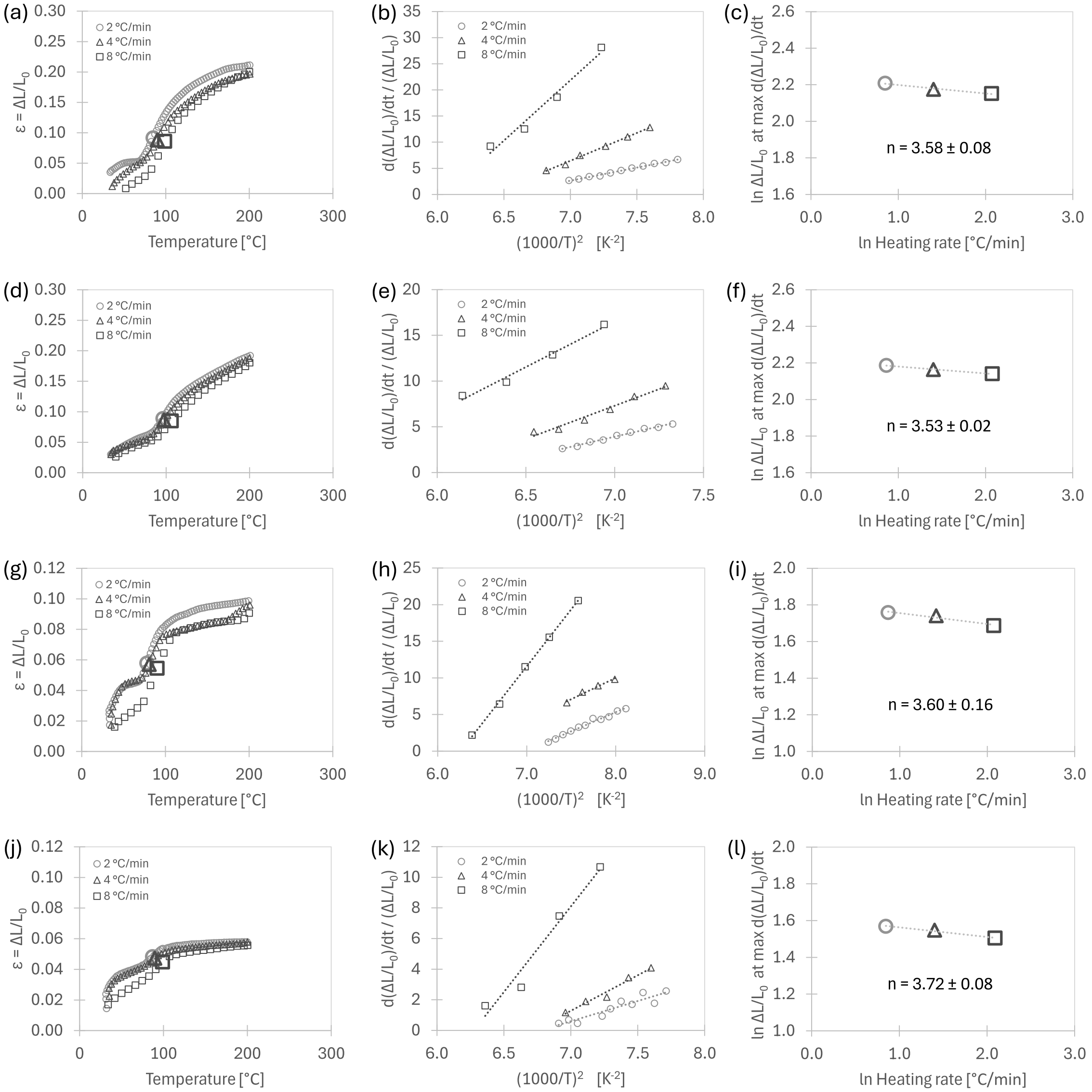

Figure **7-S1**: Composite ceramics undergoing cold sintering at different heating rates, 2, 4 and 8°C/min, with the corresponding strain under an applied stress of 250 MPa, shrinkage strain rate versus inverse squared temperature, and natural log-log plot of the strain at maximum strain rate versus heating rate, for (a-c) NMO-20md, (d-f) NMO-40md, (g-i) NMO-20hBN and (j-l) NMO-40hBN.

Chapter 8

Summary and Future Work

8.1 Summary

The investigation presented in this dissertation, recognizes the importance of the cold sintering process (CSP) as a transformative approach for ceramic composite fabrication, offering unique advantages over traditional sintering methods. This study undertakes a comprehensive investigation into the synthesis, characterization, and application of ceramic-polymer and ceramic matrix composites (CMCs) via CSP, drawing insights from studies outlined in Chapters 4, 5, 6, and 7.

Chapter 4 explores the fabrication of ZnO/PVDF-TrFE ceramic-polymer composites utilizing CSP. This chapter represents a significant advancement in understanding the interaction between ceramic and polymer phases in composite materials. By achieving high relative densities at remarkably low temperatures, this study demonstrates the efficacy of CSP in preserving the ferroelectric properties of PVDF-TrFE within the composites. Through TEM analysis, the thickness of the PVDF-TrFE phase at grain boundaries is quantified, providing valuable insights into the composite microstructure. Furthermore, analysis of experimental data allows to determine the conduction mechanisms across grain boundaries, revealing a non-ohmic behavior indicative of Schottky thermionic emission and Fowler-Nordheim tunneling. These findings underscore the potential of integrating functional polymers into ceramic matrices to modulate electrical properties, particularly for voltage dependent resistors applications, opening future opportunities for the development of advanced electronic materials.

In Chapter 5, the focus shifts to the synthesis and characterization of NMO-hBN composites via CSP. This chapter represents a significant advancement in tailoring composite properties for specific applications, particularly in the realm of microwave substrate materials. The engineered microstructures of interconnected hBN filler flakes within the NMO matrix yield composites with enhanced properties, including high relative densities, low permittivity, low dielectric loss, and improved thermal conductivity. Through a combination of experimental techniques including dilatometry, dielectric measurements, and microstructural analysis, the results in this chapter demonstrate the influence of filler volume fraction and particles alignment on the composite properties. The measured $Q \times f$ values, improvement of the electrical properties of resistivity and breakdown strength, together with the increase of the thermal conductivity, emphasize the potential of NMO-hBN composites for high-frequency microwave applications, positioning them as promising candidates for next-generation communication technologies.

Chapter 6 extends the investigation to NMO-diamond composites fabricated via CSP. This chapter represents a pioneering effort in harnessing the unique properties of diamond fillers to enhance composite performance. By achieving high relative densities and a homogeneous distribution of diamond filler within the NMO matrix, this chapter demonstrates the potential of CSP in fabricating composites with tailored dielectric, electrical, and thermal properties. Through comprehensive characterization, including ultrasonic non-destructive evaluation (NDE) and dielectric measurements, the chapter provides insights into the influence of filler volume fraction on composite properties. The observed increase in thermal conductivity and electrical breakdown strength highlights the potential of NMO-diamond composites for high-performance applications such as microwave substrates and electronic packaging materials.

Finally, Chapter 7 provides an analysis of the densification processes involved in ceramic composites undergoing CSP. This chapter represents a critical step towards optimizing composite fabrication processes and understanding the underlying mechanisms governing densification. By explaining the role of particle rearrangement, pressure solution creep, and diffusional steady-state creep, the dilatometry study offers valuable insights into the relationship between process parameters and the material’s microstructural features. These insights are crucial for advancing the design and fabrication of CSP-derived composites with tailored properties for diverse applications.

In conclusion, the advantages that CSP provides for the fabrication of ceramic composites, represent a paradigm shift in materials science and engineering. Through an experimental approach including microstructural design, materials synthesis, characterization of physical properties, and modeling to theoretical principles, this investigation underscores the transformative potential of CSP-derived composites in addressing challenges in communication technologies, electronic materials, and beyond. Moving forward, further research efforts aimed at optimizing process parameters, revealing fundamental mechanisms, and exploring novel material combinations will be instrumental in unlocking the full potential of CSP in materials synthesis and design.

8.2 Future work

This dissertation has explored the feasibility of integrating high thermal conductivity fillers along with a ceramic matrix, via cold sintering, to obtain composites of enhanced properties for applications of microwave substrates. The results documented in Chapter 5, revealed that the use of hexagonal Boron Nitride (hBN) as filler can improve several properties of interest for the mentioned application, such as lowering of the dielectric permittivity, increase of the electrical resistivity, higher electrical breakdown strength, reduction of the thermal coefficient of resonance frequency, and more importantly the increase of the thermal conductivity for the bulk cold sintered composite. Under the light of such remarkable improvements of properties, it is imperative to consider the possibility of utilizing hBN as a sole material to form microwave substrates.

A recent publication by Dai et al., achieves the densification of hBN under applied uniaxial pressures between 100 - 800 MPa, at room temperature, obtaining relative densities between 67 – 95 %, attributing the cohesiveness of the bulk material to the inter-flake Van der Waals bonds (π

bonds).[167] Building upon this approach, it is worth to use cold sintering to produce high density hBN pellet samples and characterize their physical properties, in order to asses its feasibility as a microwave substrate material.

As part of this dissertation, initial experiments have been conducted to obtain cold sintered hBN samples. The cold sintering parameters employed to densify a cilindrical hexagonal Boron Nitride (hBN, 99.8%, 70-80 nm, Nanoshel) pellet with dimensions of 13 mm in diameter and 2 mm in thickness, are the application of uniaxial pressure of 300 MPa, heating up from room temperature to 200°C at a heating rate of 2°C/min, holding the dwell temperature for 1 hour, and using deionized water as the transient liquid phase. For the fabrication of a pellet with 6 mm in thickness, same parameters were used, except for an extended dwell time of 3 hours instead. The fabricated cold sintered samples exhibited relative densities of 92.3 % and 93.5 %, for the pellets with thicknesses of 2 mm and 6 mm, respectively. Figure 8-1shows the enhanced densification resulting from the addition of heat and the transient liquid phase in the cold sintering process.

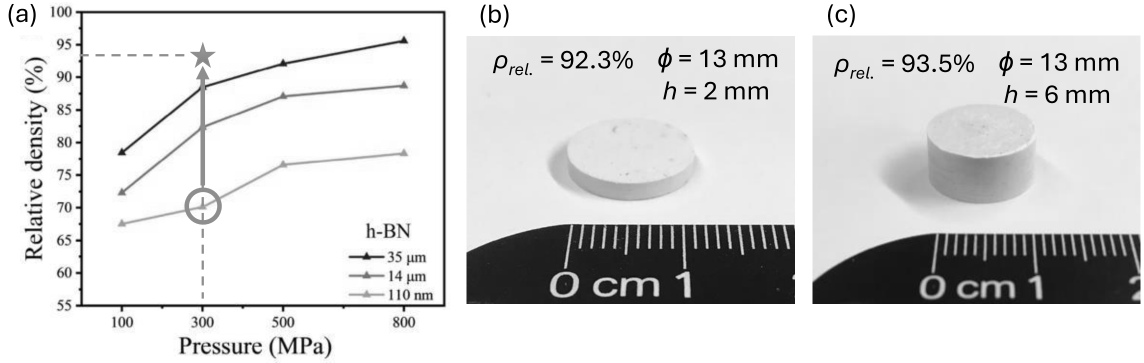

Figure **8-1**: (a) The addition of heat and water as the transient liquid phase in cold sintering, improved the relative density of hBN pellets from 70 to 93%. Figure adapted from reference.[167] (b,c) Cold sintered hBN pellets from this work.

X-Ray Diffraction (XRD) analysis of a cold sintered hBN sample's surface, revealed a textured microstructure, with major intensity from the peaks corresponding to (002) and (004), and suppressed peaks from the other indexed planes, as shown in Figure 8-2. This set of data suggests that there is a degree of [001] texture, as indicated by the maxima at the 002 and 004 peaks. The degree of [001] hBN texture can be evaluated using the Lotgering factor, *f*,

$$f = \frac{p - p_0}{1 - p_0} \quad \text{(Eq. 8.1)}$$

where *p*,

$$p = \frac{\sum I(002 + 004)}{\sum I(hkl)} \quad \text{(Eq. 8.2)}$$

is the ratio of the sum of the 002 and 004 peak intensities divided by the sum of all peak intensities (I) and p_o is that ratio for a randomly oriented sample.[168, 169] The calculated Lotgering factor was 90%. The origin of the texturized microstructure is understood to be caused by the uniaxial pressure, inducing the orientation of hBN flakes, to be preferentially perpendicular to the direction of the applied load.

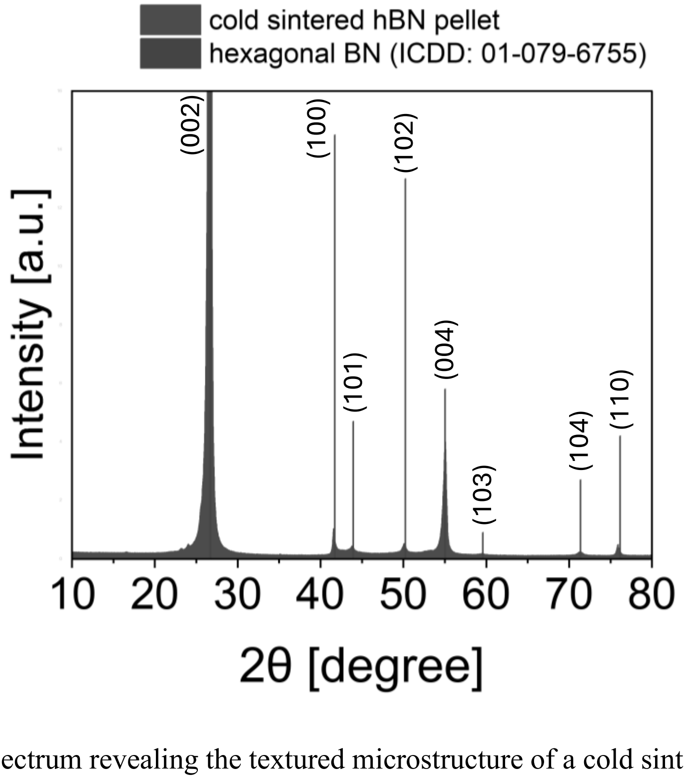

Figure **8-2**: XRD spectrum revealing the textured microstructure of a cold sintered hBN sample.

The dielectric properties of the cold sintered hBN samples were measured at a frequency of 10^6 Hz within a temperature range of 20 – 100°C, and by the Hakki-Coleman method at room temperature, finding a resonance frequency of 14.7 GHz. Figure 8-3 shows the results of the dielectric measurements at 10^6 Hz, yielding a relative permittivity $\varepsilon_r = 4.1$ and dielectric loss presenting values of $\tan \delta = 4 - 6 \times 10^{-3}$. The microwave frequency measurements at 14.7 GHz resulted in values of $\varepsilon_r = 4.9$, $\tan \delta = 1.7 \times 10^{-3}$ and $Q \times f \sim 8{,}000$ GHz. From these results, it may appear counterintuitive to observe a higher value of relative permittivity at the microwave frequency, because the increase of operating frequencies entails disabling certain polarization mechanisms in the material. To provide a plausible explanation for these counterintuitive experimental results, first it is necessary to keep in mind the anisotropic permittivity values for hBN, which are $\varepsilon_{hBN}\|$ = 6.93 (*in-plane* direction) and $\varepsilon_{hBN}\perp$ = 3.76 (*out-of-plane* direction). Secondly it should be considered that the applied electric field in the low frequency measurement travels linearly from electrode to electrode, through the material, therefore the measured capacitance corresponds mostly to the anisotropic relative permittivity from the *out-of-plane*

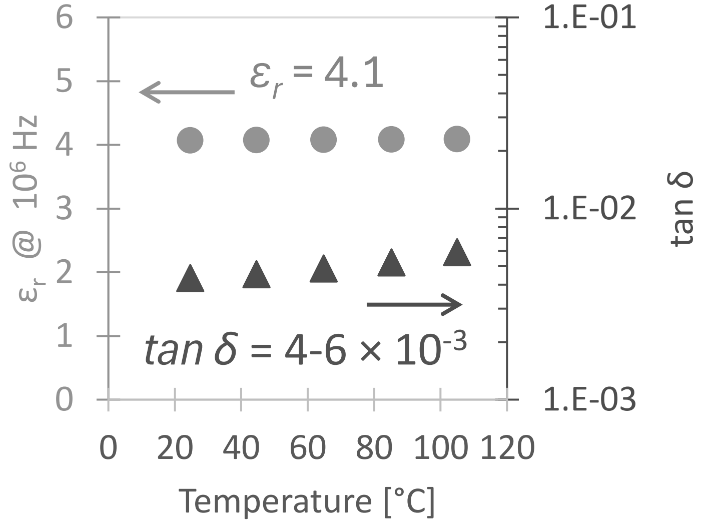

Figure **8-3**: Dielectric properties of cold sintered hBN pellet, at 10^6 Hz.

direction, in the textured microstructure. On the other hand, the electric field emitted by the antenna in the Hakki-Coleman method travels in a curved direction, and so there is more contribution to the measured effective permittivity from the *in-plane* direction of the textured microstructure, with respect to the low frequency measurements. In an attempt to semi-quantify the anisotropic permittivity ratio to the effective permittivity, for the 10^6 Hz frequency measurements

$$\varepsilon_{eff} = \frac{\varepsilon_{hBN} \parallel}{\varepsilon_{hBN} \perp} \sim \frac{1}{7}$$

And for the 14.7 GHz frequency measurements by the Hakki-Coleman method

$$\varepsilon_{eff} = \frac{\varepsilon_{hBN} \parallel}{\varepsilon_{hBN} \perp} \sim \frac{3}{4}$$

The 1/7 ratio (~86%) of anisotropic permittivity measured from the applied electric field at 10^6 Hz through the hBN sample, is slightly smaller than the Lotgering factor of 90% calculated from the XRD data of the sample's surface. This suggests that the texture degree in the hBN pellets may be to some extent higher at the top and bottom surfaces, but the results from both techniques infer high levels of textured microstructure.

Initial preliminary results from analysis of dielectric properties, position hBN as a potentially viable alternative as a microwave substrate material.

Appendix A

Cold Sintering of Geopolymers: A Novel Approach for Dense Aluminosilicates

Geopolymers, a class of aluminosilicate compounds, have recently gained significant attention in materials science due to their properties and potential applications. This study in collaboration with researchers from the University of Padova, Italy, investigates the synthesis of geopolymer dense bodies employing cold sintering, a recently developed low-energy sintering technique. Geopolymers exhibit an inorganic, amorphous nature characterized by a continuous 3D structure formed through alkali activation of aluminum-silicate sources such as metakaolin or fly ash. The network architecture comprises interconnected SiO_4 and AlO_4 tetrahedra sharing interstitial oxygens, stabilized by the presence of positive ions such as Na^+ and K^+. Notably, geopolymers demonstrate exceptional properties including high temperature resistance, strong interfacial bonding ability, and corrosion resistance, making them promising candidates for various applications.

Cold sintering offers a promising alternative for the fabrication of geopolymer-based materials by densifying powders with the aid of a liquid phase, typically a water solution, under high external pressure and limited heating conditions (<350°C). This environmentally friendly and energy-efficient approach holds significant potential for diverse applications, including toxic waste encapsulation and composite matrix formation. The successful production of geopolymer dense bodies through cold sintering underscores the viability of this technique for advancing materials synthesis and engineering.

In this study, the cold sintering process of Sodium doped alumino-silicate (SiO_2 54.8 wt.%, Al_2O_3 23.3 wt.%, Fe_2O_3 1.1 wt.%, TiO_2 0.9 wt.%, MgO 0.4 wt.%, K_2O 0.9 wt.%, Na_2O 18.7 wt.%) with particle size between 45 – 125 µm, comprised the application of a uniaxial pressure of P = 70

MPa, heating rates (α) of 6.5, 13.0 and 30°C/min, from room temperature to T = 150°C. These pressure and temperature conditions were held for a dwell time of t = 30 min. The mentioned cold sintered parameters produced pellets of 13 mm of diameter and 3.5 mm of thickness, with relative densities above 92 %.

Dilatometry studies were conducted, as described in *Section 5.2.3 Dilatometry study*, to determine the activation energy of densification, according to the Woolfrey-Bannister method[153] described in *Section 7.3.1 Pressure Solution Creep analysis on NMO-hBN and NMO-md composites* of this dissertation. The calculated activation energy of densification was Q = 22 ± 5 kJ/mol, and the analysis for this calculations is shown in Figure A-1. The value of the calculated activation energy correlates well with previously reported values for the pressure solution creep densification mechanism characteristic of the cold sintering process.[114]

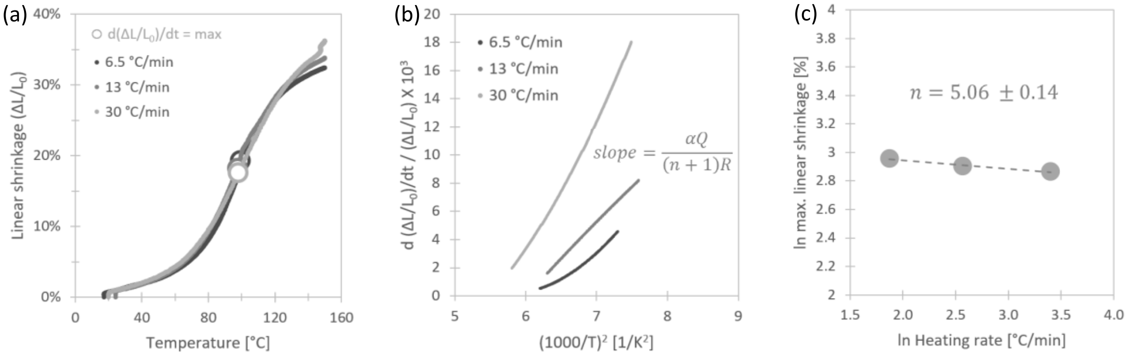

Figure **A-1**: (a) Sodium alumino-silicate geopolymers undergoing cold sintering at different heating rates of 6.5, 13.0 and 30.0°C/min, with the corresponding strain under an applied stress of 70 MPa, (b) shrinkage strain rate versus inverse squared temperature, and (c) natural log-log plot of the strain at maximum strain rate versus heating rate.

References

1. Zhao X, Guo J, Wang K, De Beauvoir TH, Li B, Randall CA. Introducing a ZnO–PTFE nanocomposite varistor via the cold sintering process. *Adv Eng Mater*. 2018;1700902:1–8. https://doi.org/10.1002/adem.201700902
2. Sada T, Tsuji K, Ndayishimiye A, Fan Z, Fujioka Y, Randall CA. Enhanced high permittivity $BaTiO_3$–polymer nanocomposites from the cold sintering process. *J Appl Phys*. 2020;128(July 2020):084103. https://doi.org/10.1063/5.0021040
3. Mena-Garcia J, Dursun S, Tsuji K, *et al.* Integration and characterization of a ferroelectric polymer PVDF-TrFE into the grain boundary structure of ZnO via cold sintering. *J Eur Ceram Soc*. 2022; 42 (January): 2789–2797. https://doi.org/10.1016/j.jeurceramsoc.2022.01.064
4. Li Y, Zheng M, Zang M, Zhu M, Hou Y. Cold sintering co-firing of (Ca, Bi) (Mo, V)O_4–PTFE composites in a single step. *J Am Ceram Soc*. 2022;105(December 2021):6262–6270. https://doi.org/10.1111/jace.18595
5. Vilesh VL, Santha N, Subodh G. Influence of Li_2MoO_4 and polytetrafluoroethylene addition on the cold sintering process and dielectric properties of $BaBiLiTeO_6$ ceramics. *Ceram Int*. 2021;47(May):30756–30763. https://doi.org/10.1016/j.ceramint.2021.07.255
6. Gyan DS, Dwivedi A. Structural and electrical characterization of $NaNbO_3$-PVDF nanocomposites fabricated using cold sintering synthesis route. *J Appl Phys*. 2019;125(December 2018):024103. https://doi.org/10.1063/1.5046458
7. Guo J, Legum B, Anasori B, *et al.* Cold sintered ceramic nanocomposites of 2D MXene and zinc oxide. *Adv Mater*. 2018;30(1801846):1–6. https://doi.org/10.1002/adma.201801846
8. Gao J, Ding Q, Yan P, *et al.* Highly improved microwave absorbing and mechanical properties in cold sintered ZnO by incorporating graphene oxide. *J Eur Ceram Soc*. 2022;42(October 2021):993–1000. https://doi.org/10.1016/j.jeurceramsoc.2021.10.053
9. Guo J, Si M, Zhao X, *et al.* Altering interfacial properties through the integration of C_{60} into ZnO ceramic via cold sintering process. *Carbon N Y*. 2022;190:255–261. https://doi.org/10.1016/j.carbon.2022.01.017
10. Vakifahmetoglu C, Karacasulu L. Cold sintering of ceramics and glasses: A review. *Curr Opin Solid State Mater Sci*. 2020;24(December 2019):100807. https://doi.org/10.1016/j.cossms.2020.100807
11. Kahari H, Teirikangas M, Juuti J, Jantunen H. Dielectric properties of lithium molybdate ceramic fabricated at room temperature. *J Am Ceram Soc*. 2014;97(11):3378–3379. https://doi.org/10.1111/jace.13277
12. Kahari H, Teirikangas M, Juuti J, Jantunen H. Room-temperature fabrication of microwave dielectric Li_2MoO_4–TiO_2 composite ceramics. *Ceram Int*. 2016;42:11442–11446. https://doi.org/10.1016/j.ceramint.2016.04.081
13. Ramachandran P, Kahari H, Juuti J, Jantunen H. Room temperature densified ceramics for weight optimized circular polarized GPS antenna design. *Microw Opt Technol Lett*. 2018;60:1061–1066. https://doi.org/10.1002/mop.31105
14. Ji Y, Song K, Luo X, Liu B, Bafrooei HB, Wang D. Microwave dielectric properties of $(1-x)Li_2MoO_4$-xMg_2SiO_4 composite ceramics fabricated by cold sintering process. *Front*

Mater. 2019;6(October):256. https://doi.org/10.3389/fmats.2019.00256

15. Wang D, Li L, Jiang J, *et al.* Cold sintering of microwave dielectric ceramics and devices. *J Mater Res*. 2021;36(2):333–349. https://doi.org/10.1557/s43578-020-00029-w
16. Wang D, Zhang S, Zhou D, *et al.* Temperature stable cold sintered $(Bi_{0.95}Li_{0.05})(V_{0.9}Mo_{0.1})O_4$-$Na_2Mo_2O_7$ microwave dielectric composites. *Materials (Basel)*. 2019;12(1370):1–10. https://doi.org/10.3390/ma12091370
17. Wang D, Chen J, Wang G, *et al.* Cold sintered $LiMgPO_4$ based composites for low temperature co-fired ceramic (LTCC) applications. *J Am Ceram Soc*. 2020;103(May):6237–6244. https://doi.org/10.1111/jace.17320
18. Guo J, Baker AL, Guo H, Lanagan M, Randall CA. Cold sintering process: A new era for ceramic packaging and microwave device development. *J Am Ceram Soc*. 2017;100(July):669–677. https://doi.org/10.1111/jace.14603
19. Induja IJ, Sebastian MT. Microwave dielectric properties of mineral sillimanite obtained by conventional and cold sintering process. *J Eur Ceram Soc*. 2017;37:2143–2147. https://doi.org/10.1016/j.jeurceramsoc.2017.01.007
20. Hong W Bin, Li L, Yan H, Chen XM. Cold sintering and microwave dielectric properties of dense HBO_2-II ceramics. *J Am Ceram Soc*. 2019;102(January):5934–5940. https://doi.org/10.1111/jace.16450
21. Hao J, Guo J, Zhao E, *et al.* Grain size effect on microwave dielectric properties of Na_2WO_4 ceramics prepared by cold sintering process. *Ceram Int*. 2020;46(June):27193–27198. https://doi.org/10.1016/j.ceramint.2020.07.200
22. Vandiver P, Soffer O, Klima B, Svoboda J. The origins of ceramic technology at Dolni Vestonice, Czechoslovakia. *Science (80)*. 1989;246:1002–1008.
23. Kingery WD, Bowen HK, Uhlmann DR. Introduction to ceramics. 2d ed. Wiley series on the science and technology of materials; 1976
24. Rahaman MN. Sintering of ceramics. CRC Press; 2007
25. Kang S-JL. Sintering. Densification, grain growth and microstructure. Oxford: Elsevier; 2005
26. Grasso S, Biesuz M, Zoli L, *et al.* A review of cold sintering processes. *Adv Appl Ceram*. 2020;119(3):115–143. https://doi.org/10.1080/17436753.2019.1706825
27. Ibn-mohammed T, Randall CA, Mustapha KB, *et al.* Decarbonising ceramic manufacturing: A techno-economic analysis of energy efficient sintering technologies in the functional materials sector. *J Eur Ceram Soc*. 2019;39(16):5213–5235. https://doi.org/10.1016/j.jeurceramsoc.2019.08.011
28. Guo H, Guo J, Baker A, Randall CA. Hydrothermal-assisted cold sintering process: A new guidance for low-temperature ceramic sintering. *ACS Appl Mater Interfaces*. 2016;8:20909–20915. https://doi.org/10.1021/acsami.6b07481
29. Guo J, Guo H, Baker AL, *et al.* Cold sintering: A paradigm shift for processing and integration of ceramics. *Angew Chemie - Int Ed*. 2016;55(38):11457–11461. https://doi.org/10.1002/anie.201605443
30. Bang SH, Ndayishimiye A, Randall CA. Mechanistic approach to identify densification kinetics and mechanisms of zinc oxide cold sintering. *Acta Mater*. 2019. https://doi.org/10.2139/ssrn.3428070
31. Gratier JP, Dysthe DK, Renard F. The role of pressure solution creep in the ductility of the Earth's upper crust. Elsevier Inc.; 2013 https://doi.org/10.1016/B978-0-12-380940-7.00002-0
32. Newnham RE, Skinner DP, Cross LE. Connectivity and piezoelectric-pyroelectric composites. *Mater Res Bull*. 1978;13(5):525–536.
33. Newnham RE. Composite electroceramics. *Annu Rev Mater Sci*. 1986;16:47–68.

34. Guo J, Guo H, Sohrabi D, Heidary B, Funahashi S, Randall CA. Semiconducting properties of cold sintered V_2O_5 ceramics and co-sintered V_2O_5-PEDOT:PSS composites. *J Eur Ceram Soc*. 2017;37(4):1529–1534. https://doi.org/10.1016/j.jeurceramsoc.2016.11.021
35. Zhao Y, Berbano SS, Gao L, *et al.* Cold-sintered V_2O_5-PEDOT:PSS nanocomposites for negative temperature coefficient materials. *J Eur Ceram Soc*. 2019;39(August 2018):1257–1262. https://doi.org/10.1016/j.jeurceramsoc.2018.10.018
36. Heidary D, Guo J, Seo J, Guo H, Rajagopalan R, Randall CA. Microstructures and electrical properties of V_2O_5 and carbon-nanofiber composites fabricated by cold sintering process. *Jpn J Appl Phys*. 2018;57(025702). https://doi.org/https://doi.org/10.7567/JJAP.57.025702
37. Seo J-H, Guo J, Guo H, *et al.* Cold sintering of a Li-ion cathode: $LiFePO_4$-composite with high volumetric capacity. *Ceram Int*. 2017;43(August):15370–15374. https://doi.org/10.1016/j.ceramint.2017.08.077
38. Guo J, Berbano SS, Guo H, Baker AL, Lanagan MT, Randall CA. Cold sintering process of composites: Bridging the processing temperature gap of ceramic and polymer materials. *Adv Funct Mater*. 2016;26:7115–7121. https://doi.org/10.1002/adfm.201602489
39. Zhao X, Guo J, Wang K, Herisson De Beauvoir T, Li B, Randall CA. Introducing a ZnO–PTFE (Polymer) nanocomposite varistor via the cold sintering process. *Adv Eng Mater*. 2018;20(1700902):1–8. https://doi.org/10.1002/adem.201700902
40. Ndayishimiye A, Grady ZA, Tsuji K, Wang K, Bang SH, Randall CA. Thermosetting polymers in cold sintering: The fabrication of ZnO-polydimethylsiloxane composites. *J Am Ceram Soc*. 2020;103(August 2019):3039–3050. https://doi.org/10.1111/jace.17009
41. Dursun S, Tsuji K, Bang SH, Ndayishimiye A, Randall CA. A route towards fabrication of functional ceramic/polymer nanocomposite devices using the cold sintering process. *ACS Appl Electron Mater*. 2020;2:1917–1924. https://doi.org/10.1021/acsaelm.0c00225
42. Si M, Hao J, Zhao E, *et al.* Preparation of zinc oxide/poly-ether-ether-ketone (PEEK) composites via the cold sintering process. *Acta Mater*. 2021;215:117036. https://doi.org/10.1016/j.actamat.2021.117036
43. Si M, Guo J, Hao J, Zhao X, Randall CA, Wang H. Cold sintered composites consisting of PEEK and metal oxides with improved electrical properties via the hybrid interfaces. *Compos Part B*. 2021;226(109349). https://doi.org/10.1016/j.compositesb.2021.109349
44. Guo J, Pfei N, Beese A, *et al.* Cold sintering $Na_2Mo_2O_7$ ceramic with poly(ether imide) (PEI) polymer to realize high-performance composites and integrated multilayer circuits. *ACS Appl Nano Mater*. 2018;1:3837–3844. https://doi.org/10.1021/acsanm.8b00609
45. Mena-Garcia J, Ndayishimiye A, Fan Z, *et al.* Sodium molybdate-hexagonal boron nitride composites enabled by cold sintering for microwave dielectric substrates. *J Am Ceram Soc*. 2023;(June):1–11. https://doi.org/10.1111/jace.19254
46. Mena-Garcia J, Mervosh MW, Yousefian P, *et al.* Dielectric, electrical and thermal properties of sodium molybdate-hexagonal boron nitride composites enabled by cold sintering. *Ceram Int*. 2024. https://doi.org/10.1016/j.ceramint.2024.05.155
47. Nayir S, Waryoba DR, Rajagopalan R, Arslan C, Randall CA. Cold sintering of a covalently bonded MoS_2/graphite composite as a high capacity Li–ion electrode. *ChemNanoMat*. 2018;4:1088–1094. https://doi.org/10.1002/cnma.201800342
48. Lee W, Lyon CK, Seo J-H, *et al.* Ceramic–salt composite electrolytes from cold sintering. *Adv Funct Mater*. 2019;29(1807872):1–8. https://doi.org/10.1002/adfm.201807872
49. Ndayishimiye A, Tsuji K, Wang K, Bang SH, Randall CA. Sintering mechanisms and dielectric properties of cold sintered (1-x)SiO_2-xPTFE composites. *J Eur Ceram Soc*. 2019;39(15):4743–4751. https://doi.org/10.1016/j.jeurceramsoc.2019.07.048
50. Sada T, Tsuji K, Ndayishimiye A, Fan Z, Fujioka Y, Randall CA. High permittivity $BaTiO_3$ and $BaTiO_3$-polymer nanocomposites enabled by cold sintering with a new transient

chemistry: $Ba(OH)_2{\cdot}8H_2O$. *J Eur Ceram Soc*. 2021;41(August 2020):409–417. https://doi.org/10.1016/j.jeurceramsoc.2020.07.070

51. Nunokawa T, Takashima K, Mizuno K, Randall CA. Impact of PTFE particle size in designing $BaTiO_3$ dielectric composites under the cold sintering process. *Jpn J Appl Phys*. 2023;62(071003). https://doi.org/10.35848/1347-4065/ace145
52. Okazaki T, Sada T, Tsuji K, Fujioka Y, Randall CA. $BaTiO_3$-based composites provide new opportunities enabled by the cold sintering process. *Jpn J Appl Phys*. 2023;62(SM1030). https://doi.org/10.35848/1347-4065/acf478
53. Sada T, Tsuji K, Ndayishimiye A, Fan Z, Fujioka Y, Randall CA. Highly reliable $BaTiO_3$-polyphenylene oxide nanocomposite dielectrics via cold sintering. *Adv Mater Interfaces*. 2021;8(2100963):1–11. https://doi.org/10.1002/admi.202100963
54. Wang D, Tsuji K, Randall CA, Trolier-Mckinstry S. Model for the cold sintering of lead zirconate titanate ceramic composites. *J Am Ceram Soc*. 2020;103(May):4894–4902. https://doi.org/10.1111/jace.17269
55. Gupta S, Wang D, Shetty S, *et al.* Cold sintering of PZT 2-2 composites for high frequency ultrasound transducer arrays. *MDPI Actuators*. 2021;10(235). https://doi.org/doi.org/10.3390/act10090235
56. Seo J-H, Nakaya H, Takeuchi Y, *et al.* Broad temperature dependence, high conductivity, and structure-property relations of cold sintering of LLZO-based composite electrolytes. *J Eur Ceram Soc*. 2020; 40 (15): 6241–6248. https://doi.org/10.1016/j.jeurceramsoc.2020.06.050
57. Grady Z, Fan Z, Ndayishimiye A, Randall CA. Design and sintering of all-solid-state composite cathodes with tunable mixed conduction properties via the cold sintering process. *ACS Appl Mater Interfaces*. 2021; 13: 48071–48087. https://doi.org/10.1021/acsami.1c13913
58. Grady Z, Fan Z, Fanghanel J, Randall CA. Conductivity of cold sintered diphasic composites containing a ceramic active material and a solid-state electrolyte or carbon for all solid-state batteries. *J Mater Chem A*. 2024;12(4492):4492–4512. https://doi.org/10.1039/d3ta07067k
59. Wang D, Zhou D, Zhang S, *et al.* Cold-sintered temperature stable $Na_{0.5}Bi_{0.5}MoO_4$-Li_2MoO_4 Microwave Composite Ceramics. *ACS Sustain Chem Eng*. 2018;6:2438–2444. https://doi.org/10.1021/acssuschemeng.7b03889
60. Vilesh VL, Santha N, Subodh G. Influence of Li_2MoO_4 and polytetrafluoroethylene addition on the cold sintering process and dielectric properties of $BaBiLiTeO_6$ ceramics. *Ceram Int*. 2021;47(21):30756–30763. https://doi.org/10.1016/j.ceramint.2021.07.255
61. McLachlan DS, Blaszkiewicz M, Newnham RE. Electrical resistivity of composites. *J Am Ceram Soc*. 1990;73(8):2187–2203.
62. Bowen CP. A study of dielectrophoresis as a means to assemble ceramic-polymer composite materials. PhD Thesis; The Pennsylvania State University; 1996
63. Rahaman M, Aldalbahi A, Govindasami P, *et al.* A new insight in determining the percolation threshold of electrical conductivity for extrinsically conducting polymer composites through different sigmoidal models. *MDPI Polym*. 2017;9(527):1–17. https://doi.org/10.3390/polym9100527
64. Maruzhenko O, Mamunya Y, Boiteux G, Pusz S, Szeluga U, Pruvost S. Improving the thermal and electrical properties of polymer composites by ordered distribution of carbon micro- and nanofillers. HAL Id : hal-02136462. *Int J Heat Mass Transf*. 2019;138:75–84.
65. Brovelli A, Cassiani G. A combination of the Hashin-Shtrikman bounds aimed at modelling electrical conductivity and permittivity of variably saturated porous media. *Geophys J Int*. 2010;180:225–237. https://doi.org/10.1111/j.1365-246X.2009.04415.x

66. Banno H. Effects of shape and volume fraction of closed pores on remanent polarization and coercive force of ferroelectric ceramics. *Jpn J Appl Phys*. 1987;26(2):50–52. https://doi.org/10.7567/JJAPS.26S2.50
67. Neelakanta PS. Handbook of electromagnetic materials: Monolithic and composite versions and their applications. CRC Press; 1995
68. Frohlich H. Theory of dielectrics: Dielectric constant and dielectric loss. 2nd ed. Clarendon Press; 1958
69. Goncharenko A V., Lozovski VZ, Venger EF. Lichtenecker's equation: Applicability and limitations. *Opt Commun*. 2000;174(January):19–32.
70. Doyle WT. The Clausius-Mossotti problem for cubic arrays of spheres. *J Appl Phys*. 1978;49:795–797. https://doi.org/10.1063/1.324659
71. Moulson, A.J.; Herbert JM. Electroceramics. 2nd ed. West Sussex, England: John Wiley & Sons Ltd.; 2003
72. Macdonald JR, Barsoukov E. Impedance spectroscopy: Theory, experiment and applications. 2nd ed. Hoboken, New Jersey: Wiley-Interscience; 2005
73. Miller PH. The electrical conductivity of zinc oxide. *Phys Rev*. 1941;60(12):890–895. https://doi.org/10.1103/PhysRev.60.890
74. Levinson LM, Philipp HR. Zinc oxide varistors - a review. *Am Ceram Soc Bull*. 1986;65(4):639–646.
75. Mahan GD, Levinson LM, Philipp HR. Theory of conduction in ZnO varistors. *J Appl Phys*. 1979;50(4):2799–2812. https://doi.org/10.1063/1.326191
76. Chiu FC. A review on conduction mechanisms in dielectric films. *Adv Mater Sci Eng*. 2014. https://doi.org/10.1155/2014/578168
77. Tsuji K, Chen W, Guo H, Lee W, Randall CA, Guillemet S. Contrasting conduction mechanisms of two internal barrier layer capacitors: (Mn, Nb)-doped $SrTiO_3$ and $CaCu_3Ti_4O_{12}$. *J Appl Phys*. 2017;121(6). https://doi.org/10.1063/1.4976011 . hal-02403341
78. Pecht MG, Agarwal R, McCluskey P, Dishongh T, Javadpour S, Mahajan R. Electronic packaging materials and their properties. CRC Press; 1999
79. Viswanadham P. Essentials of electronic packaging: A multidisciplinary approach. ASME Press; 2011
80. Imanaka Y. Multilayered low temperature cofired ceramics (LTCC) technology. Springer; 2005
81. Bouville F, Studart AR. Geologically-inspired strong bulk ceramics made with water at room temperature. *Nat Commun*. 2017; 8 (14655): 1–8. https://doi.org/10.1038/ncomms14655
82. Zhang X, Spiers CJ, Peach CJ. Compaction creep of wet granular calcite by pressure solution at 28°C to 150°C. *J Geophys Res Solid Earth*. 2010;115(9):1–18. https://doi.org/10.1029/2008JB005853
83. Ndayishimiye A, Sengul MY, Sada T, *et al.* Roadmap for densification in cold sintering: Chemical pathways. *Open Ceram*. 2020; 2 (July): 100019. https://doi.org/10.1016/j.oceram.2020.100019
84. Bang SH, Ndayishimiye A, Randall CA. Anisothermal densification kinetics of the cold sintering process below 150°C. *J Mater Chem C*. 2020;8:5668–5672. https://doi.org/10.1039/d0tc00395f
85. Sada T, Ndayishimiye A, Fan Z, Fujioka Y, Randall CA. Surface modification of $BaTiO_3$ with catechol surfactant and effects on cold sintering. *J Appl Phys*. 2021;129(18). https://doi.org/10.1063/5.0049905
86. Liu JA, Li CH, Shan JJ, Wu JM, Gui RF, Shi YS. Preparation of high-density $InGaZnO_4$ target by the assistance of cold sintering. *Mater Sci Semicond Process*. 2018;84(April):17–

23. https://doi.org/10.1016/j.mssp.2018.04.030

87. Kang X, Floyd R, Lowun S, Cabral M, Dickey E, Maria J-P. Mechanism studies of hydrothermal cold sintering of zinc oxide at near room temperature. *J Am Ceram Soc*. 2019;102(December 2018):4459–4469. https://doi.org/10.1111/jace.16340
88. Liu Y, Sun Q, Wang D, Adair K, Liang J, Sun X. Development of the cold sintering process and its application in solid-state lithium batteries. *J Power Sources*. 2018;393(March):193–203. https://doi.org/10.1016/j.jpowsour.2018.05.015
89. Ndayishimiye A, Grady Z, Tsuji K, Wang K, Bang SH, Randall CA. Thermosetting polymers in cold sintering: The fabrication of ZnO-polydimethylsiloxane composites. *J Am Ceram Soc*. 2020;103(5):3039–3050. https://doi.org/10.1111/jace.17009
90. Guo J, Pfeiffenberger N, Beese A, *et al.* Cold sintering $Na_2Mo_2O_7$ ceramic with poly(ether imide) (PEI) polymer to realize high-performance composites and integrated multilayer circuits. *ACS Appl Nano Mater*. 2018; 1: 3837–3844. https://doi.org/10.1021/acsanm.8b00609
91. Zhang QM, Bharti V, Zhao X. Giant electrostriction and relaxor ferroelectric behavior in electron- irradiated poly(vinylidene fluoride-trifluoroethylene) copolymer. *Science (80)*. 1998;280(5372):2101–2104. https://doi.org/10.1126/science.280.5372.2101
92. Tsutsumi N, Ueyasu A, Sakai W, Chiang CK. Crystalline structures and ferroelectric properties of ultrathin films of vinylidene fluoride and trifluoroethylene copolymer. *Thin Solid Films*. 2005;483(1–2):340–345. https://doi.org/10.1016/j.tsf.2004.12.033
93. Özgür Ü, Alivov YI, Liu C, *et al.* A comprehensive review of ZnO materials and devices. *J Appl Phys*. 2005;98(4):1–103. https://doi.org/10.1063/1.1992666
94. Maria JP, Kang X, Floyd RD, *et al.* Cold sintering: Current status and prospects. *J Mater Res*. 2017;32(17):3205–3218. https://doi.org/10.1557/jmr.2017.262
95. Moriwake H, Konishi A, Ogawa T, *et al.* Ferroelectricity in wurtzite structure simple chalcogenide. *Appl Phys Lett*. 2014;104(24):1–4. https://doi.org/10.1063/1.4884596
96. Miller LS, Mullin JB. Electronic materials from silicon to organics. New York: Springer Science Business Media; 1991 https://doi.org/10.1007/978-1-4615-3818-9
97. Nazir NA, Kim N, Iglesias WG, Jakli A, Kyu T. Conductive behavior in relation to domain morphology and phase diagram of nafion/poly(vinylidene-co-trifluoroethylene) blends. *Polymer (Guildf)*. 2012;53(1):196–204. https://doi.org/10.1016/j.polymer.2011.11.019
98. Arrigoni A, Brambilla L, Bertarelli C, Serra G, Tommasini M, Castiglioni C. PVDF-TrFE nanofibers: Structure of the ferroelectric and paraelectric phases through IR and Raman spectroscopies. *RSC Adv*. 2020;10(62):37779–37796. https://doi.org/10.1039/d0ra05478j
99. Milani A, Castiglioni C, Radice S. Joint experimental and computational investigation of the structural and spectroscopic properties of poly(vinylidene fluoride) polymorphs. *J Phys Chem B*. 2015;119(14):4888–4897. https://doi.org/10.1021/acs.jpcb.5b00161
100. Jonscher AK. Dielectric relaxation in solids, Chelsea. *Dielectr Pub, London*. 1983.
101. Guler O. Effect of carbon nanotubes produced by using different methods on electrical and optical properties of zinc oxide–carbon nanotube composite. *Int J Mater Res*. 2015;106(6):641–646. https://doi.org/10.3139/146.111218
102. Beebe JM, Kim B, Gadzuk JW, Frisbie CD, Kushmerick JG. Transition from direct tunneling to field emission in metal-molecule-metal junctions. *Phys Rev Lett*. 2006;97(2):026801. https://doi.org/10.1103/PhysRevLett.97.026801
103. Ikuno T, Okamoto H, Sugiyama Y, Nakano H, Yamada F, Kamiya I. Electron transport properties of Si nanosheets: Transition from direct tunneling to Fowler-Nordheim tunneling. *Appl Phys Lett*. 2011;99(2):1–4. https://doi.org/10.1063/1.3610486
104. Yoon SH, Kim SH, Kim DY. Correlation between I (current)-V (voltage) characteristics and thermally stimulated depolarization current of Mn-doped $BaTiO_3$ multilayer ceramic

capacitor. *J Appl Phys*. 2013;114(7):074102. https://doi.org/10.1063/1.4818947

105. Peng CJ, Hu H, Krupanidhi SB. Electrical properties of strontium titanate thin films by multi-ion-beam reactive sputtering technique. *Appl Phys Lett*. 1993;63(8):1038–1040. https://doi.org/10.1063/1.109827
106. Meng N, Ren X, Zhu X, *et al.* Multiscale understanding of electric polarization in poly(vinylidene fluoride)-based ferroelectric polymers. *J Mater Chem C*. 2020;8(46):16436–16442. https://doi.org/10.1039/d0tc04310a
107. Oshikiri M, Imanaka Y, Aryasetiawan F, Kido G. Comparison of the electron effective mass of the n-type ZnO in the wurtzite structure measured by cyclotron resonance and calculated from first principle theory. *Phys B Condens Matter*. 2001;298(1–4):472–476. https://doi.org/10.1016/S0921-4526(01)00365-9
108. He J. Metal oxide varistors. Weinheim, Germany: Wiley-VCH; 2019 https://doi.org/10.1146/annurev.ms.17.080187.001503
109. Blatter G, Greuter F. Carrier transport through grain boundaries in semiconductors. *Introd to Semicond Phys*. 1986;33(6):77–86. https://doi.org/10.1142/9789812816733_0006
110. Božanić M, Sinha S. Millimeter-wave integrated circuits. Cham, Switzerland: Springer; 2020 https://doi.org/10.1007/978-3-030-44398-6
111. Valasa S, Kotha VR, Vadthiya N. Beyond Moore's law – A critical review of advancements in negative capacitance field effect transistors: A revolution in next-generation electronics. *Mater Sci Semicond Process*. 2024;173(108116). https://doi.org/10.1016/j.mssp.2024.108116
112. Sebastian MT, Jantunen H. Low loss dielectric materials for LTCC applications: a review. *Int Mater Rev*. 2008;53(2):57–90. https://doi.org/10.1179/174328008X277524
113. Funahashi S, Guo J, Guo H, *et al.* Demonstration of the cold sintering process study for the densification and grain growth of ZnO ceramics. *J Am Ceram Soc*. 2017;100(May 2016):546–553. https://doi.org/10.1111/jace.14617
114. Ndayishimiye A, Bang SH, Spiers CJ, Randall CA. Reassessing cold sintering in the framework of pressure solution theory. *J Eur Ceram Soc*. 2023;43(September 2022):1–13. https://doi.org/10.1016/j.jeurceramsoc.2022.09.053
115. Galotta A, Sglavo VM. The cold sintering process: A review on processing features, densification mechanisms and perspectives. *J Eur Ceram Soc*. 2021;41(July):1–17. https://doi.org/10.1016/j.jeurceramsoc.2021.09.024
116. Sibi N, Rajan A, Subodh G. Garnet mineral based composites through cold sintering process: Microstructure and dielectric properties. *J Eur Ceram Soc*. 2020;40(September 2019):371–375. https://doi.org/10.1016/j.jeurceramsoc.2019.09.012
117. Garcia-Martin E, Granados-Miralles C, Ruiz-Gomez S, *et al.* Dense strontium hexaferrite-based permanent magnet composites assisted by cold sintering process. *J Alloys Compd*. 2022;917:165531. https://doi.org/10.1016/j.jeurceramsoc.2019.09.012
118. Yang C, Li J, Wang X, *et al.* ZrW_2O_8/ZrO_2 composites with low/near-zero coefficients of thermal expansion fabricated at ultralow temperature: An integration of hydrothermal assembly and a cold sintering process. *ACS Appl Mater Interfaces*. 2021;13:39738–39747. https://doi.org/10.1021/acsami.1c10108
119. Liu M, Jin Q, Shen P. Cold sintering of $NaNO_3/MgO$ heat-storage composite. *Ceram Bull*. 2020;46(July):28955–28960. https://doi.org/10.1016/j.ceramint.2020.08.066
120. Cahill DG, Ford WK, Goodson KE, *et al.* Nanoscale thermal transport. *J Appl Phys*. 2017;93(January 2002):793–818. https://doi.org/10.1063/1.1524305
121. Cahill DG, Braun P V, Chen G, *et al.* Nanoscale thermal transport. II. 2003–2012. *Appl Phys Rev*. 2014;011305–1(April 2013). https://doi.org/10.1063/1.4832615
122. Yu C, Zhang J, Tian W, Fan X, Yao Y. Polymer composites based on hexagonal boron

nitride and their application in thermally conductive composites. *RSC Adv*. 2018;8:21948–21967. https://doi.org/10.1039/c8ra02685h

123. Vetser A. Cold Sintering of $Na_2Mo_2O_7$ hexagonal BN composites for MLCC applications. Master's thesis; The Pennsylvania State University; 2023
124. Ndayishimiye A, Fan Z, Mena-Garcia J, Anderson JM, Randall CA. Coalescence in cold sintering: A study on sodium molybdate. *Open Ceram*. 2022;11(April):100293. https://doi.org/10.1016/j.oceram.2022.100293
125. Zhu W, Kamali AR. On the reactive molten salt synthesis, solubility and Na-ion storage performance of $Na_2Mo_2O_7$. *J Electrochem Soc*. 2021;168(046517). https://doi.org/10.1149/1945-7111/abf5a4
126. Hakki BW, Coleman PD. A dielectric resonator method of measuring inductive capacities in the millimeter range. *IRE Trans Microw Theory Tech*. 1960;8(4):402–410. https://doi.org/10.1109/TMTT.1960.1124749
127. Kata K, Shimada Y, Takamizawa H. Low dielectric constant new materials for multilayer ceramic substrate. *IEEE Trans Components, Hybrids Manuf Technol*. 1990;13(2):448–451.
128. Laturia A, Van de Put ML, Vandenberghe WG. Dielectric properties of hexagonal boron nitride and transition metal dichalcogenides: from monolayer to bulk. N*pj 2D Mater Appl*. 2018;2(6):1–6. https://doi.org/10.1038/s41699-018-0050-x
129. Narang SB, Bahel S. Low loss dielectric ceramics for microwave applications: A review. *J Ceram Process Res*. 2010;11(3):316–321.
130. Pang L, Zhou D, Guo J, Qi Z, Shao T. Microwave dielectric properties of scheelite structured low temperature fired $Bi(In_{1/3}Mo_{2/3})O_4$ ceramic. *Ceram Int*. 2013;39:4719–4722. https://doi.org/10.1016/j.ceramint.2012.11.021
131. Hirata Y, Shimonosono T. Mixing rules of Young's modulus, thermal expansion coefficient and thermal conductivity of solid material with particulate inclusion. *J Korean Ceram Soc*. 2016;53(1):43–49. https://doi.org/10.4191/kcers.2016.53.1.43
132. Li W, Wang J, Poudel B, *et al.* Filiform metal silver nanoinclusions to enhance thermoelectric performance of p type $Ca_3Co_4O_{9+}$. *ACS Appl Mater Interfaces*. 2019;11:42131–42138. https://doi.org/10.1021/acsami.9b13607
133. Zhang H, Zheng W, Yan Q, *et al.* Electrically conductive polyethylene terephthalate / graphene nanocomposites prepared by melt compounding. *Polymer (Guildf)*. 2010;51(5):1191–1196. https://doi.org/10.1016/j.polymer.2010.01.027
134. Qi XY, Yan D, Jiang Z, *et al.* Enhanced electrical conductivity in polystyrene nanocomposites at ultra-low graphene content. *ACS Appl Mater Interfaces*. 2011;3:3130–3133. https://doi.org/dx.doi.org/10.1021/am200628c
135. Wu S, Ladani RB, Zhang J, *et al.* Aligning multilayer graphene flakes with an external electric field to improve multifunctional properties of epoxy nanocomposites. *Carbon N Y*. 2015;94:607–618. https://doi.org/10.1016/j.carbon.2015.07.026
136. Marsden AJ, Papageorgiou DG, Valles C, *et al.* Electrical percolation in graphene – polymer composites. *2D Mater*. 2018;5(032003). https://doi.org//doi.org/10.1088/2053-1583/aac055
137. Guo J, Zhao X, Beauvoir TH De, *et al.* Recent progress in applications of the cold sintering process for ceramic–polymer composites. 2018; 1801724 (2): 1–15. https://doi.org/10.1002/adfm.201801724
138. O'Dwyer JJ. Theory of dielectric breakdown in solids. *Electrochem Soc*. 1969;116(239).
139. Dissado LA, Fothergill C. Electrical degradation and breakdown in polymers. London, United Kingdom: The Institution of Engineering and Technology; 1992
140. Feilat EA, Grzybowski S, Knight P, Doriott L. Breakdown and aging behavior of composite insulation system under DC and AC high voltages. *WSEAS Trans circuits Syst*. 2016;(July

2005).

141. Chauvet C, Laurent C. Weibull statistics in short-term dielectric breakdown of thin polyethylene films. *IEEE Trans Electr Insul*. 1993;28(1):18–29.

142. Gao Y, Zhang C, Ma L, Li H, Chen S. The structural, lattice dynamic, thermodynamic, and mechanical characterization of $Na_2Mo_2O_7$ crystal by first-principles. *Phys Status Solidi*. 2022;259(2200036):1–11. https://doi.org/10.1002/pssb.202200036

143. Jovanovic DJ, Validzic IL, Mitric M, Nedeljkovic JM. Structure of disodium dimolybdate synthesized using thermo-dynamically stable molybdenum (VI) oxide clusters as precursors. *J Am Ceram Soc*. 2009;2470(25769):2467–2470. https://doi.org/10.1111/j.1551-2916.2009.03225.x

144. Spassky DA, Kozlova NS, Brik MG, *et al.* Luminescent, optical and electronic properties of $Na_2Mo_2O_7$ single crystals. *J Lumin*. 2017;192:1264–1272. https://doi.org/10.1016/j.jlumin.2017.09.006

145. Verma R, Ramanujam K, Varadaraju U V. Nanocrystalline $Na_2Mo_2O_7$: A new high performance anode material. *Electrochim Acta*. 2016;215:192–199. https://doi.org/10.1016/j.electacta.2016.08.094

146. Poda D. Scintillation in low-temperature particle detectors. *MDPI Phys*. 2021;3:473–535.

147. Tower J, Winslow L, Churilov A, *et al.* A new scintillating bolometer crystals for rare particle detection. *Nucl Inst Methods Phys Res A*. 2020;954(May 2019):162300. https://doi.org/10.1016/j.nima.2019.06.041

148. Barik SK, Chatterjee S, Choudhary RNP. Molecular and impedance spectroscopy of $Na_2Mo_2O_7$. *PRAMANA - J Phys*. 2014;83(4):571–577. https://doi.org/10.1007/s12043-014-0803-9

149. Hao S-Z, Zhou D, Pang L-X, *et al.* Ultra-low temperature co-fired ceramics with adjustable microwave dielectric properties in the Na_2O-Bi_2O_3-MoO_3 ternary system: a comprehensive study. *J Mater Chem C*. 2022;10:2008–2016. https://doi.org/10.1039/d1tc05557g

150. Zhang G, Wang H, Guo J, He L, Wei D, Yuan Q. Ultra-low sintering temperature microwave dielectric ceramics based on Na_2O-MoO_3 binary system. *J Am Ceram Soc*. 2015;533(35275):528–533. https://doi.org/10.1111/jace.13297

151. Jones HN, Trautman E, Maria J-P, Trolier-McKinstry S, Argüelles AP. Assessment of flaws in cold-sintered ZnO via acoustic wave speed and attenuation measurements. *J Am Ceram Soc*. 2023;106(October 2022):4955–4966. https://doi.org/10.1111/jace.19108

152. Wheatley CS. A feasibility study on the scalability of the cold sintering process through ultrasonic nondestructive evaluation. Master's thesis; The Pennsylvania State University; 2023.

153. Woolfrey JL, Bannister MJ. Nonisothermal techniques for studying initial-stage sintering. *J Am Ceram Soc*. 1972;55(6):390–394.

154. Cannon WR, Langdon TG. Review: creep of ceramics part 2. An examination of flow mechanisms. *J Mater Sci*. 1988;23:1–20.

155. Wilkinson DS. Creep mechanisms in multiphase ceramic materials. *J Am Ceram Soc*. 1998;81(2):275–299.

156. Guo H, Baker A, Guo J, Randall CA. Cold sintering process: A novel technique for low-temperature ceramic processing of ferroelectrics. *J Am Ceram Soc*. 2016;99(11):3489–3507. https://doi.org/10.1111/jace.14554

157. Zang M, Zheng M, Zhu M, Hou Y. Low-temperature sintering and microwave dielectric properties of $CaMoO_4$ ceramics for LTCC and ULTCC applications. *J Eur Ceram Soc*. 2024;44(1):293–301. https://doi.org/10.1016/j.jeurceramsoc.2023.09.029

158. Chi M, Liu Y, Zhou T, *et al.* Ni doping improving magnesium borate microwave dielectric ceramic for LTCC via cold sintering and post- annealing process. *J Mater Sci Mater*

Electron. 2023;34(3):1–9. https://doi.org/10.1007/s10854-022-09652-1

159. Li C, Liu Y, Chi M, *et al.* ULTCC post-annealing cold sintering densification process , microwave dielectric properties of $Zn_3B_2O_6$ ceramics. *Mater Today Commun*. 2022;33(November):104997. https://doi.org/10.1016/j.mtcomm.2022.104997
160. Madhuri R, Rajan A, Ganesanpotti S. Cold-sintered $NaCa_2Mg_2V_3O_{12}$–Li_2MoO_4 microwave dielectrics for the design and fabrication of high-bandwidth antennas. *Mater Res Bull*. 2023;158(October 2022):112069. https://doi.org/10.1016/j.materresbull.2022.112069
161. Villatte L, Rua-taborda M, Ndayishimiye A, *et al.* Mechanisms and energetics in the early stages of solvent-assisted low-temperature sintering of ZnO. *Materialia*. 2022;22(January):101418. https://doi.org/10.1016/j.mtla.2022.101418
162. Musikhin AE, Bespyatov MA, Shlegel VN, Grigorieva VD. Thermodynamic properties and phonon density of states of $Na_2Mo_2O_7$ using heat capacity measurements from 5.7 to 310K. *J Alloys Compd*. 2020;830:154592. https://doi.org/10.1016/j.jallcom.2020.154592
163. Chokshi AH, Langdon TG. Characteristics of creep deformation in ceramics. *Mater Sci Technol*. 2013;7(7):577–584. https://doi.org/10.1179/mst.1991.7.7.577
164. Hynes A, Doremus R, Hynes A, Doremus R. Theories of creep in ceramics. 2006;8436(1996). https://doi.org/10.1080/10408439608241255
165. Dean J, Bradbury A, Aldrich-Smith G, Clyne TW. A procedure for extracting primary and secondary creep parameters from nanoindentation data. *Mech Mater*. 2013;65:124–134. https://doi.org/10.1016/j.mechmat.2013.05.014
166. Davidge RW. Mechanical behaviour of ceramics. Cambridge University Press; 1979
167. Dai Z, Tyrpekl V, Boi F, Song J, Hu C, Grasso S. Cold sintering of Van der Waals layered compounds. *Open Ceram*. 2022;12(100304). https://doi.org/10.1016/j.oceram.2022.100304
168. Lotgering FK. Topotactical reactions with ferrimagnetic oxides having hexagonal crystal structures-I. *J Inorg Nucl Chem*. 1959;9:113–123. https://doi.org/10.1016/0022-1902(59)80070-1
169. Fox AJ, Drawl B, Fox GR, Gibbons BJ, Trolier-McKinstry S. Control of crystallographic texture and surface morphology of Pt/TiO_2 templates for enhanced PZT thin film texture. *IEEE Trans Ultrason Ferroelectr Freq Control*. 2015;62(1):56–61. https://doi.org/10.1109/TUFFC.2014.006671

VITA

Javier Mena Garcia

Javier Mena Garcia was born in Ciudad Juarez, Mexico. He attended Tecnologico de Monterrey, Mexico and received a B. Sc. degree in Mechatronics Engineering. He continued his studies at the Universidad Autonoma de Ciudad Juarez, where he earned a M. Sc. in Materials Science and Engineering. He dedicated 13 years of his professional career in the automotive industry, being responsible for engineering activities related to failure analysis, manufacturing processing, quality assurance and problem solving. In 2019 he became the recipient of a Fulbright scholarship, which allowed him to join Professor Clive Randall's group and begin his doctoral studies in cold sintering of ceramic matrix composites, at The Pennsylvania State University. His research interests include the processing-structure-property relationships for the next generation of electronic packaging materials. Listed below are his publications during his doctoral studies:

Mena-Garcia, J.; Mervosh, M.W.; Yousefian, P.; Ndayishimiye, A.; Perini, S.E.; Li, W.; et al. Dielectric, electrical and thermal properties of Sodium Molybdate-hexagonal Boron Nitride composites enabled by cold sintering, *Ceram Intern*. **2024**; https://doi.org/10.1016/j.ceramint.2024.05.155. (*invited*)

Mena-Garcia, J.; Ndayishimiye, A.; Fan, Z.; Perini, S.E.; Li, W.; Poudel, B.; et al. Sodium molybdate-hexagonal boron nitride composites enabled by cold sintering for microwave dielectric substrates. *J Am Ceram Soc*. **2023**; 106: 5975–5985. https://doi.org/10.1111/jace.19254

Mena-Garcia, J.; Dursun, S.; Tsuji, K.; Bang, S. H.; Fan, Z.; Ndayishimiye, A.; Randall, C. Integration and characterization of a ferroelectric polymer PVDF-TrFE into the grain boundary structure of ZnO via cold sintering. *J Europ Ceram Soc.* **2022**; 42 (6): 2789-2797. https://doi.org/10.1016/j.jeurceramsoc.2022.01.064.

Ndayishimiye, A.; Fan, Z.; **Mena-Garcia, J.**; Anderson, J.M.; Randall, C.A. Coalescence in cold sintering: A study on sodium molybdate. *Op Ceram*. **2022**; 11: 100293. https://doi.org/10.1016/j.oceram.2022.100293.